Band gap mapping of alloyed ZnO using probe-corrected and monochromated STEM-EELS

Wei Zhan

Thesis submitted in partial fulfilment of the requirements for the degree of Philosophiae Doctor

Department of Physics

Faculty of Mathematics and Natural Science

University of Oslo

March 2018

Series of dissertations submitted to the
Faculty of Mathematics and Natural Sciences, University of Oslo
No. 1988

ISSN 1501-7710

Cover: Hanne Baadsgaard Utigard.
Print production: Reprosentralen, University of Oslo.

Dedicated to my grandfather and grandmother

Abstract

The band gap of semiconducting ZnO can be readily tuned through alloying it with other relevant oxides, such as CdO, consequently extending the performance of the corresponding materials and devices. In this context, one of the challenges is to establish the methodology for two-dimensional band gap measurements on the nanometer scale. Here, monochromated electron energy loss spectroscopy (EELS) in combination with probe-corrected scanning transmission electron microscopy (STEM) can be applied, potentially with much greater success compared to traditional techniques with low spatial resolution. However, up to now, the EELS based band gap mapping technique has not seen widespread use, primarily due to its experimental and data processing complexities.

In this work, utilizing state-of-the-art probe-corrected and monochromated STEM-EELS platform without particular instrumental design, we developed and applied methods for acquiring large band gap maps with high spatial resolution. A newly-developed efficient computing method was employed to extract band gap maps from the EELS data after proper background subtraction. All these advances are highlighted by the band gap mapping of $Zn_{1-x}Cd_xO$/ZnO hetero structure with a spatial resolution well below 10 nm and a high spectral precision.

Nevertheless, band gap measurement by EELS are also restricted in spatial resolution, which is fundamentally determined by the delocalization length (L_{50}) of the inelastic scattering process. The origin of this delocalization is the long range electrostatic interactions between the atomic electrons of the sample and the incident high-energy electrons. The EELS plasmon energy map has obviously higher spatial resolution than the band gap map, and its experiment as well as data extraction is also much easier to perform. In order to push the spatial resolving power in EELS band gap analysis further, the relationship between the band gaps and plasmon energies in $Zn_{1-x}Cd_xO$ was investigated based on the fact that both depend strongly on the unit cell parameter. A robust quantitative correlation was established, providing a simple and straightforward way to calculate the band gap variations just from the easily measured plasmon energy, with improved spatial resolving ability as compared with the conventional EELS approach.

In order to further verify the success of the probe-corrected and monochromated STEM-EELS technique, it was put into application to a new system, namely separate $ZnCr_2O_4$ nano-

inclusions embedded in ZnO matrix. Band gap mapping of $ZnCr_2O_4$ nanoparticles in ZnO matrix and their interface was successfully achieved, confirming the validity of this STEM-EELS approach. In addition, probe-corrected STEM enables sub-ångström imaging, from which the realistic structure can be revealed. We employed atomic-resolution images together with geometric phase analysis (GPA) to analyze the structure and strain at $ZnCr_2O_4$/ZnO interfaces, which is of critical importance for thin film growth and may affect band gap.

Acknowledgements

First I would like to deeply thank my supervisors, Øystein Prytz, Andrej Kuznetsov and Espen Flage-Larsen for their scientific guidance and invaluable support. Their efforts made this project possible. In particular, I am grateful to my main supervisor, Øystein Prytz, who contributed expert ideas and inputs to this project, from which I have learned a lot.

Moreover, I appreciate the generous help received from Cecilie Granerød, Vishnukanthan Venkatachalapathy, Andrey Yurievich Kosinskiy, Ingvild Julie Thue Jensen, Klaus Magnus Håland Johansen, Thomas Aarholt, Lasse Vines, and Patricia Almeida Carvalho. Their collaboration promotes the progress of this project. I would also like to express my acknowledgment to Phuong Dan Nguyen and Ole Bjørn Karlsen for the precious assistance. Besides, thanks all the friends in Structure Physics group for their hospitality.

In addition, my gratitude goes to my parents and family. Only working harder is to repay them better. Especially, I would like to thank my grandfather and grandmother, although heaven is perhaps far away. Time is so cruel that I could not see you two for the last time, which is the greatest regret in my life. For more than two decades, there are you and your love accompanying and encouraging me all long, which, I believe, will last forever……Then, in this world, is there anything else that deserves my pursuing?

The Research Council of Norway is acknowledged for the financial support to the Norwegian Center for Transmission Electron Microscopy, NORTEM (197405/F50), the Norwegian Micro- and Nano-Fabrication Facility, NorFab (197411/V30), the FriPRO Toppforsk project FUNDAMeNT (no. 251131), and the DYNAZOx project (no. 221992).

Preface

This project with the title "Band gap mapping of alloyed ZnO using probe-corrected and monochromated STEM-EELS" started in September, 2013, and received financial support from the University of Oslo. My principal supervisor is Associate Professor Øystein Prytz from Structure Physics group. My co-supervisors are Professor Andrej Kuznetsov from Semiconductor Physics group, University of Oslo, and Dr. Espen Flage-Larsen from SINTEF Materials and Chemistry. The main work of the project, including TEM/probe-corrected STEM/(monochromated) EELS/EDX, was carried out in Structure Physics group, University of Oslo. Part of the work, such as $Zn_{1-x}Cd_xO$/ZnO thin film synthesis, was performed at Semiconductor Physics group, University of Oslo. I also cooperated with Klaus Magnus Håland Johansen and Associate Professor Lasse Vines from Semiconductor Physics group, as well as Ingvild Julie Thue Jensen and Patricia Almeida Carvalho from SINTEF Materials and Chemistry.

The main objective of this PhD project was to investigate the band structure of alloyed ZnO in two dimensions by means of the high spatial and spectral resolution of monochromatic EELS in combination with probe-corrected STEM. This thesis takes the form of five chapters. In Chapter 1, the properties of ZnO and related materials are presented, and the importance of band gap engineering in semiconductor is emphasized. Thereafter we introduce the background of band gap measurement of $Zn_{1-x}Cd_xO$/ZnO up to now, and concentrate on the benefit in EELS band structure analysis. The hypothesis of a novel approach for extracting band gap on the basis of the correlation between band gap and plasmon energy is brought forward. ZnO matrix with nano $ZnCr_2O_4$ inclusion is adopted for structure and strain investigation taking use of high-resolution STEM, GPA, energy-loss near-edge structure (ELNES), and monochromatic low-loss EELS. In Chapter 2, the methodology utilized in this work is described in detail, such as EDX, CL and XPS. These techniques and their results constitute the main part of this thesis. A lot of attention is focused on STEM and EELS, which are employed for structure determination and band gap mapping. Additionally, sample fabrication, TEM sample preparation and experimental setup are briefly described. Chapter 3 provides an overview of all the papers. Chapter 4 gives a brief summary of this thesis and some suggestions for future work.

List of abbreviations

ABF	Annular Bright-field
ADF	Annular Dark-field
CBM	Conduction Band Minimum
CL	Cathodoluminescence
DOS	Density of States
EDX	Energy-dispersive X-ray Spectroscopy
EELS	Electron Energy-Loss Spectroscopy
ELNES	Energy-Loss Near-Edge Structure
EXELFS	Extended Energy-Loss Fine Structure
FFT	Fast Fourier Transforms
FWHM	Full Width at Half Maximum
GPA	Geometric Phase Analysis
HAADF	High-angle Annular Dark-field
HRTEM	High-resolution Transmission Electron Microscopy
MOVPE	Metal Organic Vapour Phase Epitaxy
PL	Photoluminescence
SDD	Silicon Drift Detector
STEM	Scanning Transmission Electron Microscopy
TEM	Transmission Electron Microscopy
VBM	Valence Band Maximum
XPS	X-ray Photoelectron Spectroscopy
XRD	X-ray Diffraction
ZLP	Zero-loss Peak

Contents

Chapter 1

Introduction

Engineering the band gap of ZnO-related semiconductors is capable of bringing about a wealth of novel nanostructures with interesting properties. This has resulted in a multitude of applications. Therefore measurements of band gap with high spatial and spectral resolution at relevant length scales are in high demand. This information is not readily available from traditional methods, which are very limited in their spatial resolution. In Chapter 1.1, a few outstanding properties as well as practical usages of ZnO-related materials are briefly introduced. Chapter 1.2 introduces three kinds of band gap engineering methods, including alloying, heterojunction and quantum well. Then the current situation of band gap measurement is presented in Chapter 1.3, and the critical importance of the probe-corrected scanning transmission electron microscopy (STEM) and monochromated electron energy loss spectroscopy (EELS) technique, which can be used for two-dimensional band gap mapping with nanoscale resolving power, is emphasized. However, such studies are very rare because of experimental and data processing complexity in EELS band gap analysis. Therefore, a new approach based on the correlation between band gap and plasmon energy is put forward to reconstruct band gap mapping with improved spatial resolution, as described in Chapter 1.4. Last but not the least, the STEM-EELS technique was applied in $ZnCr_2O_4$ nanoparticles grown in ZnO matrix, and two-dimensional band gap mapping was achieved. We also performed structure and strain study by means of the combination of probe-corrected atom-resolved STEM image and geometric phase analysis (GPA).

1.1 Properties of ZnO-related materials

ZnO is a semiconductor that crystallizes in the wurtzite structure. It exhibits a wide and direct band gap (E_g) of ~3.3 eV at room temperature, which enables optical and electronic applications in the blue/ultraviolet range, including light-emitting diodes (LEDs), lasers and photodetectors [1, 2]. The large free-exciton binding energy (60 meV) of ZnO guarantees that efficient excitonic emission processes can persist at or above room temperature [3, 4]. Furthermore, the large piezoelectric constants pave the way for the usage of ZnO in energy generators and converters [5, 6]. In addition, the conductivity of ZnO exhibits strong sensitivity to the presence of adsorbed species, which makes it suitable for sensor application

[7, 8]. Last but not the least, because of the large non-linear optical coefficients, ZnO is seen as a promising material used in non-linear optical devices, and the high thermal conductivity causes ZnO to be suitable as an additive. Other advantages existing in ZnO consist of availability of large single crystals, amenability to wet chemical etching, radiation hardness, high stability at room temperature, which greatly benefits semiconductor device fabrication and applications [2].

In addition, many novel properties, such as piezo-electricity and ferromagnetism, exist in trivalent metal oxide alloyed ZnO compounds, where the modifications to ZnO's semiconducting behavior are found [2]. Spinel oxides, which can be formed in these alloyed compounds, have motivated intensive interest due to their wide range of applications in luminescence [9], catalysis [10, 11], sensors [12, 13], magnetism [14], and lithium batteries [15]. As an example, $ZnCr_2O_4$ spinels have commonly acted as efficient catalysts, humidity sensors and magnetic materials [16-18].

1.2 Band gap engineering

Many properties of the semiconductor depend on the band gap, which is the energy separation between the lowest conduction band and the highest valence band. Band gap engineering, such as alloying, heterojunction and quantum well, can develop new semiconductor materials or structures with useful physical properties, and has attracted a great deal of interest.

Alloying is of critical importance for the realization of a specific opto-electrical behavior in semiconductor, and hence greatly benefits device technology. In the case of ZnO, conductivity, transparency, piezoelectricity, room-temperature ferromagnetism, magneto-optic and chemical-sensing effects are all strongly influenced by intentionally alloyed elements. These usually cause the band gap value to change somewhat [19]. In analogy to GaN-based alloys ($Ga_{1-y}In_yN$ and $Ga_{1-y}Al_yN$), the band gap of wurtzite ZnO can be engineered via metal substitution for the cation site, enabling the tunability of optical emission, which is highly beneficial for optoelectronic device applications [20-24]. Especially, fabricating and characterizing of ZnO-based alloys, such as $Zn_{1-y}Mg_yO$ and $Zn_{1-x}Cd_xO$, are critically important from the viewpoint of their practical usages in *p–n* junctions [22]. After alloyed with MgO (E_g~7.7 eV), $Zn_{1-y}Mg_yO$ films display great promise to act as barrier layers owing to its wider band gap, which can be tuned from 3.3 eV to 4.0 eV depending on Mg concentration. Similarly, to narrow the band gap, ZnO can be alloyed with

CdO (E_g~2.3 eV), allowing modulation of the band gap of $Zn_{1-x}Cd_xO$, while maintaining its direct band gap, high mobility and drift velocity, radiation hardness, and optical absorption [20-26]. Device performance can thus be optimized in a flexible manner [27]. Zn and Cd are in the same subgroup of the periodic table, and we consider them to be iso-electronic in the $Zn_{1-x}Cd_xO$ alloy. The Cd^{2+} ion has significantly larger ionic radius than Zn^{2+}. After introducing Cd^{2+} into the wurtzite ZnO matrix, the replacements of Zn_x by Cd_x would lead to the increase of the lattice constants and hence the unit cell volume [27, 28], as illustrated in Figure 1.1. This is the main mechanism giving rise to the reduction of band gap [26, 28-31]. Existing publication reported that Cd concentrations as high as x = 0.67 can be achieved while maintaining the wurtzite structure, resulting in a drop in band gap from 3.3 eV to 1.7 eV [25].

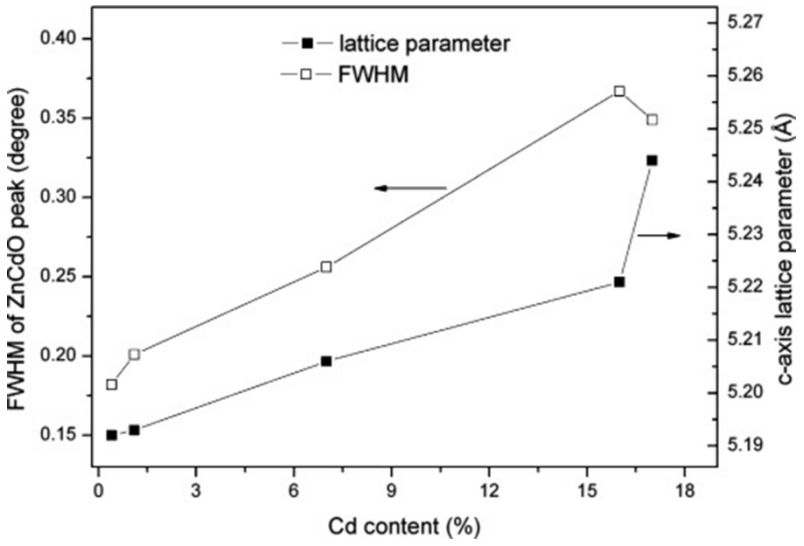

Figure 1.1 *c-axis and FWHM of $Zn_{1-x}Cd_xO$ as a function of Cd content x.* [27]

Basically, the band gap of $Zn_{1-x}Cd_xO$ reduces as Cd content x raises, as described in Figure 1.2. A quantitative equation that relates band gap and Cd content x is given by the solid line.

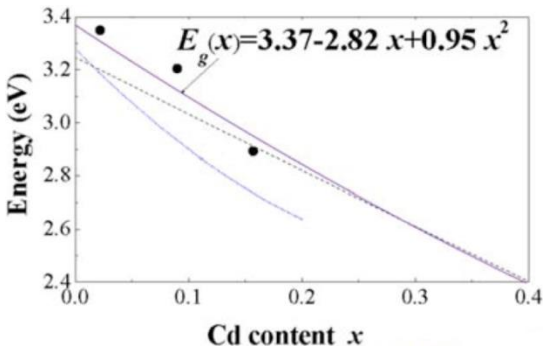

Figure 1.2 *Band gap of $Zn_{1-x}Cd_xO$ as a function of Cd content x.* [26]

Most nanostructure-based semiconductor devices, such as heterostructures (e.g. *p–n* junction) and quantum wells, take advantage of the excellent properties that can be achieved through band gap engineering. Through the choice of different semiconducting materials and alloying levels, the energy position of band gap can be tailored, leading to redistributed charge carriers and enhanced optical and electrical properties.

A heterojunction is formed when bringing two different semiconductors in contact with each other. In the *z*-direction, there is confinement of electron transport, while electron can move freely along the *xy*-direction, as illustrated in Figure 1.3. In such structure, a two-dimensional electron system may exists, and quantum confinement effects have been observed in polar ZnO/$Zn_{1-y}Mg_yO$ heterostructures [32, 33]. Various functional properties of semiconductor electronics are attributable to the *p–n* junction, a type of heterostructures that result from joining *p*-type and *n*-type semiconductors together, see Figure 1.3. There is an asymmetry of the density of electrons and holes at both sides of the junction, and light can be emitted from this structure through recombination of the electron and hole. There is a lack of reliable and reproducible *p*-type ZnO-based alloys as a result of the internal defects and its high electron affinity level [1, 2]. However, ZnO-based *p–n* junctions can be achieved via depositing the easily available *n*-type ZnO (the active layer) on other *p*-type semiconductors, such as *n*-ZnO/*p*-AlGaN, which enabled high-intensity UV emission [2, 34]. Additionally, the polarization-induced doping technique utilized in graded $Ga_{1-z}Al_zN$ *p–n* junction results in highly improved electrical conductivity and emission efficiency in optoelectronic devices, and could be applied in the ZnO family [35].

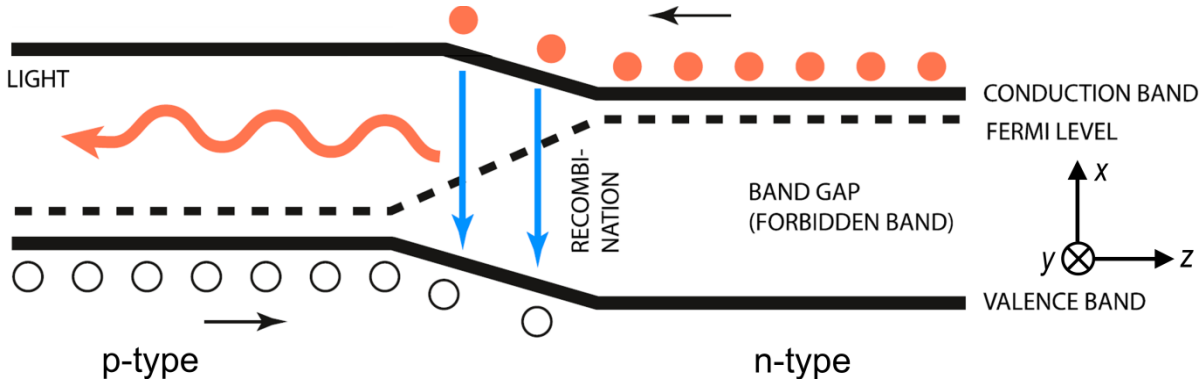

Figure 1.3 *Light emission from a p–n junction under a forward voltage.* [36]

Through sandwiching a thin layer (~2–100 nm) of a low band gap material between two thick layers (several hundred nm) of wider band gap material, a single quantum well is fabricated. The thick and thin layers serve as the barrier and well, respectively. Similar to heterostructure,

the motion of electrons in the *z* (growth) direction is restricted, while electrons are free to move in the *xy* plane, thus forming a two-dimensional carrier system in the well, as can be seen from a quantum well structure of $Ga_{1-z}Al_zAs/GaAs$ in Figure 1.4 [37]. It is well known that GaAs has a direct band gap 1.4 eV corresponding to light in the infrared spectral region. Electrons and holes are held in close proximity by a well layer of GaAs between two $Ga_{1-z}Al_zAs$ barriers, promoting efficient recombination in devices of lasers and LEDs. The well width and the barrier composition can be adjusted to modulate special properties, such as band gap. Utilizing such quantum well structures, $ZnO/Zn_{1-y}Mg_yO$ superlattices (multiple quantum wells with narrow barrier thickness), where $Zn_{1-y}Mg_yO$ serve as barrier layers, have been shown to produce stimulated emission up to 373 K [21].

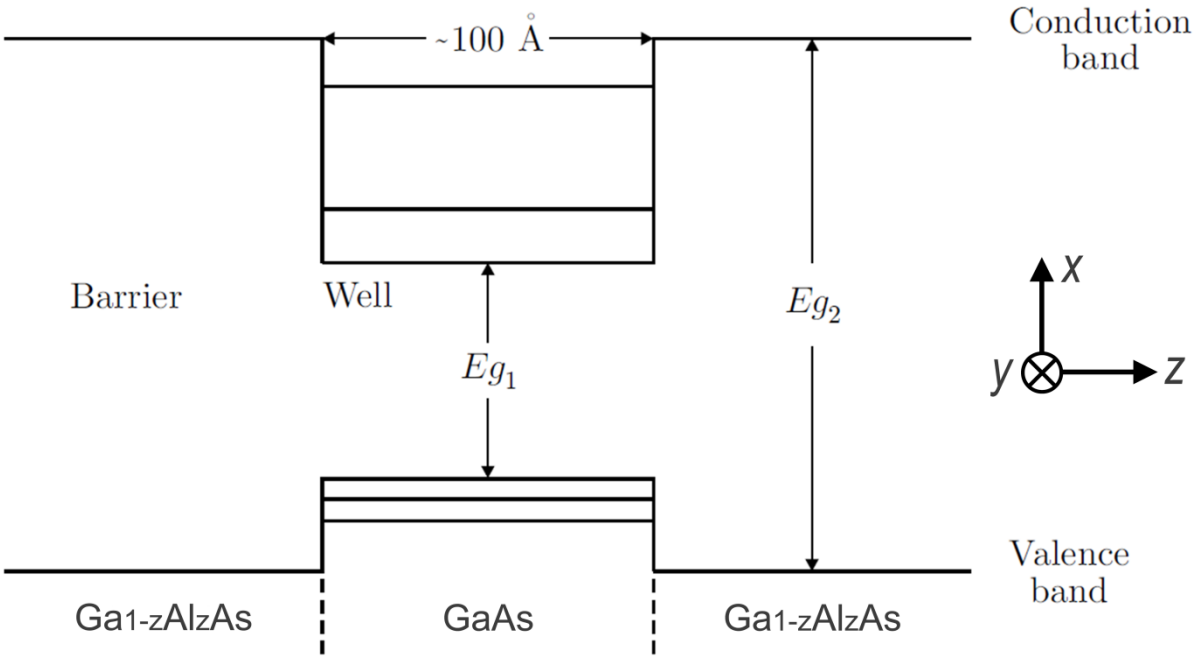

Figure 1.4 *Band edges of a $Ga_{1-z}Al_zAs/GaAs$ quantum well. The energies of the subbands are displayed schematically. z indicates the growth direction.* [37]

Designs of a broad range of semiconductor devices rely on quantum wells which can provide carrier and optical confinement. Examples include blue light-emitting diodes (LEDs) on the basis of wurtzite GaN with a direct band gap of 3.4 eV and exciton binding energy of ~25 meV at 300 K. GaN is widely applied in green, blue-ultraviolet, and white light-emitting devices. Efficient blue LEDs can be produced through the growth of quantum well structures of GaN-based alloys (AlGaN, InGaN) with different concentrations. Figure 1.5 displays such a quantum well based on GaN [38]. This great invention enables bright and energy-saving white light sources, and was awarded the Nobel Prize in Physics in 2014 [36]. In brief,

currently there is a rapid conversion from illumination based on incandescence to devices using blue LEDs (in combination with other colors) to produce white light. The LEDs have a very long lifetime, and use approximately ten times less energy than incandescence-based lighting. The overall cost of LEDs lighting is therefore much lower than traditional light sources. Since 20–30% of the global electrical energy is used for illumination, the replacement of light bulbs by LEDs will dramatically reduce electricity requirements, bringing about significant energy savings, which is of great benefit to mankind.

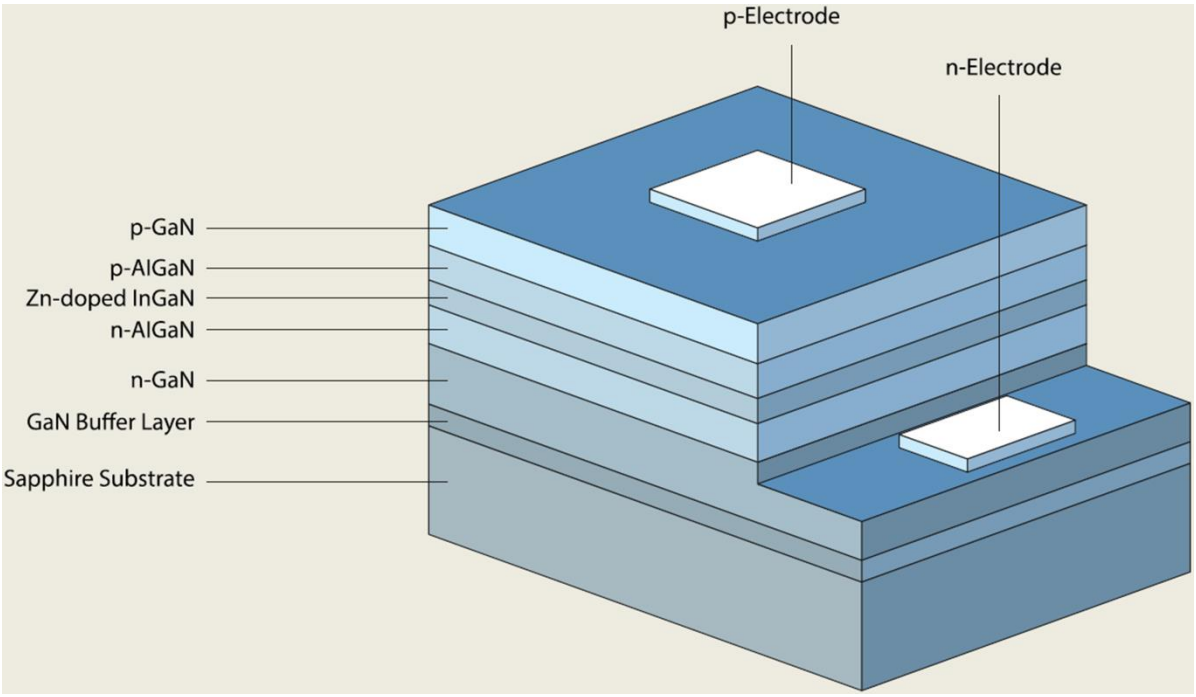

Figure 1.5 *A blue LED structure.* [38]

ZnO has several advantages over GaN, among which are a larger exciton binding energy and the availability of large bulk single crystals. ZnO, as an alternative to GaN, holds promises as a good candidate for fabrication of UV/blue LEDs. As is known, high quality *n*-type ZnO-based alloys can be obtained easily and thus used widely as transparent contacts and high electron mobility transistors [39]. While *p*-type ZnO showed promising applications in UV light emitters and transparent high-power electronics [40, 41], and would greatly promote LEDs. Therefore many researchers have been driven to realize robust and stable *p*-type ZnO-based alloys despite of the difficulty [39]. In addition, to form LEDs based on ZnO *p*–*n* junctions, *n*-type ZnO can be fabricated on other available *p*-type semiconductors, including GaN and AlGaN [42-44].

Apart from the nanostructures described above, alloyed semiconductor nanocrystals with adjusted constituent stoichiometries also exhibit outstanding optical and electronic properties [45, 46]. Owing to quantum confinement effects, reducing the size of a semiconductor particle to nanoscale effectively widens its band gap. In particular, the band gap of alloyed nanocrystals can be tailored through size effects as well as composition control [47]. Thus, instead of measuring the average band gap of many particles with different sizes, it is necessary to determine the band gap of a seperate particle (e.g. nano $ZnCr_2O_4$ inclusion embedded in ZnO matrix, see Figure 2.17).

1.3 The situation of band gap measurement

Conventional techniques, such as photoluminescence (PL) [27], cathodoluminescence (CL) [48], optical absorption [22] and X-ray photoelectron spectroscopy (XPS) [49] have been applied in measuring band gap structure of alloyed ZnO with high spectral resolution. However, their poor spatial resolutions (several microns) have existed as a major drawback for many years. In addition, they can only reveal band gap one-dimensionally. The need of high spatial resolution techniques and cross-methodological interpretations is thus evident.

In a modern probe-corrected STEM instrument, a sub-ångström electron beam with greatly improved signal strength is formed, and can be used to simultaneously perform high resolution imaging and spectroscopic studies [50, 51]. This technique becomes particularly powerful when the electron beam is monochromated, thereby allowing EELS investigations with both high spatial and spectral resolution. Probe forming correctors mounted in STEM greatly increase the number of electrons that enter the EELS spectrometer and thus the signal-to-noise ratio [52-54]. Encouragingly, these advancements have recently allowed semiconductor band gaps to be analyzed in detail [55-59].

Although probe-corrected STEM has realized atomic resolution imaging, EELS spatial resolving ability varies from case to case. Existing publications report that the spatial resolution for EELS analysis is expressed as the inelastic delocalization length [60-62].

$$L_{50} = \frac{0.44hc_0[eU(eU + 2m_0{c_0}^2)]^{\frac{1}{4}}}{[E(eU + m_0{c_0}^2)]^{\frac{3}{4}}} \tag{1.1}$$

Where L_{50} is the diameter which contains 50% of the inelastic interactions, h is the planck constant, c_0 is light speed, e is elementary charge, U is accelerating voltage, m_0 is electron mass, E is energy loss.

As can be seen from the above-mentioned formula, the spatial resolving ability of EELS analysis is mainly dictated by energy loss and microscope high tension. EELS spatial resolution (L_{50}) for band gap measurements is material dependent and would vary depending on the local dielectric function, e.g., the effective screening of the field imposed by the electron beam. Considering excitations across the band gap (3.7–2.3 eV) of common semiconductors, this inelastic delocalization provides a theoretical spatial resolution between 5–7 nm, which is much better than conventional tools.

Existing work reported that monochromated EELS was employed to probe the electron transitions within the visible and near-UV spectral range [30, 57]. Considerable amount of past efforts have been spent on one-dimensional study of band gap, such as point, line scan (see Figure 1.6).

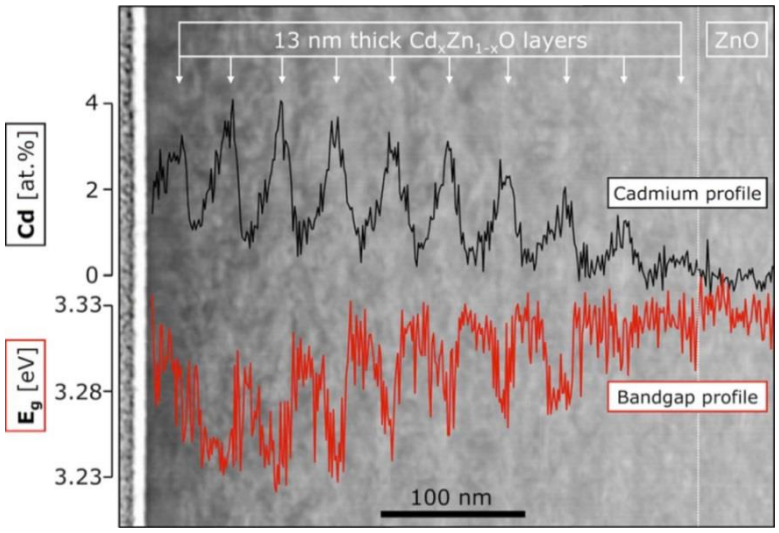

Figure 1.6 *Annular dark-filed (ADF)-STEM image of $Zn_{1-x}Cd_xO/ZnO$ multilayer. The black and red lines show Cd content and band gap profiles, respectively.* [30]

Two-dimensional observation of optical band gaps, which is of great importance, can be realized through the STEM-EELS approach. However, experimental and data analytical complexities hinder investigators to carry out this kind of research. As shown in Figure 1.7, Lin Gu and co-authors [57] proposed energy-filtered STEM to increase the collection efficiency and hence achieve band gap mapping. This special setup is not feasible in most microscopes. Besides, EELS spatial resolution is also tested here as well as in the above

publication, and a value of approximately 10–12 nm is found [30, 57]. This is larger than the theoretical prediction of L_{50} (5–7 nm) for common semiconductors.

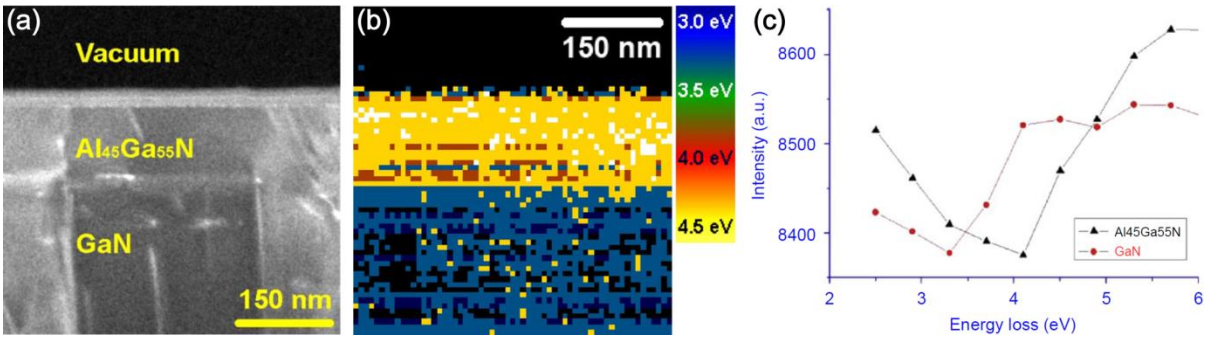

Figure 1.7 *(a) EF-STEM image of $Al_{45}Ga_{55}N$/GaN. (b) Band gap map. (c) EELS spectra.* [57]

In the current thesis, the band structures of $Zn_{1-x}Cd_xO$ were analyzed to enhance our understanding of its properties in bulk and close to the interfaces. Compared with optical spectroscopy, the advantage of spatially resolved band gap profiling is that structural imaging, Cd content x and band gap (even plasmon energy, see Chapter 1.4) can be obtained in the same area with significantly better spatial resolution. Unlike the research performed by Lin Gu et al [57], no particular instrumental design exists in our study. To handle the problem associated with shortage of collected EELS signals, the exposure time of each single spectrum was set up just below the limiting exposure of CCD. This also avoids saturation of the diodes. Besides, the thin specimen, long acquisition time and good environment ensured the feasibility of the spectrum mapping experiments. CL experiments were performed for additional confirmation of the observed absolute values of the band gap in the ZnO layer. The actual content of Cd in $Zn_{1-x}Cd_xO$ was studied by energy-dispersive X-ray spectroscopy (EDX). There are four FEI super-X EDX detectors in the microscope, which greatly improves the counts of EDX signals. Thus the acquisition of STEM imaging, chemical element and band gap from the same position provides a powerful tool to determine the relationship between the band gap and chemical composition of the compound.

In a word, as the technology of nanoscale semiconductor advances, two-dimensional imaging of band gap on the nanometer scale is drawing more and more attention. Using the nanoscale resolving power of monochromated EELS coupled with probe-corrected STEM, it not only provides a useful measurement of the band gap energy, but also is able to map how the band gap energies are distributed in space. This may significantly benefit the field of band gap engineering in semiconductors, for instance, accurate control of band structure and composition on the nanometer scale.

1.4 Band gap mapping using the E_p–to–E_g reconstruction method

As mentioned previously, two-dimensional imaging of band gaps at the nanometer scale can be achieved through the combination of probe-corrected STEM plus monochromated EELS, but are very rare due to the experimental and data analytical complexities in EELS band gap mapping. The difficulty of performing experiments exists in the setup of the hardware required, such as monochromator and probe Cs corrector. For instance, monochromtors can improve the energy resolution of EELS spectrum. However, it also significantly decreases the EELS signal, because the already narrow energy spread of a focused beam is further refined by the selecting slit. Besides, the beam that passes through the selecting slit and the film into GIF spectrometer is sensitive to environmental disturbance and would shift after a period of time, leading its intensity to decrease gradually, in particular for specimen with beam charging effects. Moreover, as recently shown, residual retardation losses, surface plasmons and excitations of guided-light modes can be possible obstacles for the measurement of band gap. In addition, unfortunately, even EELS has some limitation in spatial resolving ability for band gap analysis, with theoretical prediction of 5−7 nm for common semiconductors.

For the above-mentioned reason, this exploratory study was conducted to develop a novel and straightforward approach to acquire band gap map according to plasmon energy (namely the E_p–to–E_g reconstruction method), and improve the spatial resolution further. This solution is realized on the basis of the following potential relevance as well as spatial resolving ability discrepancy between band gap and plasmon energy in $Zn_{1-x}Cd_xO$/ZnO.

As described in the preceding publications, when Cd content *x* increases, the band gap of $Zn_{1-x}Cd_xO$ reduces [26, 29-31]. Meanwhile, the unit cell volume raises [27, 28], causing the valence electron density to decrease. This may have a direct impact on the plasmons in the system. As can be seen from Equations (2.8) and (2.9), higher Cd contents are associated with lower plasmon energies. This is also verified by the plasmon mapping of the $Zn_{1-x}Cd_xO$ layer with Cd compositional variations [63]. Therefore, band gap and plasmon energy in $Zn_{1-x}Cd_xO$/ZnO are both in connection with Cd content *x* and unit cell parameter, implying the probable existence of a quantitative connection. Although this relationship could be of great help for conveniently determining band gap via plasmon energy, to the best of our knowledge, to date there is no research available in the previous literature about such relevance.

A good quality plasmon energy map is much easier to acquire than a band gap map if conducting these two experiments separately, because a monochromator is not a must, and extracting the plasmon energy afterwards is much simpler. Furthermore, the plasmon energy map has a merit over the band gap map in significantly higher spatial resolving ability. As an example, at a high tension of 60 kV used for EELS band gap experiment in this thesis, the theoretically expected spatial resolutions (L_{50}) are approximately 5.41 nm and 1.46 nm for energy loss processes 3 eV and 19 eV, which are close to ZnO band gap and plasmon energy, respectively. According to Equation (1.1), to improve EELS spatial resolution, we could either reduce high tension (U) or increase energy loss (E). For ZnO band gap measurement, to reach the same spatial resolution as ZnO plasmon energy, the high tension needs to be reduced from 60 kV to 0.18 kV. This would cause the beam intensity to be highly weak, thus making two-dimensional nanoscale observation of band gap more challenging, and the broadening of beam size would outweigh the improvement of inelastic delocalization (L_{50}).

Combing monochromatic electrons with probe-corrected STEM, the signals of band gap and plasmon energy can be simultaneously collected pixel by pixel, forming two-dimensional mapping with a large number of data points, which is advantageous for analyzing their relationship. Consequently, a quantitative correlation between band gap and plasmon energy in $Zn_{1-x}Cd_xO$/ZnO can be established on the basis of their intrinsic relevance with the common determining factor of unit cell parameter.

In conclusion, the combination of monochromated EELS plus probe-corrected STEM enabled us to observe band gap and plasmon energy simultaneously on the nanometer scale. An equation between band gap and plasmon energy was built to quantitatively correlate the two in an example system of $Zn_{1-x}Cd_xO$/ZnO, giving a new and convenient approach for band gap mapping with improved spatial resolution.

1.5 Structure and strain of nano $ZnCr_2O_4$ inclusions in ZnO matrix

The STEM-EELS method we developed is a powerful tool for band gap mapping of the $Zn_{1-x}Cd_xO$/ZnO heterostructure with high spatial and spectral resolution, see Chapter 1.3. Further research by means of this approach is needed in order to make it more convincing. Therefore, the STEM-EELS technique was applied in band gap mapping of a new system, namely separate $ZnCr_2O_4$ nanoparticles embedded in ZnO matrix, as described below. Moreover, strain is found to influence band gap [64]. Thus the structure and strain at ZnO/$ZnCr_2O_4$ interfaces were investigated through high-resolution STEM imaging together with GPA

analysis. We attempted to see how band gap is affected by strain at the interface region. Note that this is just an initial try and a detailed study in the future is required.

Atomic sites and electronic structure of defects as well as defect-induced strains, especially at hetero-interfaces, have a strong impact on the properties of materials and hence the performance of device, and are required to be resolved experimentally. Therefore, the structure and strain field of lattice defects have received a great deal of attention. STEM can observe crystal structure with easier interpretation than TEM. Furthermore, STEM enables the simultaneous acquisition of high-angle annular dark-field (HAADF) and annular bright-field (ABF) information. HAADF collects the signals of elastically scattered electrons to form images showing strong atomic-number (Z) contrast. ABF, which displays phase contrast, can image both heavy and light elements [65]. For probe-corrected STEM, spherical aberration correctors [50] offer sub-ångström size beam [51] with enhanced intensity, making atom-resolved imaging and fast element mapping by either EELS or EDX possible, which can reveal quantitative information of defect structure. Especially, previous investigations have consistently applied GPA in measuring lattice strains of high-resolution HAADF images [66, 67].

EELS, which utilizes element dependent inelastic scattering, provides both compositional and electronic information at high spatial resolution [61]. For target atoms in the sample, the core-level excitations by incident-beam electrons give unique EELS spectroscopic information about the excited atom as well as its bonding states [68]. Furthermore, monochromatic EELS in conjunction with probe-corrected STEM can be employed to map band gap of nanoparticles with high spatial and spectral resolution.

In this work, we employed nano $ZnCr_2O_4$ inclusions in ZnO matrix to analyze the structure and strain. XRD measurements [Paper III] confirmed the co-existence of two pure phases in the sample, ZnO and $ZnCr_2O_4$. Figure 1.8 illustrates their schematic unit cells. ZnO crystallizes in the non-centrosymmetric wurtzite structure with polarity along the c axis, and the lattice constants are $a = b = 3.25024$ Å, $c = 5.20703$ Å, $\alpha = \beta = 90^\circ$, $\gamma = 120^\circ$, in accordance with preceding report [69]. While $ZnCr_2O_4$, with the spinel structure, has antiferromagnetism, and the unit cell dimensions are as follows, $a = b = c = 8.32904$ Å, $\alpha = \beta = \gamma = 90^\circ$, agreeing well with earlier investigation [70].

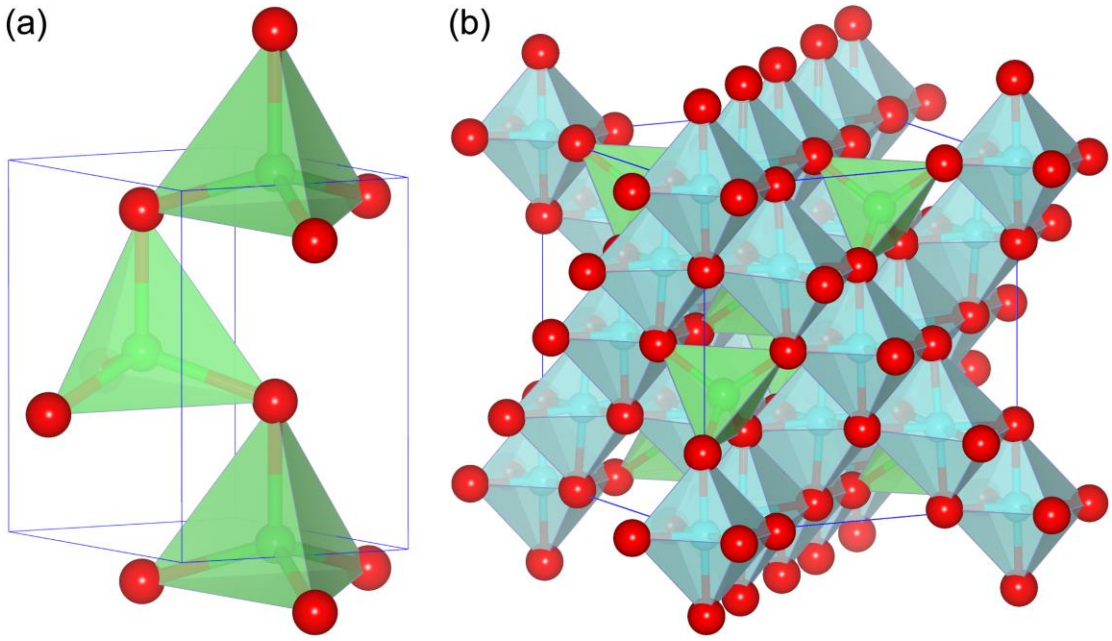

Figure 1.8 *Schematic unit cells of (a) wurtzite ZnO and (b) spinel $ZnCr_2O_4$. The green, cyan and red balls represent Zn, Cr and O, respectively.*

In summary, probe-corrected STEM, GPA analysis and (monochromated) EELS was utilized to investigate the structure and strain at $ZnO/ZnCr_2O_4$ interfaces. ELNES was employed to analyze Cr valence across $ZnO/ZnCr_2O_4$ interface, and band gaps of $ZnCr_2O_4$ nanoparticles were mapped two-dimensionally utilizing the STEM-EELS approach. Thin film growth will benefit from this study.

Chapter 2

Methodology

In this work, probe-corrected STEM, (monochromated) EELS, EDX, CL, XPS and GPA were employed to carry out band gap mapping, structure characterization and strain analysis. The purpose of this chapter is to give a detailed description of these different methodologies. In particular, this chapter focuses on EELS band gap measurements, whose accuracy depends on multiple aspects of the experiments and data analyses. This chapter ends by introducing sample fabrication, TEM sample preparation and experimental setup in detail, which are fundamentally important for the achieved outcome of this thesis.

2.1 Scanning transmission electron microscopy

When a focused beam is scanning on the specimen, the incident electrons interact with the Coulomb potential of the atoms. The scattered electrons are detected by STEM detectors, amplified and displayed on the computer screen, thereby forming an image. As a result of the strong elastically scattered signal, STEM resolution is fundamentally controlled by the probe beam dimension, which depends on electron source size and aberrations in condenser lens.

2.1.1 STEM imaging with different collection angles

In this thesis, we observed STEM images with different collection angles, depending on the experimental requirements. The collection angle is changed according to the camera length. HAADF/ADF/ABF collects the signals from the high/middle/low-angle scattered electrons. Detectors located above (Fischione company) and below (FEI company) the viewing screen were employed to observe HAADF and ABF images with STEM collection angles of 98.7–200 and 10.6–21.5 mrad, respectively, where a camera length of 77 mm was used. When EDX mapping was performed, we chose the HAADF detector (Fischione company) because the images it acquires exhibit Z-contrast. If EELS spectrum mapping was carried out, a lower camera length value was usually chosen so as to increase EELS spectrometer collection angle and hence enhance EELS signals. In this case, an ADF detector (Gatan company) located at the entrance of the GIF spectrometer with STEM collection angle approximately 26.6–96.3 mrad was adopted for imaging. Note that the collection angles for STEM imaging and EELS spectrum is different.

Figure 2.1 shows the schematic map of STEM-EELS spectrum imaging. When a high-energy electron beam is focused down to a small spot and scanned across the *xy* plane of the sample two-dimensionally, electrons elastically scattered to large angles are collected by an ADF detector placed below the sample, and build up an ADF image. Meanwhile, electrons inelastically scattered to smaller angles are allowed to pass through the annulus hole of the detector and enter into the electron energy-loss spectrometer located at the bottom of the microscope column. Spatially resolved EELS can thus be obtained when the structure is imaged, giving electronic (bonding) information along each projected atomic column. Additionally, characteristic X-rays generated in the specimen can be collected by EDX detectors and form EDX mapping. Therefore, using STEM it is not only possible to image structure directly [71], but also to measure compositional changes and electronic structure spectroscopically in two-dimensions [72].

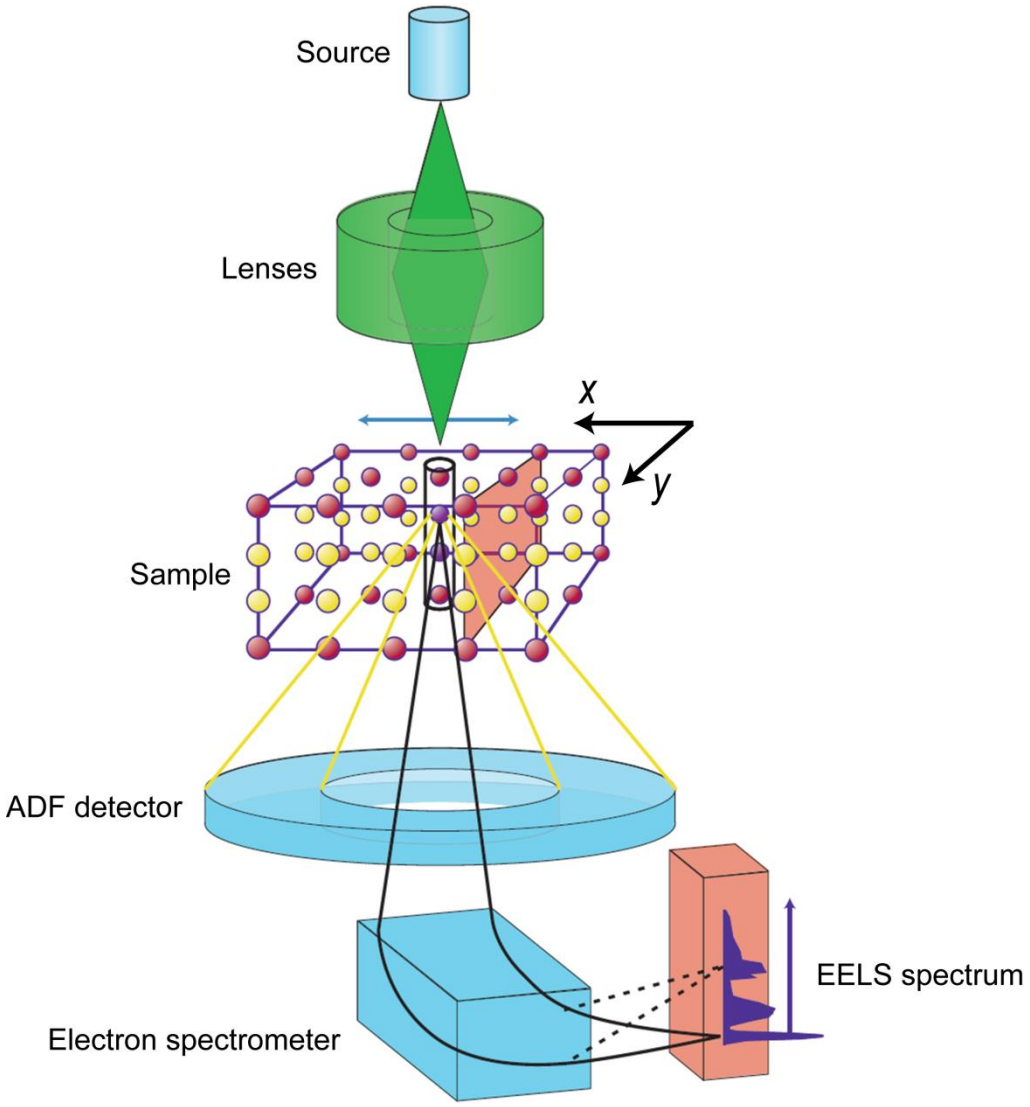

Figure 2.1 *Simultaneous acquisition of STEM image and EELS spectrum.* [73]

The HAADF detector forms Z-contrast image, whose brightness is approximately proportional to atomic number squared (Z^2) [74]. Thus HAADF is most sensitive to heavy atoms. In comparison, phase contrast dominates in the ABF image. ABF is capable of resolving both light (oxygen) and heavy atomic columns even in thick sample regions, providing highly localized positions of both columns. HAADF and ABF signals can be recorded simultaneously, see Figure 2.2.

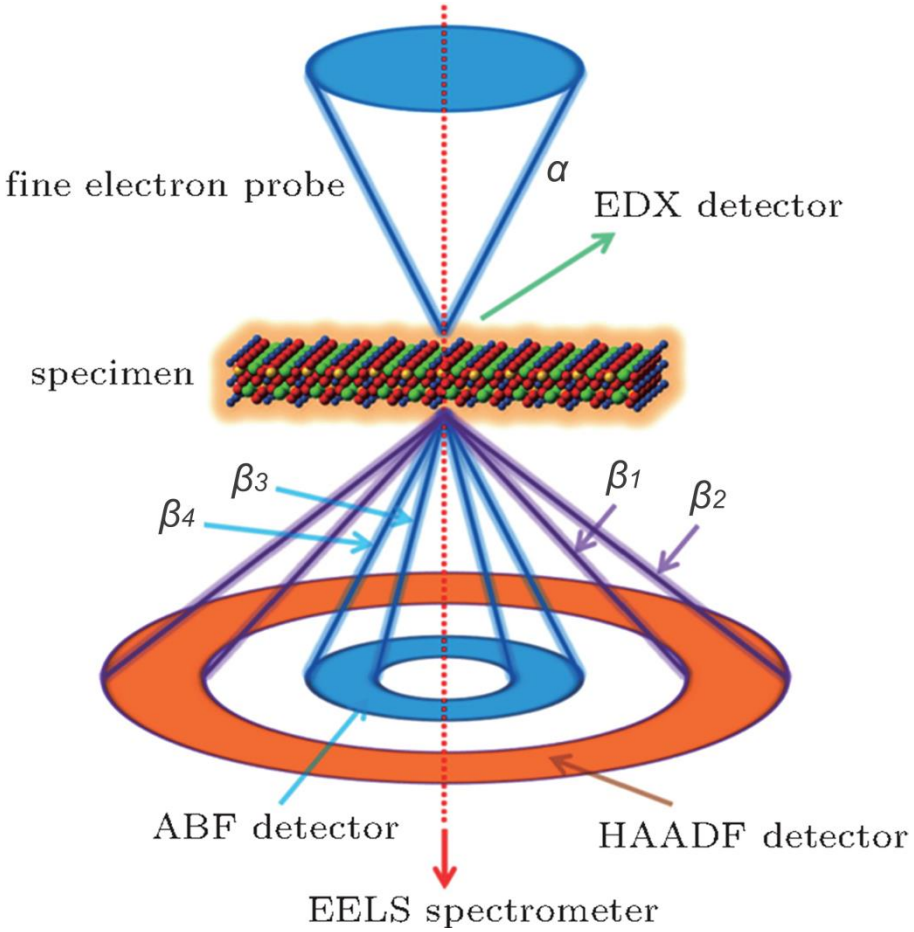

Figure 2.2 *Simultaneous collection of HAADF and ABF signals.* [75]

2.1.2 Probe-corrected STEM

Aberrations strongly influence STEM image quality, which can be improved by aberration correctors mounted in the illumination system. Currently, probe-corrected STEM has enabled sub-ångström resolution [50, 51, 53], being a powerful tool for studying atomic structures. Furthermore, the combination of probe-corrected STEM and EELS/EDX makes rapid elemental and chemical analysis at atomic-column scale feasible [73, 76-78].

In TEM bright field imaging, structural details are easily obscured by contrast variations that occur because of specimen thickness, crystal tilt, objective lens defocus and lattice strains.

While for HAADF these effects are less pronounced, enabling robust atom-resolved imaging that shows strong atomic-number contrast, which is especially useful for investigating defects or interfaces [79, 80]. Figure 2.3 illustrates simulated HRTEM images as a function of thickness and defocus. The image contrast varies obviously as the thickness and defocus shift, and interpretation is difficult.

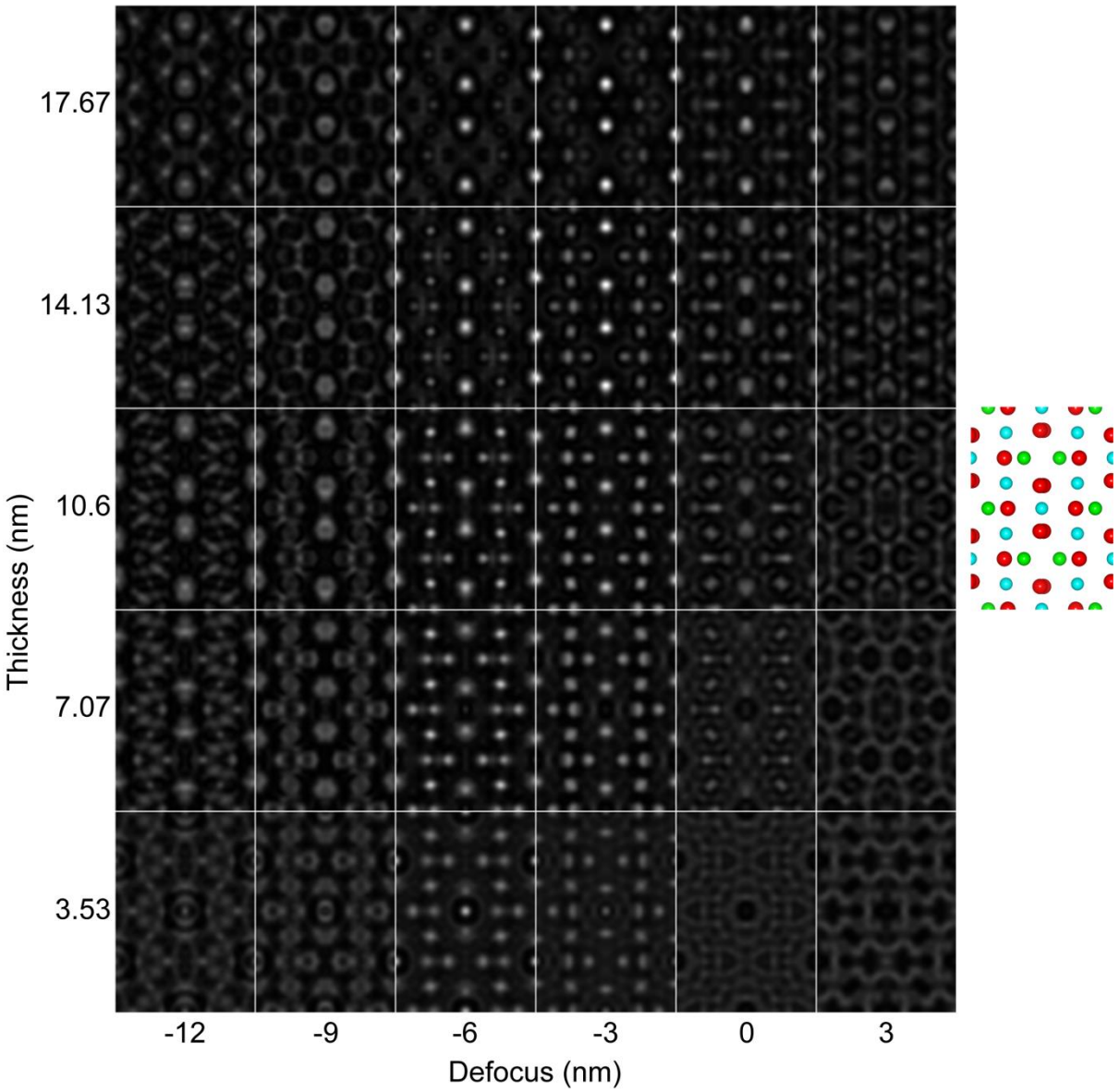

Figure 2.3 *Simulated HRTEM images of $ZnCr_2O_4$ viewed from the [1-10] direction, as a function of thickness and defocus. The atomic projection model is shown at the right. The green, cyan and red balls represent Zn, Cr and O, respectively.* [unpublished, Wei Zhan]

In order to compare with simulated HRTEM images, we also carried out STEM image simulations based on the same atomic model in Figure 2.3, as illustrated in Figure 2.4. Small

variations of specimen thickness usually do not affect the contrast of the HAADF image, while the ABF image contrast becomes darker gradually as thickness increases.

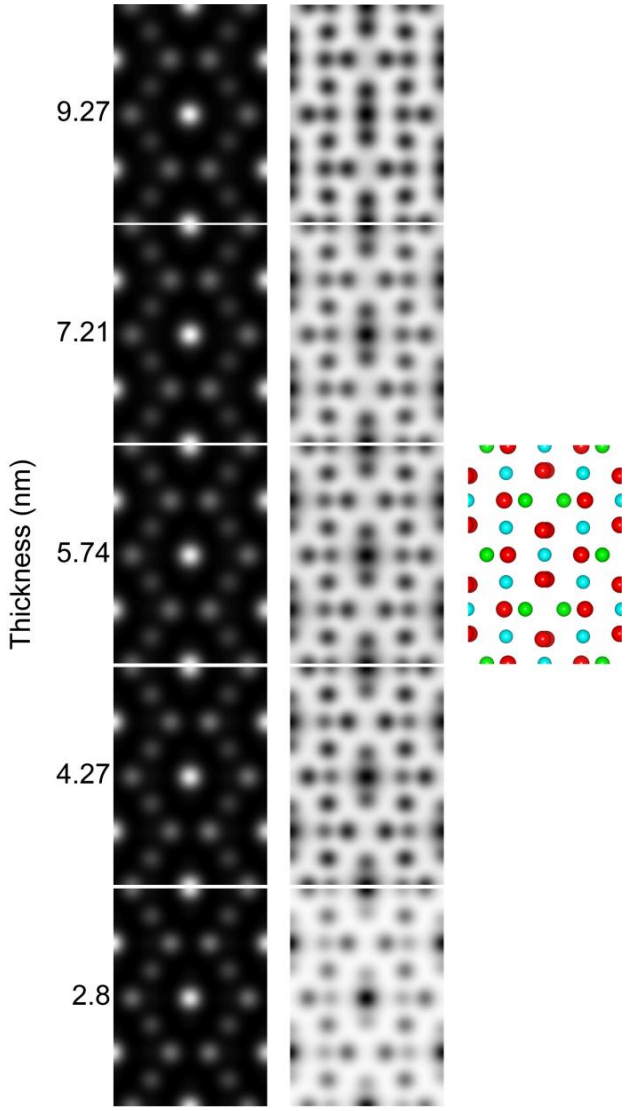

Figure 2.4 *Simulated HAADF and ABF images of $ZnCr_2O_4$ viewed from the [1-10] orientation, as a function of thickness. The atomic projection model is displayed at the right. The green, cyan and red balls represent Zn, Cr and O, respectively.* [unpublished, Wei Zhan]

In our STEM investigations, Au particles on the cross grading copper grid were employed to fine tune the astigmatisms including spherical aberration, where probe-corrector software was used. Table 2.1 gives the measured aberration value after probe-corrector tuning. The STEM images were acquired until the experimental conditions as listed below have been reached, spherical aberration C3 about 0 μm, two-fold astigmatism A1 < 5 nm, three-fold astigmatism A2 < 50 nm, axial coma B2 < 50 nm, four-fold astigmatism A3 < 1 μm, star aberration S3 < 1 μm.

Table 2.1 *Aberrations after tuning probe-corrector.* [unpublished, Wei Zhan]

Aberration	Measured value
defocus C1	< 5 nm
two-fold astigmatism A1	< 5 nm
three-fold astigmatism A2	< 50 nm
axial coma B2	< 50 nm
spherical aberration C3	~ 0 μm
four-fold astigmatism A3	< 1 μm
star aberration S3	< 1 μm

Under the experimental conditions summarized in Table 2.1, atom-resolved imaging and spectrum mapping of high quality have been achieved. As an example, Figure 2.5 illustrates high-resolution STEM imaging of wurtzite ZnO in the [$1\bar{2}10$] zone axis, with comparisons to simulated images using QSTEM that is based on the multi-sclice method [81]. HAADF imaging is very sensitive to heavy atoms, while observing light atoms, such as O, is more difficult. Thus, in the HAADF image shown in Figure 2.5(a), the columns corresponding to Zn atoms are easily observed, but there is no indication of the neighboring columns of O. In comparison, the ABF image in Figure 2.5(b) clearly displays both columns, but with the contrast reversed.

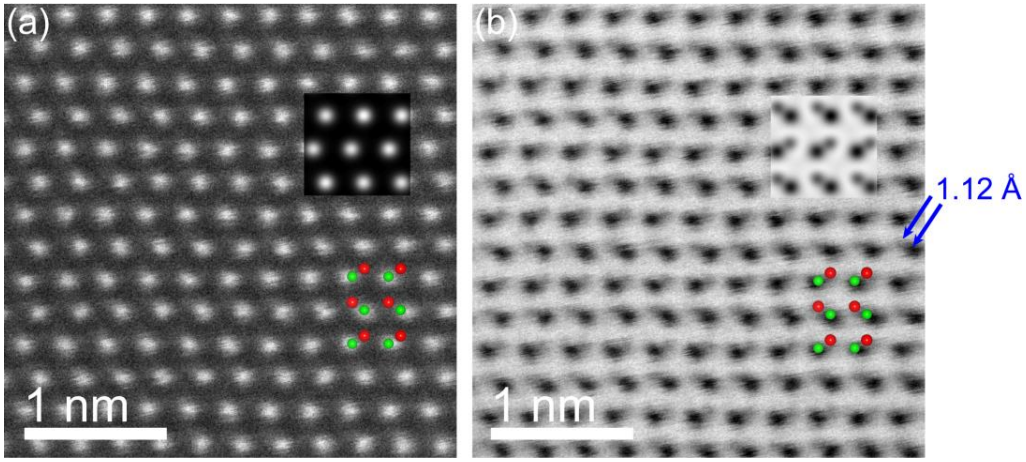

Figure 2.5 *(a) HAADF and (b) ABF images of ZnO viewed from the [1-210] direction. The upper right shows the simulated image based on the atomic projection model at the bottom right. The green and red balls represent Zn and O, respectively.* [unpublished, Wei Zhan]

We also realized structural and elemental imaging of $ZnCr_2O_4$ with atomic-resolution. In the [$1\bar{1}0$] zone axis, there are five different types of atomic columns in the hexagon unit, namely

four edge Cr, six edge Zn, one central Cr_2, two O_2 and four O near the center. The four Cr and six Zn columns form a hexagonal structure with Cr_2 in the center. These atomic columns show different contrast in the HAADF image (Figure 2.6(a)). At the edge of the hexagon, the Zn (Z=30) column is brighter than the Cr (Z=24) column as expected. However, the central Cr_2 column is much brighter than the edge Zn or Cr column, in seeming contradiction to the expected Z-contrast. In order to understand this, the ratio of the number of atoms in the five different columns has to be considered. For the central Cr_2 column, the edge Zn column, the edge Cr column, the O_2 column, and the O column, the ratio of the number of atoms is 2:1:1:2:1 in one unit of periodicity along the $[1\bar{1}0]$ direction. The total scattering strength of the different columns that scales as the sum of atomic numbers are 48, 30, 24, 16, 8, respectively, indicating a higher mass density and thereby higher scattering strength along the central Cr_2 column. EDX map with atomic resolution, as inserted at the left of the HAADF image, clearly identifies that the central atom with high brightness is Cr_2, while at the edge, the four dark atoms are Cr and other six bright atoms are Zn. This demonstrates that not only the atomic number, but also the atom ratio along each column need to be considered. In Figure 2.6(b), from Cr_2, Zn, Cr, O_2 to O column, the black contrast changes from deep to light. The two O_2 and four O atomic columns have slight different contrast and can be clearly distinguished. Here the closest distance between Zn and O is 1.14 Å.

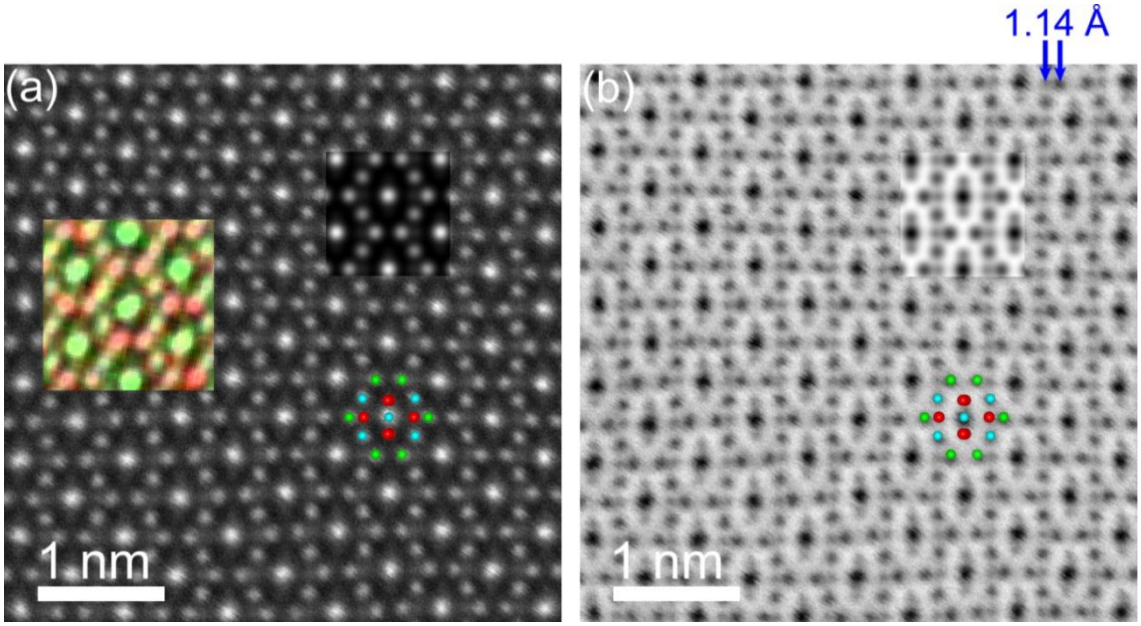

Figure 2.6 *(a) HAADF and (b) ABF images of $ZnCr_2O_4$ observed from the [1-10] orientation. The upper right shows the simulated image based on the atomic projection model at the bottom right. The green, cyan and red balls represent Zn, Cr and O, respectively.* [unpublished, Wei Zhan]

2.2 Electron energy-loss spectroscopy

2.2.1 EELS spectrum

Inelastic scattering occurs when there is an interaction between the incident beam and outer-shell electrons as well as inner-shell electrons in an atom. To detect these signals, the viewing screen, under which the GIF spectrometer is mounted, is removed. As illustrated in Figure 2.7, the inelastically scattered electrons pass a drift tube, and a magnetic field deflects them through ≥ 90°. This "magnetic prism" also compensates for the same energy-loss electrons with different paths (on-axis and off-axis), so that focusing in the dispersion plane happens. In addition, higher energy-loss electrons are deflected more than lower energy-loss ones, so in the dispersion plane, an EELS spectrum showing intensity (I) as a function of energy loss (E) is formed.

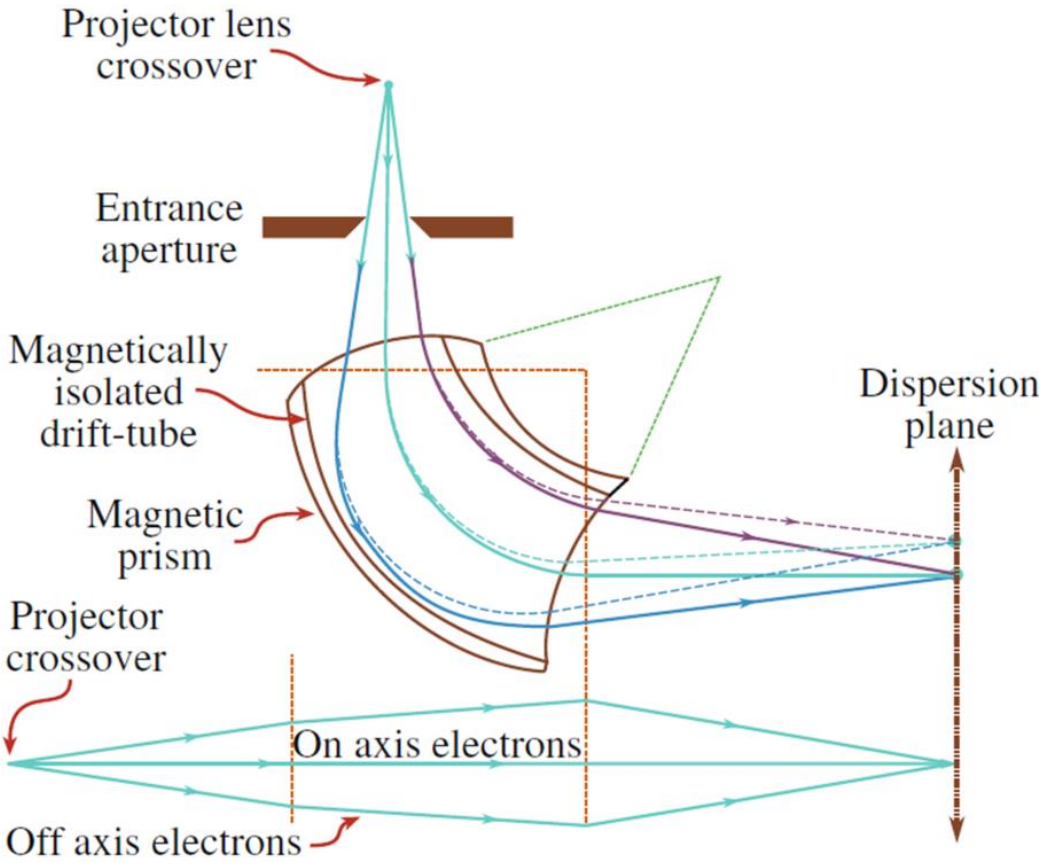

Figure 2.7 *Paths of inelastically scattered electrons through a GIF spectrometer. On-axis and off-axis electrons are focused in the dispersion plane. The bottom displays the lens focusing behavior.* [74]

Here we observe the energy loss by a beam of electrons to excitation processes in the sample. When an atomic electron in the initial state $|\psi_i\rangle$ absorbs energy from an incident electron, it

is excited into an empty state $|\psi_f\rangle$ above the Fermi-level. In the dipole-approximation of small scattering angles, the energy loss suffered by the incident electron corresponds to the double differential cross section of single electron excitation [55, 82]:

$$\frac{d^2\sigma(\boldsymbol{q},E)}{d\boldsymbol{q}dE} = \frac{4\gamma^4}{a_0^2\boldsymbol{q}^4}\rho(E)|\langle\Psi_\mathrm{f}|\mathrm{i}\mathbf{q}\cdot\mathrm{r}|\Psi_\mathrm{i}\rangle|^2 \tag{2.1}$$

Where σ is the integrated cross section, $\boldsymbol{q}$ is the momentum transfer, E is the difference in the energy of the final and initial states $E = E_f - E_i$, γ is the relativistic correction factor, a_0 is the Bohr radius, $\rho(E)$ is a joint density of states resulting from the convolution of the density of initial and final states, r is the coordinate of the fast electron.

EELS takes use of inelastic scattering that is elementally dependent, and can reveal both component and electronic structure [61]. The EELS spectrum is divided into low-loss (0–50 eV) and core-loss (above ~50 eV). As the energy loss raises, inelastic interactions occurs in the following sequence, inter/intraband transitions (1–20 eV), plasmon oscillations (5–30 eV), and inner-shell ionizations (50–2000 eV).

2.2.2 Monochromator

The energy resolution in an EELS experiment is usually defined by the full width at half maximum (FWHM) of the focused ZLP. It is to a large extent dictated by the energy spread of the electron source. For conventional electron sources, the energy spread is in the range of 0.8 eV (for Schottky field emission gun) down to 0.6 eV (for cold field emission gun). A monochromator can be mounted on the gun source. Its selecting slit cuts off the tail of ZLP and thus greatly improves the energy resolution. As displayed in Figure 2.8, a monochromator takes use of electric field and magnetic field to decrease the energy spread of the beam significantly. Only the chosen electrons with the specific velocity (v_0) are allowed to travel straight ahead, while other electrons are distributed spatially.

$$v_0 = \frac{E}{B} \tag{2.2}$$

Where E is electric field, and B is magnetic field.

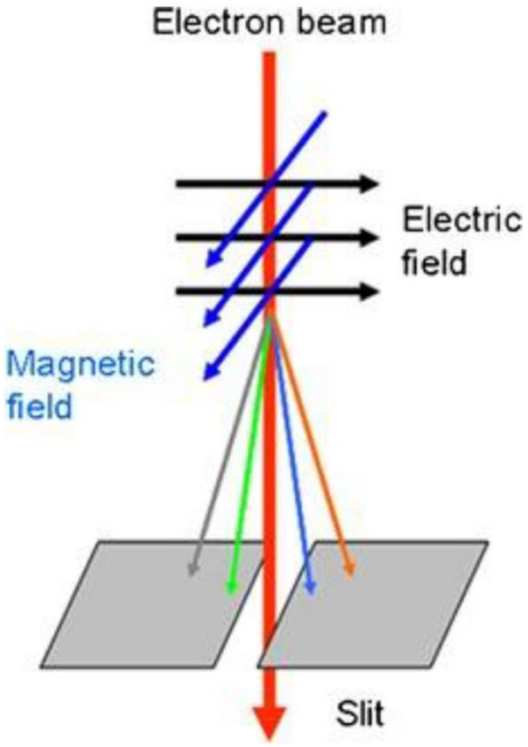

Figure 2.8 *Schematic image of a monochromator.*

Recent years have seen rapid development in the field of monochromated EELS, which has been successfully applied in measuring optical band gap with high spectral resolution of <0.2 eV [30, 55, 57]. In this work, an energy resolution of approximately 0.15 eV can be reached for monochromatic electrons. However, a monochromator is like a double-edged sword. It also greatly filters out the number of electrons, significantly reducing the beam intensity and thus making band gap mapping challenging. Probe forming correctors in our microscope allow the collection of more EELS signals within less time. More importantly, despite the reported complexity, the exposure time close to the limitation required by CCD, suitable specimen thickness, adequate acquisition time, and non-disturbance surroundings altogether make band gap mapping on the nanometer scale possible.

2.2.3 Low-loss EELS

The so-called low-loss region of the EELS spectrum (0–50 eV) has a relatively high intensity, and is composed of the ZLP and the low-loss portion up to ~50 eV. The ZLP includes elastic, forward-scattered electrons that retains the incident beam energy E_0, and electrons with very small energy losses below the resolution limit, usually the excited phonons. Generally, the ZLP is most intense in EELS spectrum as long as specimen is thin enough. A tail exists at both sides of the ZLP. On negative energy side, the tailing comes from the point-spread

function, while on the positive energy side, the low-loss electrons (phonon) are accounted for the tail. The energy losses up to ~50 eV result from the interaction between the high-energy electrons and the weakly bound electrons of outer-shells of the atoms. Plasmon, the second predominant feature after the ZLP, is situated in this range. Plasmon peak detects energy loss of incident beam that have interacted with weakly bound conduction/valence band electrons. Low-loss EELS is characteristic of the dielectric properties, and the EELS spectrum can be described by the dielectric function through the following relationship:

$$I(E) \propto Im\left(\frac{-1}{\varepsilon(E,\boldsymbol{q})}\right) = \frac{\varepsilon_2}{\varepsilon_1^2 + \varepsilon_2^2} \tag{2.3}$$

Where $I(E)$ is the intensity of EELS spectrum, ε is the dielectric function, E is energy loss, $\boldsymbol{q}$ is the scattering vector, ε_1 and ε_2 are real and imaginary parts of the dielectric function, respectively. For example, dielectric function (ε_1, ε_2), theoretical (based on dielectric function) and experimental EELS spectra of ZnO are presented in Figure 2.9. In order to provide a convenient comparison, the background of the ZLP in the experimental EELS spectrum was subtracted, where the power law model (see Equation (2.6)) was employed and the fitting range 2.4–2.9 eV was used. A basic similarity is found between experimental and theoretical EELS spectra of ZnO.

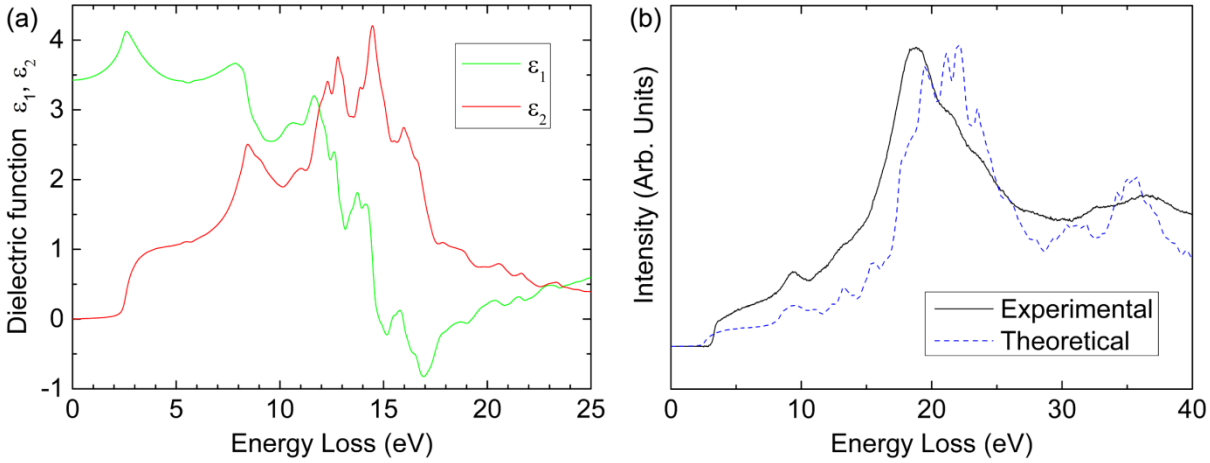

Figure 2.9 *(a) Derived complex dielectric function ($\varepsilon = \varepsilon_1 + i\,\varepsilon_2$). (b) Experimental and theoretical EELS spectra of ZnO.* [unpublished, Espen Flage-Larsen]

2.2.4 EELS band gap

In an EELS spectrum of a semiconductor or insulator, the band gap is a forbidden-transition region between the ZLP and the rise in intensity preceding the plasmon peak. No interband transitions occur in this portion of the spectrum. To analyze the band gap, an energy loss

model is fitted to the spectrum, before which the tail of the ZLP is removed.

(a) Cherenkov radiation

If only interband transitions are considered, the smallest energy loss suffered by the incident electron corresponds to the excitation of an electron from the valence band maximum (VBM) to the conduction band minimum (CBM), based on which accurate band gap can be measured. However, other energy loss processes occur in addition, and care must be taken to identify and avoid the various effects that may interfere with the measurement, or even mask the band gap transition completely. One of the most severe effects is the generation of Cherenkov photons with wavelength in the visible range, thereby overlapping the band gap in the EELS spectrum. This occurs when the speed of the electron (v_e, determined by the accelerating voltage of the TEM) is higher than the speed of light in the material (c) as determined by the refractive index $n(\lambda)$:

$$v_e > c = \frac{c_0}{n(\lambda)} \tag{2.4}$$

Where c_0 is the speed of light in vacuum.

In the case of ZnO, typical values for the refractive index in the visible range fall between $n \approx 2.0 - 2.5$ [2]. Thus, to fully avoid the generation of Cherenkov photons, an electron speed lower than $0.4 - 0.5c_0$ should be utilized, corresponding to accelerating voltages below 45−80 kV. In this study, an accelerating voltage of 60 kV was used, thereby reducing, but not completely eliminating the probability of generating Cherenkov photons. In order to assess the possible impact, we calculate the emission probability following the work of Erni and Browning [56]:

$$P^* = 1 - \frac{c_0^2}{v_e^2\, n(\lambda)^2} = 1 - \frac{(eU + m_0{c_0}^2)^2}{n(\lambda)^2 eU(eU + 2m_0{c_0}^2)} \tag{2.5}$$

Where P^* is an emission probability per unit path length normalized to the maximal emission rate in a bulk sample, m_0 is the electron mass, e is the elementary charge, U is the high tension, c_0 is the speed of light. With a TEM high tension of 60 kV and the refractive indices quoted above, an emission probability of 0.2−0.3 is found. This is low enough that we do not expect any considerable contribution in the energy loss spectrum from Cherenkov losses. The specimen of less than 30 nm in the present work further limited such retardation loss efficiently. Other factors, such as surface plasmon and guided light modes, are also not

significant in this study due to the sample thickness and the low emission probability [56]. These are confirmed by the similar band gap values of ZnO obtained from our EELS measurements and CL analysis.

(b) Direct and indirect band gaps

For a direct band gap, the smallest gap separation is vertical, as illustrated in Figure 2.10(a). Only a photon is required to excite an electron from the valence band to the conduction band, while leaving a hole behind, thereby causing optical transitions labelled $\Delta k \approx 0$ to occur. While for indirect band gap materials (Figure 2.10(b)), the smallest thermodynamic gap involves a momentum transfer. Both a phonon and a photon are needed to enable optical band gap transitions. The momentum can be conserved by emission or absorption of a phonon, thus making the transitions with $\Delta k \neq 0$ possible. As can be seen from Figure 2.10(c)-(d), different fitting equations were utilized to extract the direct and indirect band gaps in an EELS spectrum. An example of direct and indirect band gaps of GaN analyzed by EELS is given in Figure 2.10(e).

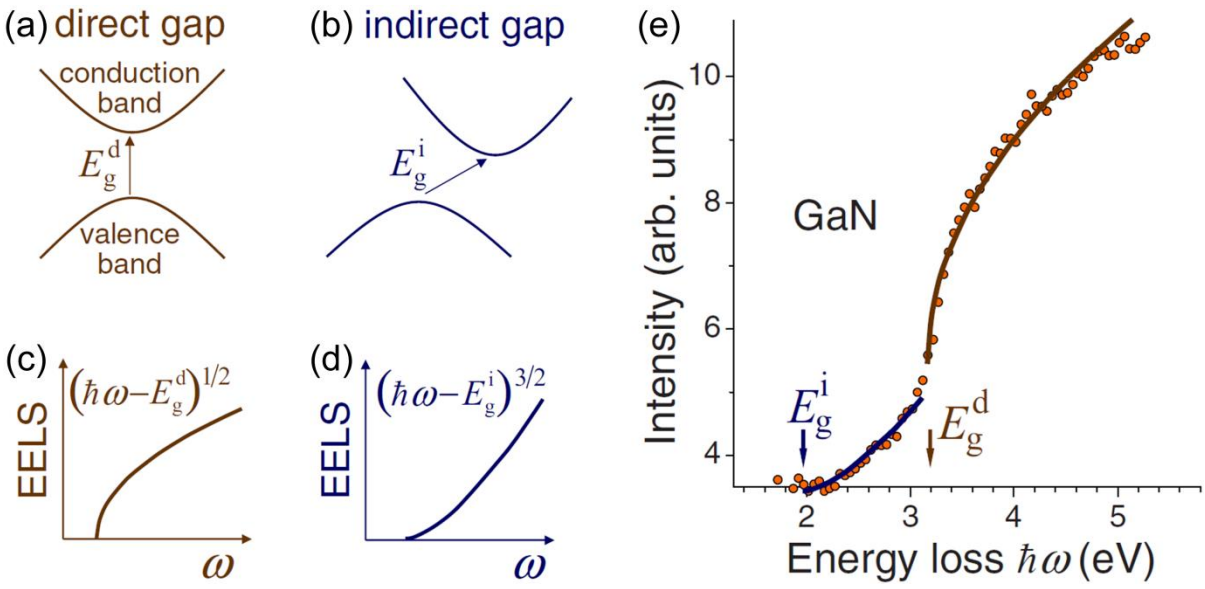

Figure 2.10 *(a) Direct and (b) indirect band gap structures. (c) Direct and (d) indirect band gaps analysis adopting EELS. (e) Direct and indirect band gaps fitting in GaN.* [82-84]

(c) Background subtraction and band gap fitting

Monochromated EELS can provide the band gap information of the specimen, and in combination with probe-corrected STEM the spatial variation of the band gap can be investigated. The acquisition is set up in the form of spectrum images, where the beam is

scanned in two spatial dimensions with an energy-loss spectrum associated with each pixel. Adopting this method the band gap can be mapped across two spatial dimensions. Band gap mapping was computed using the same method as described previously [29, 63, 85]. Briefly, the band gap is found by aligning all spectra to the ZLP maximum, removing the background and making a curve fit in order to identify the energy loss onset. An example of extraction of the band gap from an EELS spectrum of ZnO is given in Figure 2.11. The background subtraction consists of removing the intensity from the descending tail of the ZLP, which extends into the region around the band gap. The background was fitted and subtracted on the basis of power law model.

$$J(E) = AE^{-r} \tag{2.6}$$

Where A is scaling constant, r is slope exponent. This approach was found to give more robust and reproducible results than subtracting a pre-measured ZLP in vacuum. One reason is that the FWHM of ZLP measured on the specimen is slight different than that acquired in the vacuum hole as a result of elastic-scattering and phonons effects. For the purpose of obtaining the best band gap fit, the background must be removed completely, as additional intensity will shift the band gap fitting and bring about a lower value. Figure 2.11(a) displays background subtraction adopting power-law method for extracting ZnO band gap.

After subtracting the background, the spectra probably contains a high level of noise and a low signal intensity which reduce the accuracy of the band gap fitting. If so, binning was performed by summing neighbouring spectra of the spectrum image and Sawitsky-Golay smoothing filters were applied to enhance the signal and reduce the random noise. Thereafter the band gap was obtained through fitting a curve to the band onset of each spectrum. As shown in Figure 2.10(c), in the case of a direct band gap, a parabolic band approximation is employed, and the ideal energy loss intensity close to the band gap E_g is described as follows [82].

$$I(E) = c\sqrt{E - E_g} \tag{2.7}$$

Where $I(E)$ is the intensity of energy loss, c is a scaling factor, and E is the energy loss of the incident electron. Using MATLAB software for fitting this function to the band onset, the scaling constant c and the band gap E_g were fitted by a customized fitting approach. This method is a nonlinear algorithm which ignores the intensity below the fitted band gap, such

as noise and residual intensity below the band onset, and is described elsewhere [85]. The fitting was performed and the onset was identified for each spectrum in the spectrum image, thereby creating a spatial map of band gap energies. Figure 2.11(b) shows a parabolic fitting utilized to obtain ZnO band gap.

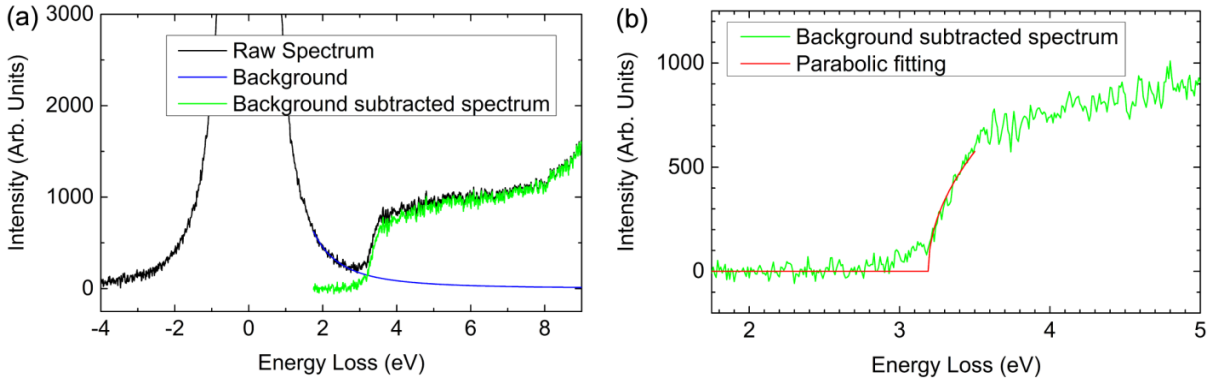

Figure 2.11 *(a) Background subtraction for an EELS spectrum of the ZnO layer in the* $Zn_{1-x}Cd_xO/ZnO$ *thin film; (b) Band gap extraction by parabolic fitting.* [unpublished, Wei Zhan]

(d) Background range

In this study, monochromated EELS in conjunction with probe-corrected STEM is capable of mapping band gap two-dimensionally. Table 2.2 gives an outline of the average band gap values of the pure ZnO layer extracted from 200 points with 2×2 binning and different background subtraction ranges. To assess the precision of the measurements, the energy spreads as expressed by the standard deviation (σ) are also listed. As is shown, the fitting range for background subtraction influences the average value as well as standard deviation of acquired band gap, although these effects are small. When the interval (from minimum to maximum) of background subtraction range is 0.3 eV, a standard deviation of 0.03 eV is found. If the interval increases to 0.5/0.75/1 eV, the standard deviation becomes 0.02 eV. Moreover, when the maximum point of background subtraction range is close to the band gap onset, higher average onset values are found. When the background subtraction range is 2.6−2.9/2.15−2.9 eV, an average band gap value of 3.21 eV is obtained. If the background subtraction range shifts to 2.4−2.9 eV, we acquire an average band gap of 3.22 eV. With a view to obtain the most accurate onset values, the best fitting range should be close to the band gap onset and cause less standard deviation σ. Therefore, in the current band gap mapping of the pure ZnO layer [29], the fitting range 2.4−2.9 eV was utilized for removing background, and an average band gap of 3.22 eV with standard deviation of 0.02 eV was found, as also confirmed by CL measurements.

Table 2.2 $\overline{E_g}$ *of ZnO with different background subtraction ranges.* [unpublished, Wei Zhan]

Background subtraction range (eV)	$\overline{E_g}$ **of ZnO layer (eV)**	**σ (eV)**
2.0-2.3, 2.1-2.4	3.19	0.03
2.2-2.5, 2.3-2.6	3.20	0.03
2.4-2.7, 2.5-2.8, 2.6-2.9	3.21	0.03
1.75-2.25, 1.8-2.3, 1.85-2.35, 1.9-2.4, 1.95-2.45, 2-2.5	3.18	0.02
2.05-2.55, 2.1-2.6, 2.15-2.65	3.19	0.02
2.2-2.7, 2.25-2.75	3.20	0.02
2.3-2.8, 2.35-2.85	3.21	0.02
2.4-2.9	3.22	0.02
1.55-2.3, 1.65-2.4, 1.75-2.5, 1.85-2.6	3.18	0.02
1.95-2.7	3.19	0.02
2.05-2.8	3.20	0.02
2.15-2.9	3.21	0.02
1.6-2.6, 1.7-2.7	3.18	0.02
1.8-2.8	3.19	0.02
1.9-2.9	3.20	0.02

The absolute values of the ZnO band gap listed in Table 2.2 are a little lower than the fundamental gap usually cited for ZnO (≈ 3.3 eV). Bear in mind that the EELS spectrum measures the optical band gap, known as the onset of absorption, which is lower than the fundamental gap due to the large exciton binding energy of ZnO as well as crystalline quality, grain size, defects, and strain which can also cause a drop in the optical band gap [86-91]. There is a summary with respect to band gap values of ZnO thin films characterized by different techniques from Bundesmann et al [92], who revealed that the observed optical band gap is from 3.195 eV to 3.44 eV, with most values clustering from 3.24 eV to 3.28 eV. Taking the expected systematic underestimation discussed previously into consideration, the band gap values observed here are in good agreement with existing investigations, and both high accuracy and precision are maintained.

(e) An example of EELS band gap mapping

In this work, high quality EELS mappings were employed to support the high spatial resolution measurements of optical band gaps on the nanometer scale. We chose one pixel

from the Cd-containing and pure ZnO pure layers of the EELS spectrum map of the $Cd_{0.16}$ sample. The arrows in Figure 2.12 display the corresponding band onsets of $Zn_{1-x}Cd_xO$ and ZnO. Here it can be seen that $Zn_{1-x}Cd_xO$ has a lower band gap than ZnO, and the signal strength of the EELS spectra is adequate.

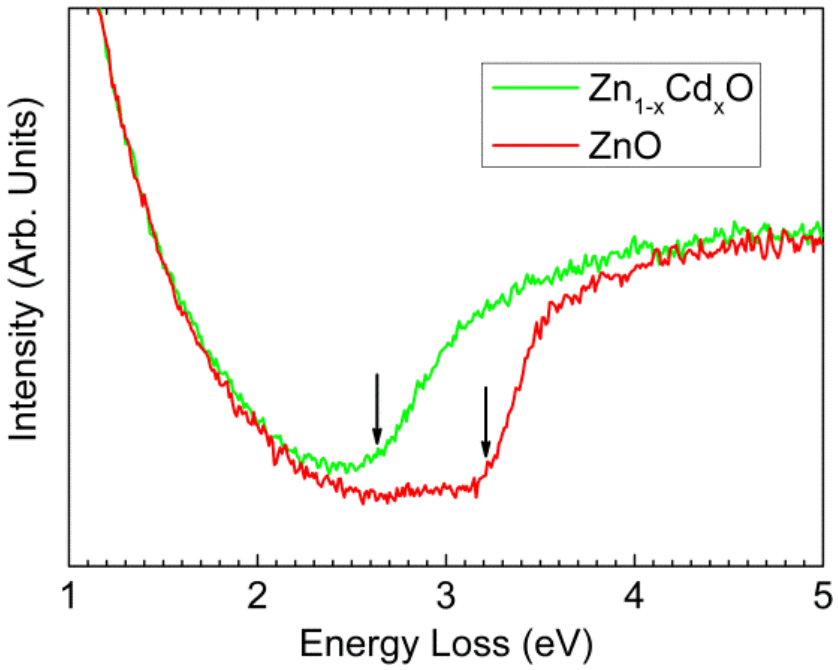

Figure 2.12 *EELS spectra of $Zn_{1-x}Cd_xO$ and ZnO.* [unpublished, Wei Zhan]

EDX was employed for the characterization of elemental composition. The structural homogeneity can thus be directly observed, and a direct correlation between the spatial distribution of Cd and band gap can be obtained. To give a review of the whole film, we performed band gap and chemical mapping of some large regions. Figure 2.13 illustrates a typical band gap map together with elemental EDX maps taken from the same area of the $Cd_{0.16}$ specimen. Binning 2×2 is adopted in the band gap map, and even the area is as large as 230 nm (height) × 210 nm (width), a high level of precision of 0.02 eV is found at the pure ZnO layer, see Figure 2.13(d). Additionally, it is apparent that the E_g and EDX maps matches very well, and at the outer layer of ZnO heavily alloyed with Cd, increasing (lower) Cd content *x* is associated with reduced (higher) band gap. For example, in the band gap map, a shift of 0.2 eV is clearly observed between the Cd poor and rich regions. It is also shown that the sufficient sensitivity of EELS enables detecting changes in band gap due to small compositional variation.

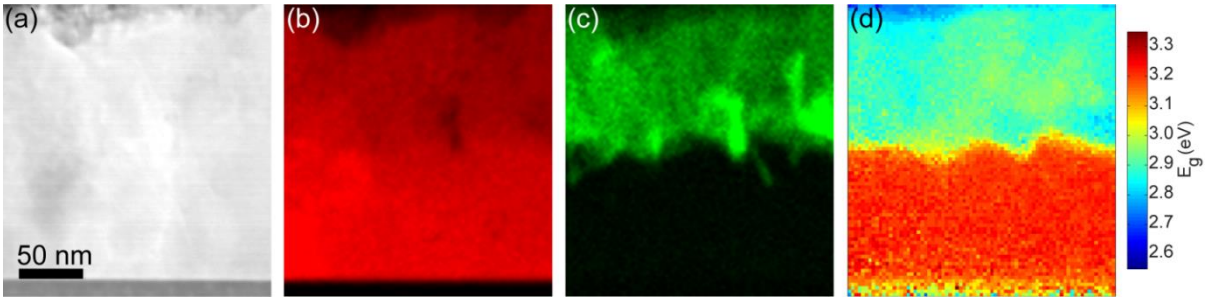

Figure 2.13 *(a) ADF image of $Zn_{1-x}Cd_xO/ZnO/\alpha$-Al_2O_3. EDX maps of (b) Zn and (c) Cd. (d) E_g map.* [unpublished, Wei Zhan]

2.2.5 EELS plasmon energy

When there is an interaction between a beam electron and the weakly bound electrons in the conduction or valence band of an atom, plasmons are generated. These are longitudinal wave-like oscillations of the valence electrons. The plasmon is therefore phase characteristic instead of atom characteristic, as the specimen composition has an impact on the valence-electron density (n), thereby giving rise to shift in the plasmon peak position. In some binary alloy composed of alloyed elements with significantly variable concentrations, a quantitative curve can be developed to relate plasmon energy and composition. This can be used to determine composition of unknown alloys on the basis of measured shifts of plasmon peak, see related investigation [93]. So the plasmon energy can reveal chemical information.

In addition to the free electron density, the unit cell volume also strongly influences the plasmon energy, as can be seen from the following equations. In free electron model, the electrons are supposed to be free (not bound to any atom or ion), and the incident electron beam has the following energy loss defined by free electron plasmon energy [61]:

$$E_{p,F} = \hbar\omega_p = \hbar\sqrt{\frac{N}{V(x)}\frac{e^2}{m_0\varepsilon_0}} \tag{2.8}$$

Where $E_{p,F}$ is the free electron plasmon energy, ω_p is the plasmon frequency, $\hbar$ is the reduced planck constant, N is the number of valence electrons in a unit cell, e is the elementary charge, $V(x)$ is the unit cell volume which relies on alloyed element content x, m_0 is the electron mass, and ε_0 is the permittivity of free space.

For semiconductors with wide band gap, damped oscillations with frequency $\omega_b = E_g/\hbar$ would arise from the core electrons and positive ion, and also need to be considered.

Accordingly the free electron model can be modified, leading to semi-free electron model with the following plasmon energy [61]:

$$E_{p,sF} = \sqrt{E_{p,F}^2 + E_g^2} \tag{2.9}$$

The variations in specimen thickness influence plasmon peak intensity, but do not change the position of the plasmon-loss peak. Thus the accurate plasmon energy can be extracted even specimen varies in thickness. The thickness of a specimen can be given by the low-loss spectrum.

$$t = \lambda \ln \frac{I_t}{I_0} \tag{2.10}$$

Where t is specimen thickness, λ is the mean free path, I_t is the total intensity of the spectrum, and I_0 is the intensity of the ZLP.

In this thesis, we mapped how plasmon energy varies spatially [63], and direct extraction methods can be used because plasmons are often seen as distinct peaks in the low loss spectrum. First we adopted the Fourier-log method to remove plural scattering in DigitalMicrograph. Plasmon energy maps were then created by selecting energy windows, fitting a Gaussian function and mapping the spatial variation of the energy corresponding to the maximum intensity.

A representative plasmon energy map, together with band gap and elemental EDX maps taken from the same region of the $Cd_{0.16}$ sample, are displayed in Figure 2.14. The image size here is 236 nm (height) × 87 nm (width). The α-Al_2O_3 substrate is at the bottom, as can be seen from Figure 2.14(a)-(b). α-Al_2O_3 plasmon energy is >19 eV, and the color is white in Figure 2.14(e). Note that the plasmon energy of α-Al_2O_3 lies beyond the range of this study. The signals of band gap and plasmon energy were collected simultaneously, and the two maps in Figure 2.14(d)-(e) exhibit pixel-to-pixel correspondence, which are highly beneficial for the analysis of their relevance. At the ZnO pure, we find the high degrees of precision for both E_g and E_p, which are adequate for building their quantitative relevancy. Importantly, there is a very good spatial correlation between the observed plasmon and band gap energies. The variation resemblance at the outer layer of ZnO heavily alloyed with Cd is striking. As supported by elemental EDX maps, increasing (reduced) Cd content x brings about lower (raising) E_g and E_p here. Interestingly, some small variations, which can not be detected in

the band gap map, are observed in the plasmon energy map. This stems from the fact that the spatial resolution in plasmon energy map is better than band gap map. It needs to be mentioned that previous investigations reported that strain has an effect on band gap [64] as well as plamon energy [94]. There is also work showing that strain is related with unit cell parameter [95]. As described earlier, band gap and plasmon energy of $Zn_{1-x}Cd_xO/ZnO$ are both associated with unit cell parameter. These lead us to think that the correlation among unit cell parameter, strain, band gap and plasmon energy may deserves further research. In addition, when the annealing or *in-situ* STEM heating reaches a specific high temperature, spinodal decomposition might happen in the $In_{0.72}Al_{0.28}N$ or $Ti_{0.34}Al_{0.66}N$ alloy on the nanometer scale, see existing publications [96, 97]. In this work, the film growth temperature (370 ℃) and the STEM experimental temperature (~25 ℃) are both much lower than the critical temperatures in the above papers. Although no spinodal decomposition was found by our XRD measurements, care must be taken.

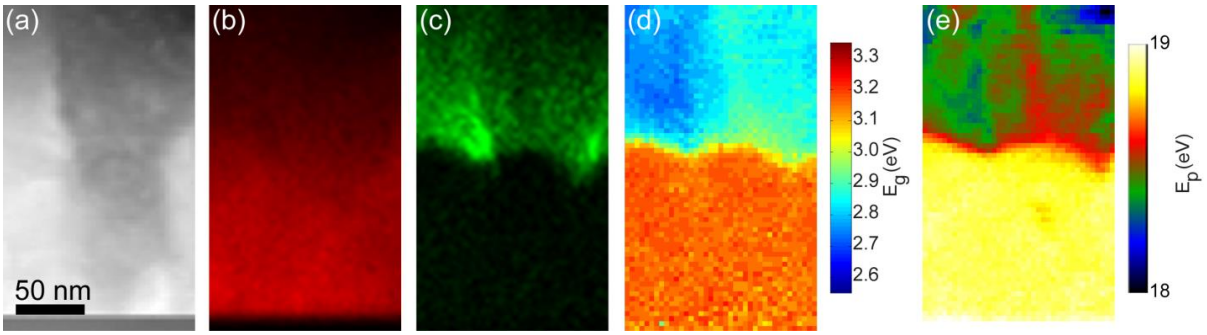

Figure 2.14 *(a) ADF image of $Zn_{1-x}Cd_xO/ZnO/\alpha\text{-}Al_2O_3$. EDX maps of (b) Zn and (c) Cd. Simultaneously measured (d) E_g and (e) E_p maps.* [unpublished, Wei Zhan]

2.2.6 Core-loss EELS

Core-loss EELS above ~50 eV is composed of inner-shell ionizations or core-loss edges. It probes the local density of states (above E_F) surrounding the excited atom. In the case of small scattering angles, the dipole selection rule applies, and the density of states with symmetry $\Delta l \pm 1$ compared to the initial state is probed.

The core-loss EELS spectrum originates from interactions with the more tightly bound, core-shell electrons. The core electron receives energy from the incident beam and is ejected from the inner shell, but does not escape to the vacuum level. Finally it belongs to an energy level above the Fermi energy (E_F), and is still bound to the Coulomb attraction of the nucleus. The

core electron can be ejected to any of the empty states in the conduction band. The probability of the excited electron residing in each possible unfilled state is unequal.

Ionization losses process can directly characterize the atomic column involved. When Z increases, *K*-shell electrons become more bound to the nucleus, and need more energy to be ejected. The probability of ionization displays a sharp rise to maximum when beam energy comes close to the critical ionization energy (E_C), and decreases slowly toward the background above E_C.

When the core electrons receive energy more than E_C from the incident beam and are ejected from the inner shell, energy-loss near-edge structure (ELNES) and extended energy-loss fine structure (EXELFS) take place. Bonding effects bring about fine structure oscillations within ~50 eV above E_C, which is named ELNES. The position of the ionization edge is controlled by the energy levels of the ionized shell, while the change of edge shape is dependent on whether certain energy states are filled or unfilled. On certain ionization edges, the white lines, which can be employed to characterize the oxidation state, occur as intense sharp peaks when the core electrons in certain elements are excited to well-defined empty states [74, 98, 99]. In comparison, EXELFS are weak oscillations that extend out several hundred eV above the ionization edge onset [61, 74]. The detailed intensity variations of ELNES and EXELFS are characteristic of the chemical bonding and coordination of the target atom and its DOS above E_F. An example of core-loss EELS spectra of Zn-$L_{2,3}$ edges is given in Figure 2.15. Zn-$L_{2,3}$ edge of $ZnCr_2O_4$ has obviously distinct features compared to that of ZnO.

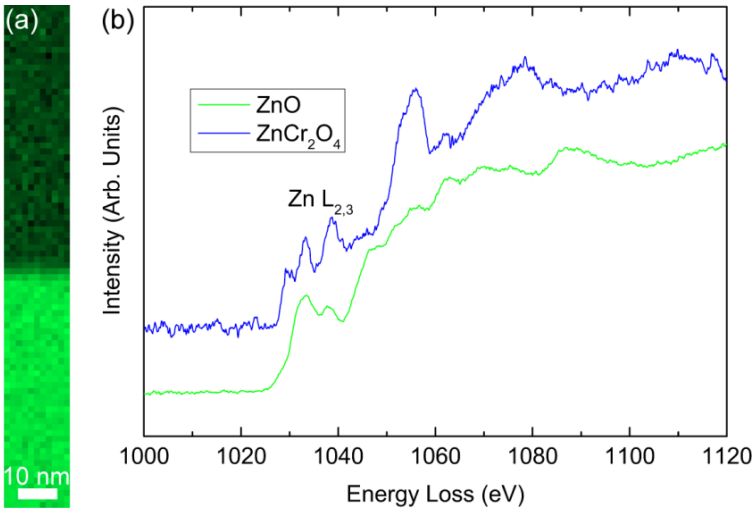

Figure 2.15 *(a) Core-loss EELS map of ZnO/$ZnCr_2O_4$ interface using Zn-$L_{2,3}$ edge. $ZnCr_2O_4$ and ZnO are situated at the top and bottom, respectively. (b) EELS spectra of Zn-$L_{2,3}$ edges of ZnO and $ZnCr_2O_4$.* [unpublished, Wei Zhan]

Ionization-loss imaging has been put into wide-spread application with high spatial resolution and single-atom detection sensitivity, especially in the field of quantitative analysis [68]. Egerton's ratio equation is employed to quantify EELS ionization edges. First the background is subtracted adopting power law model. Thereafter the edge intensity (I) is integrated for each element A, B, thereby obtaining atom number (N). The partial ionization cross section (σ) is the factor that relates atom number and edge intensity, thus σ is determined to get the ratio N_A/N_B [61, 74]. It needs to be pointed out that specimen thickness needs to be taken into consideration for the purpose of accurate quantification. When the specimen is very thin, each electron only experiences one scattering event at most, implying single scattering, and the quantification afterwards is straightforward. Usually, sample thickness less than one mean free path (<< 50 nm) is required for EELS analysis. In practice, specimen may be thicker than ideal, and each electron would undergo several (> 1 and < 20) interactions, resulting in plural scattering which is necessary to be removed though deconvoluting methods before any quantification.

2.3 Energy-dispersive X-ray spectroscopy

To generate characteristic X-rays, an incident electron beam with an energy E_0 larger than the critical energy E_C of the process is focused into the specimen. For an elemental atom within the sample, one of its electrons in an inner shell is excited and ejected, leaving an electron hole behind. Thereafter an electron from an outer shell with higher energy fills the hole, thus an X-ray photon with energy corresponding to energy difference between the outer and inner shells, is emitted.

The EDX setup is composed of four primary components, which are the electron beam, the X-ray detector, the pulse processor, and the analyzer. Figure 2.16 describes excitation and detecting process of EDX signals in the microscope. In X-ray fluorescence spectrometers, X-ray beam excitation occurs. The silicon drift detector (SDD) converts X-ray energy into voltage signals, which is sent to a pulse processor and measured. Thereafter an analyzer collects, processes and displays the signals. SDD has many benefits, consisting of high count rate collection and processing, better resolution than traditional detectors, less time in processing X-ray event, fast analysis and precise X-ray mapping.

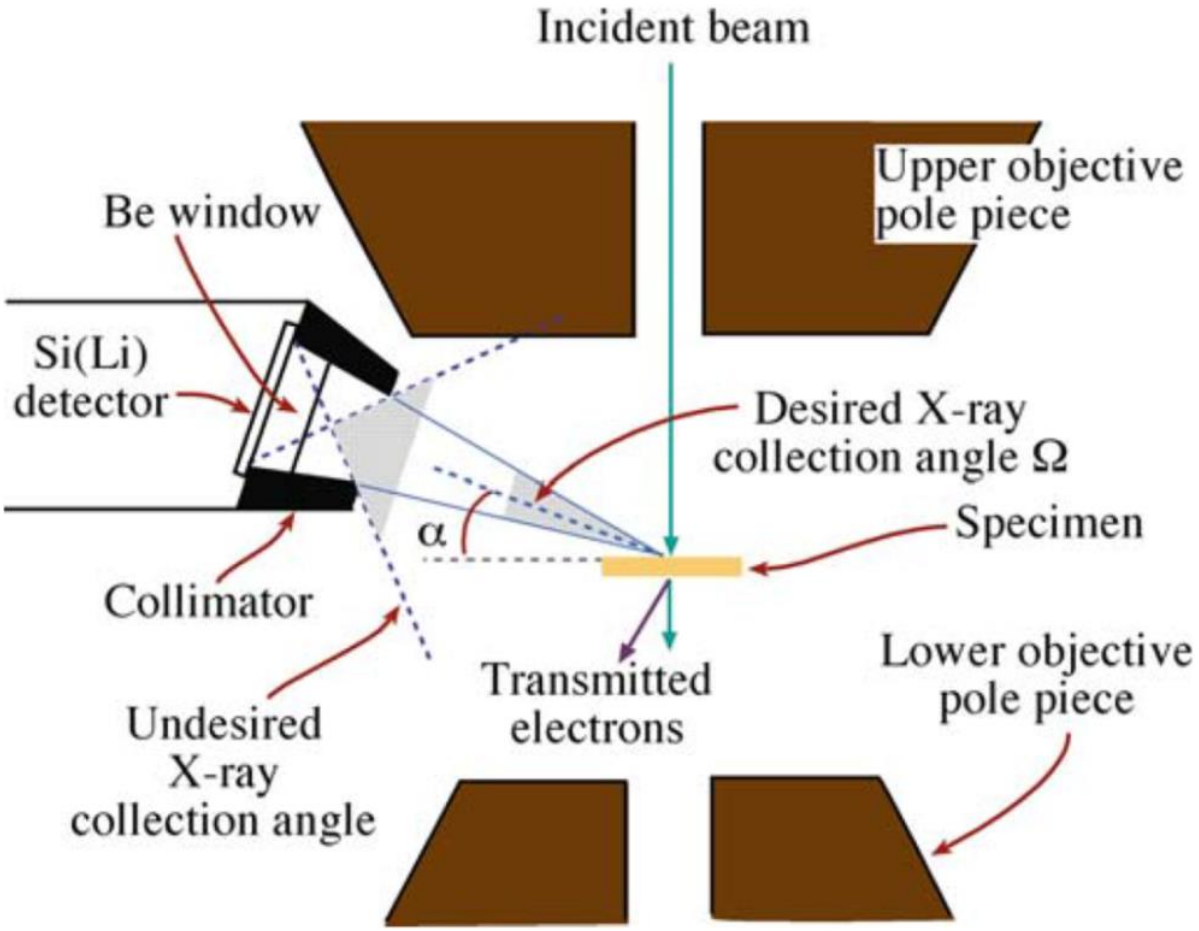

Figure 2.16 *Schematic picture of acquiring EDX spectrum in the microscope.* [74]

Producing a characteristic X-ray has the following probability as defined by the fluorescence yield ω [74].

$$\omega = \frac{Z^4}{a + Z^4} \tag{2.11}$$

Where Z is atomic number, a is a constant depending on the shell.

As can be seen from the above equation, the higher the atomic number, the higher probability of exciting EDX signals. EDX offers identification and quantification of elements above Li with a high level of spatial resolution and analytical sensitivity. The unique atomic structure in each element results in a unique set of peaks, and this forms the fundamental principle of EDX characterization. EDX quantification takes use of Cliff-Lorimer k-factor method. k-factors are sensitive to acceleration voltage, detector, background subtraction, and peak-integration. To achieve the best accuracy, the determination of k-factors relies on the particular experimental setup. Moreover, it is worth pointing out that, characteristic peaks

without overlapping should be chosen for quantification of the elements, before which the background of each peak is removed.

In this work, four FEI super-X EDX detectors as mounted in the FEI Titan G2 60−300 microscope can collect much more signals than traditional settings, greatly enhancing the accuracy of quantifying element composition. Figure 2.17 illustrates STEM-EDX maps of nano $ZnCr_2O_4$ inclusions embedded in ZnO matrix. There is one $ZnCr_2O_4$ nanoparticle formed in ZnO matrix, as can be judged from EDX map of Cr, see Figure 2.17(c). In the elemental EDX map of Zn (Figure 2.17(b)), a big intensity difference is found between the $ZnCr_2O_4$ nanoparticle and ZnO matrix. Moreover, even the difference of oxygen intensity in O EDX map can be clearly seen between the two phases, as presented in Figure 2.17(d).

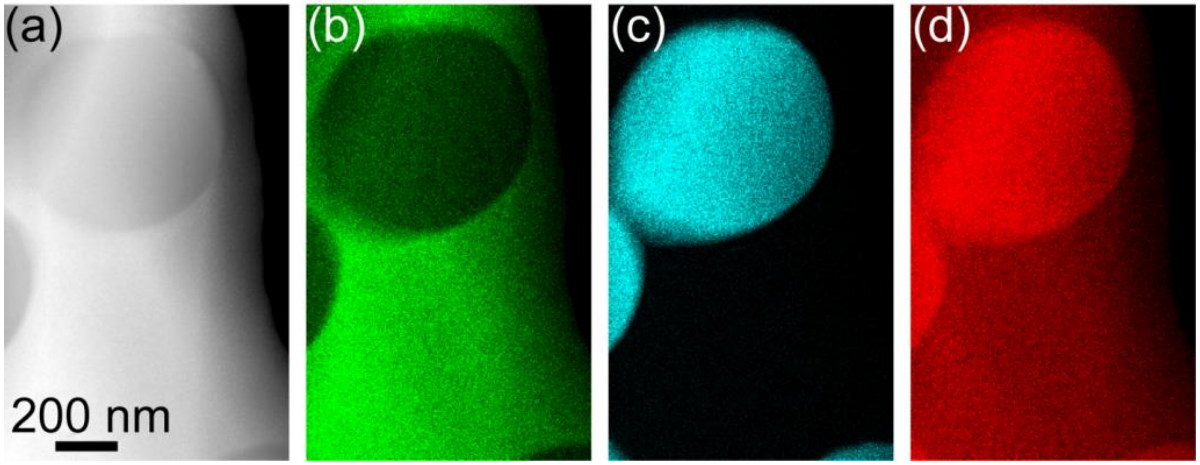

Figure 2.17 *(a) HAADF image of ZnO matrix with nano $ZnCr_2O_4$ inclusion. EDX maps of (b) Zn, (c) Cr and (d) O.* [unpublished, Wei Zhan]

EDX is suitable for the characterization of elemental and chemical properties. In comparison, EELS provides higher spatial resolution and better analytical sensitivity. Taking use of EELS, both the spatial resolving ability at the atomic scale and detection sensitivity at single-atom level are more easily achievable than EDX. Moreover, EELS can be employed to analyze band gap (if there is one), free electron density, dielectric response, specimen thickness, bonding/valence state and the nearest-neighbor atomic structure. In addition, the fluorescence-yield limitation that restricts EDX analysis of light elements does not influence EELS, thus EELS has a much higher efficiency.

2.4 Cathodoluminescence and X-ray photoelectron spectroscopy

In this work, for the sake of verifying the absolute ZnO band gap values measured by probe-corrected and monochromated STEM-EELS, CL analyses [48, 100, 101] were conducted in a

Hitatchi SU5000 with a DELMIC SPARC detector. To guarantee that the electrons have adequate energy to penetrate through the $Zn_{1-x}Cd_xO$ layer, and into the ZnO layer, an electron beam as high as 7 kV could be used.

XPS utilizes ejected electron, whose quantity and kinetic energy can be used to determine the binding energy. XPS is element-specific, allows chemical analysis, and can be employed to measure the VBM, giving beneficial information with respect to the band structure. XPS studies were undertaken in a KRATOS AXIS ULTRADLD instrument, and monochromatic Al Ka radiation at 15 kV and 15mA was used. High-resolution XPS spectra were acquired with pass energy of 20 eV and dwell time of 200 ms. In order to efficiently limit sources of error, such as sample charging, XPS signals were collected with Al contacts applied by electron beam. CasaXPS was adopted to process the XPS data [Available website: http://www.casaXPS.com].

2.5 Geometric phase analysis

It has been shown that probe-corrected atomic-resolution HAADF imaging together with GPA is capable of analyzing the strain fields at dislocations with a high level of precision [66, 67]. The methodology relies on fast Fourier transforms (FFT) and real-space peak detection is not required, excluding the problem aroused by slight misorientation at two neighboring regions. In addition, there is no need to assign appropriate sublattices, which is of great benefit for stain analysis of atom-resolved images. In this study, the measurement of local atomic displacements was undertaken using the GPA script [102-104] implemented in DigitalMicrograph. An undistorted flat region was used as internal reference lattice. Non-collinear reflections in the Fourier transform of the HAADF image were chosen by small digital apertures, and strain maps with respect to strong reflections were obtained directly through extraction of the local phase.

For analysis of large-scale strain, HRTEM imaging is sensitive to specimen variations, such as thickness and defocus value, and often suffers from the contrast reversal effects, resulting in the complication of the image interpretation [74]. In comparison, HAADF is of great use for determining large-area strain accurately on the unit-cell scale [105]. Because HAADF imaging offers uniform contrast, which is less dependent on experimental conditions and easily interpretable. Small variation of sample thickness and defocus do not introduce the problem of contrast reversal [73, 106, 107]. Additionally, the strong intensity of the

aberration-corrected electron probe with strong intensity can penetrate thick foil, where an atom-resolved HAADF image can be taken [108].

A representative ZnO dislocation structure together with GPA strain maps is illustrated in Figure 2.18. The high-resolution STEM images in Figure 2.18(a)-(b) show the existence of a dislocation in bulk ZnO. The inset at the upper right of HAADF image displays the projected atomic model of the red box at the middle. The green and red balls represent Zn and O, respectively. A dislocation is clearly observed in Fourier filtered images of the (0002) and $(10\bar{1}1)$ planes, as displayed in Figure 2.18(d)-(e). The strain field caused by this defect is quantitatively mapped by GPA (Figure 2.18(f)-(g)).

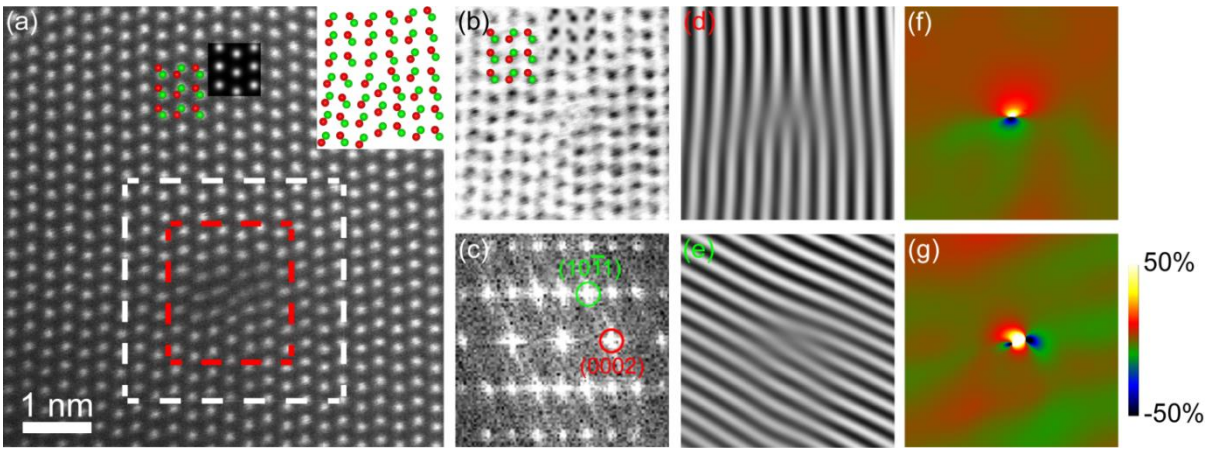

Figure 2.18 *(a) HAADF and (b) ABF images of ZnO viewed from the [1-210] direction. The white dotted square, which is the same region as ABF imaging in (b), indicates the area used for GPA strain analysis. The insets show the projected atomic model and simulated image. (c) FFT of the white square in the HAADF image. The red and green circles display the two lattice fringes. Fourier filtered images of the (d) (0002) and (e) (10-11) lattice fringes. GPA (f)* ε_{xx} *and (g)* ε_{yy} *maps.* [unpublished, Wei Zhan]

In addition, we observed $ZnCr_2O_4$ grain boundary in the $[1\bar{1}0]$ zone axis. The corresponding high-resolution HAADF image and GPA strain maps are displayed in Figure 2.19. The image size here is approximately 15.4 nm × 15.4 nm. Note that in the FFT of Figure 2.19(a), $(\bar{1}\bar{1}3)_u$ and $(222)_u$ represent the reflections of the upper grain, while $(\bar{1}\bar{1}3)_b$ and $(222)_b$ indicate the reflections of the bottom grain. Some dislocations are observed at the boundary of the upper and bottom grains, as illustrated by Fourier filtered image of both $(\bar{1}\bar{1}3)_{upper}/(222)_{bottom}$ and $(222)_{upper}/(\bar{1}\bar{1}3)_{bottom}$ lattice fringes in Figure 2.19(b). Although the angle discrepancy between the $(\bar{1}\bar{1}3)_{upper}/(222)_{bottom}$ or $(222)_{upper}/(\bar{1}\bar{1}3)_{bottom}$ planes is negligible, the d-spacings

of $(\bar{1}\bar{1}3)$ and (222) planes are 2.4 Å and 2.51 Å, respectively. Thus, at the grain boundary, a big lattice mismatch between the upper and bottom $ZnCr_2O_4$ exists, resulting in many dislocations as shown in Figure 2.19(b). Besides the dislocations B1~B3 at the grain boundary, we found additional dislocations B4~B6, as verified in the GPA ε_{yy} map in Figure 2.19(d). Using the Bragg reflections of (222) and $(\bar{1}\bar{1}3)$, GPA was put into application here to elucidate the atomic displacements, and a flat region from bulk $ZnCr_2O_4$ at the bottom was chosen as internal reference. The overall lattice displacement far away from the grain boundary is negligible, and can be taken as nearly zero. However, at the grain boundary, large strains can be seen, due to lattice mismatches as compared with the bulk. The distortion is observed across the interface, as revealed by dislocations between the $(\bar{1}\bar{1}3)_{upper}/(222)_{bottom}$ or $(222)_{upper}/(\bar{1}\bar{1}3)_{bottom}$ planes. For dislocations associated with the $(\bar{1}\bar{1}3)_{upper}/(222)_{bottom}$ planes, both the ε_{xx} and ε_{yy} components of the strain tensor exhibit inhomogeneous features. The strain along the *xx* direction is obviously localized at the interfacial dislocations. While along the *yy* direction, the strain field exhibits a much weaker component. In comparison, the $(222)_{upper}/(\bar{1}\bar{1}3)_{bottom}$ dislocations only display a very strong ε_{yy} component, while a relative flatness is found for the ε_{xx} component. All these stains are relaxed by producing a high density of dislocations. The outcome shown in Figure 2.18 and Figure 2.19 has led us to a conclusion that high-resolution STEM images coupled with GPA enable accurate strain measurements. Moreover, as illustrated in existing publications, STEM imaging with achievable spatial resolution at atomic-level [109] can be utilized to determine unit cell parameter. In addition, it is previously mentioned that strain affects both band gap [64] and plasmon energy [94]. Therefore, for this sample ($ZnCr_2O_4$ nano-inclusions embedded in ZnO matrix) with special regard to the interface area, the relevancy among unit cell parameter, strain, band gap and plasmon energy could be studied in the future, similar to the suggested possible research on $Zn_{1-x}Cd_xO$/ZnO heterostructure (see Chapter 2.2.5).

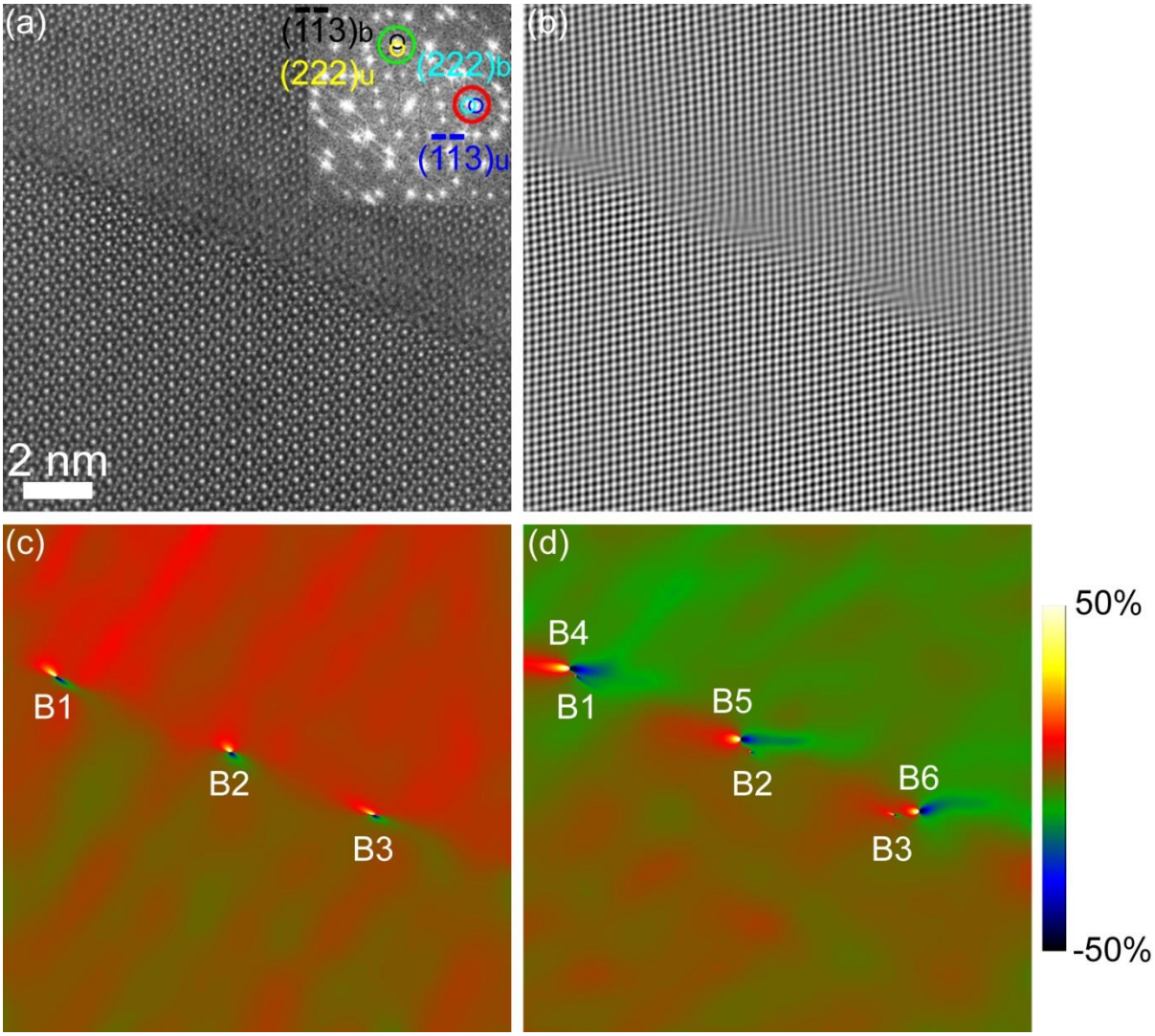

Figure 2.19 *(a) HAADF image of $ZnCr_2O_4$ grain boundary acquired from the [1-10] orientation. The inset at the upper right of the HAADF image displays its FFT, and the circles show the lattice fringes. (b) Fourier filtered image of both $(-1-13)_{upper}/(222)_{bottom}$ and $(222)_{upper}/(-1-13)_{bottom}$ lattice fringes. GPA (c) ε_{xx} and (d) ε_{yy} maps.* [unpublished, Wei Zhan]

2.6 Sample fabrication

Four thin film samples of $Zn_{1-x}Cd_xO$ with nominal Cd concentrations of x=0.05, 0.09, 0.13, and 0.16 (hereafter $Cd_{0.05}$, $Cd_{0.09}$, $Cd_{0.13}$, $Cd_{0.16}$) were synthesized using metal organic vapour phase epitaxy (MOVPE) along the [0001] axis of α-Al_2O_3 substrates buffered with a pure ZnO film. The growth temperature of the samples was held at 370 ℃. Before loaded into the chamber, the substrates were cleaned in several solutions, rinsed by deionized water, and then dried with N_2 gas. Diethyl zinc (DEZn), dimethyl cadmium (DMCd), and tertiary butanol (*t*-BuOH) were used as zinc source, cadmium source, and oxidizing agent, respectively.

Reacting the elements with radicals formed these gaseous precursors, which travelled to the α-Al_2O_3 substrate together with a stream of hydrogen. For DEZn and *t*-BuOH, the flows were set up at 100 and 150 sccm, respectively. The temperatures of both DEZn and DMCd bubblers were maintained at 10 ℃, while that of *t*-BuOH was kept at 30 ℃. The Cd content in the films was varied by changing the DMCd flow rate while maintaining the growth temperature. A radiofrequency coil heated the substrate area, where the gaseous precursors reacted and deposited the material.

STEM-EDX maps of the $Cd_{0.16}$ sample are displayed in Figure 2.20 to confirm the structure of the $Zn_{1-x}Cd_xO/ZnO/α\text{-}Al_2O_3$ thin films synthesized above. It can be seen from the elemental maps obtained for Zn and Cd (Figure 2.20(b)-(c)) that, all four samples exhibit the two-layer structure, with an inner buffer layer consisting of pure ZnO, and an outer layer of Cd-containing ZnO. The thickness of each layer is approximately 115−135 nm. Elemental EDX map of Al in Figure 2.20(e) verifies that the α-Al_2O_3 substrate is situated at the bottom. For the HAADF image, the heavier Cd atoms scatter more strongly to high angles than the lighter Zn atoms, thereby giving the enhanced contrast seen from the Cd-containing layer in Figure 2.20(a). At the $Zn_{1-x}Cd_xO$ layer of the Cd elemental map (Figure 2.20(b)), dense (sparse) green pixels represent high (low) Cd content. There are indications that some of the tendrils observed in the HAADF images are associated with a higher concentration of Cd. No significant variations in oxygen distribution were found, see Figure 2.20(d).

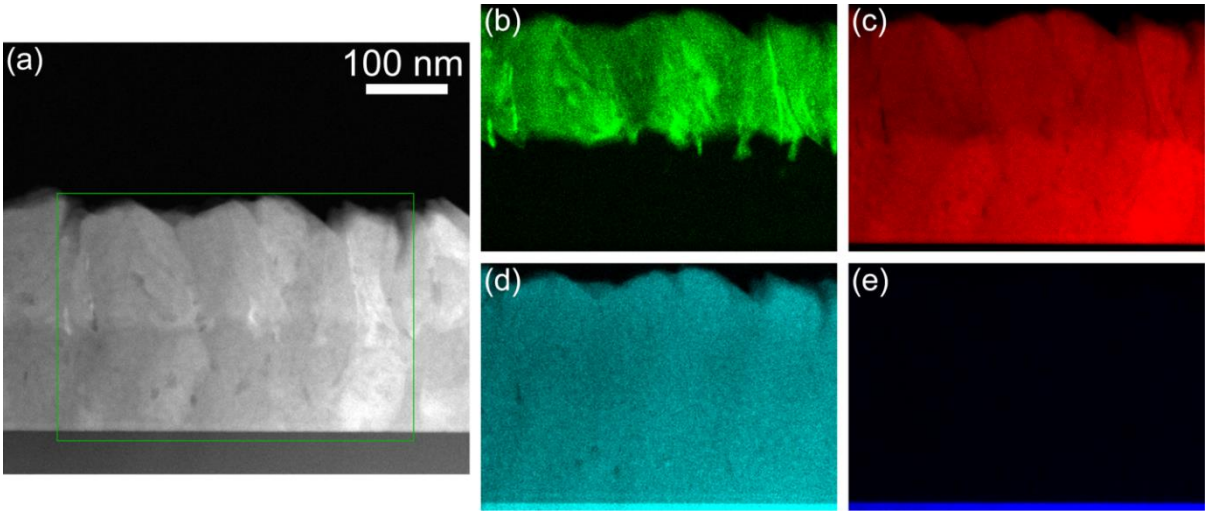

Figure 2.20 *(a) HAADF image of $Zn_{1-x}Cd_xO/ZnO/α\text{-}Al_2O_3$ with the green box indicating the area used for EDX map. EDX maps of (b) Cd, (c) Zn, (d) O and (e) Al.* [Paper I]

The Cr_2O_3-alloyed ZnO with $ZnCr_2O_4$ nano-inclusion specimen was prepared by mixing powders of ZnO and α-Cr_2O_3. The molar ratio ZnO:α-Cr_2O_3 is 15:1. The mixtures were ball-

milled for 3 h, and then uniaxially dry pressed into pellets at a pressure of 2805 MPa, before being sintered at 1350℃ for 24 h, with temperature change rate of 450 ℃/h. To guarantee the purity of the synthesized ZnO matrix and embedded $ZnCr_2O_4$ nanoparticles, any laboratory vessel (such as glassware) that contacted with the powders of ZnO and α-Cr_2O_3, as well as the mixture and pellet, was completely cleaned beforehand utilizing acetone, ethanol, and deionized water for two times in sequence.

2.7 TEM specimen preparation and experimental setup

The samples for TEM investigation were prepared by cutting the slices into small pieces. These slices were thereafter mechanically ground to 150 μm, after which the slices were made into wedges with a tilt angle of 2.5º using MultiPrep System (Allied High Tech Products, Rancho Dominguez, CA, USA). One side of the slices was further ground and polished down to 20 μm. Then the ground sides were finally thinned by the low angle ion milling & polishing system (Fischione 1010) with an incident beam angle of 8º, gun voltages of 5 kV/3 kV/0.5 kV, and gun currents of 5 mA/4 mA/3 mA. This resulted in specimens approximately 30 nm thick. The samples were plasma cleaned using a Fischione Model 1020 plasma cleaner directly before the TEM/STEM/EELS/EDX experiments were performed.

Note that for the $Zn_{1-x}Cd_xO$/ZnO/α-Al_2O_3 specimens, before TEM/STEM observation or EELS/EDX spectrum mapping, the α-Al_2O_3 substrate was tilted to the $[2\bar{1}\bar{1}0]$ orientation, so as to make the electron beam parallel to substrate/film interface and perpendicular to the film growth direction, the [0001] axis of the substrate. Figure 2.21 illustrates HRTEM image of α-Al_2O_3 viewed from the $[2\bar{1}\bar{1}0]$ direction. Diffraction patterns at the upper left were taken from this image area and verify this zone axis. The upper right shows the simulated image based on the atomic projection model at the bottom right. The experimental and simulated images, as well as the model, are consistent with each other.

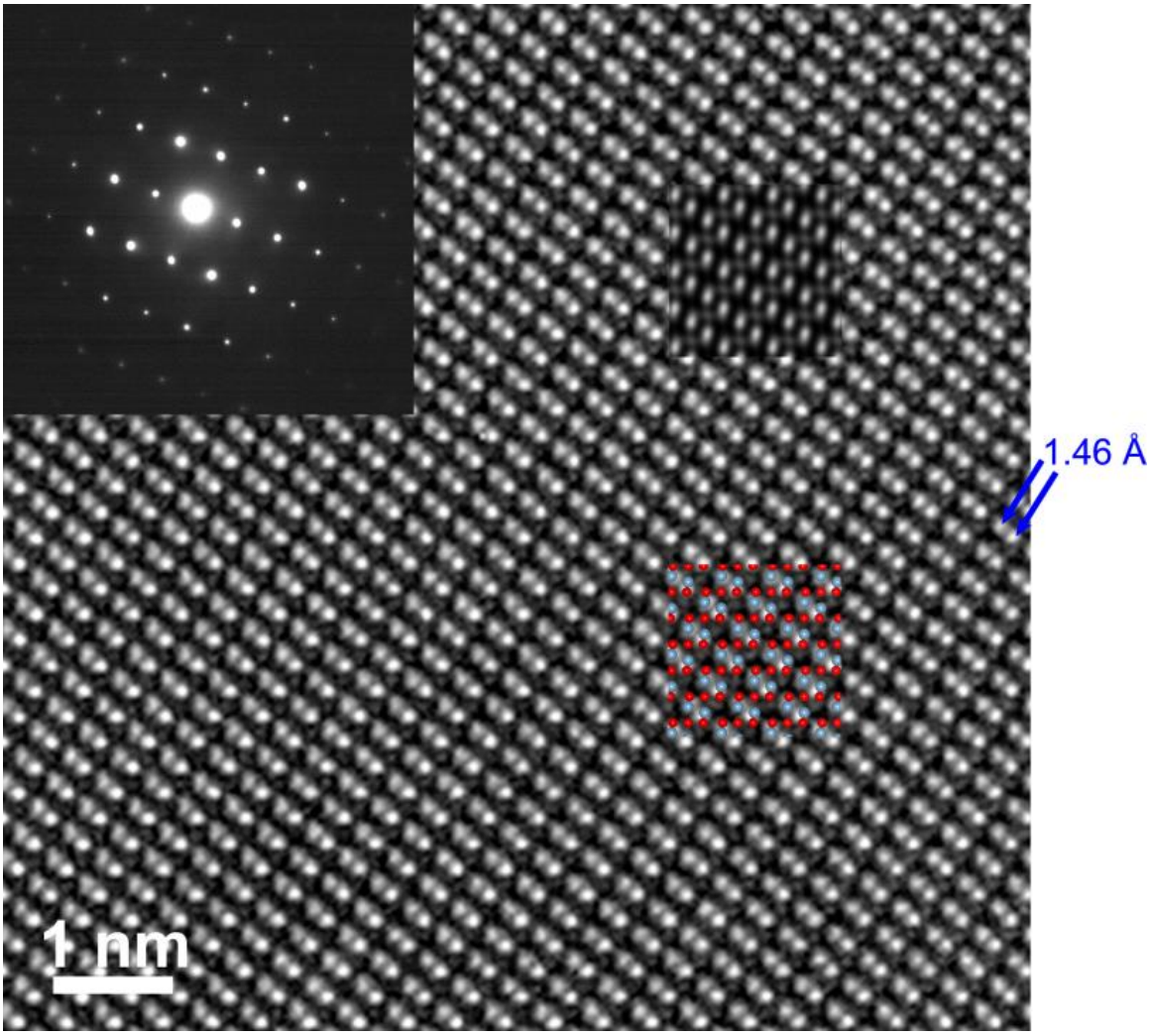

Figure 2.21 *HRTEM image of α-Al_2O_3 observed from the [2-1-10] direction. The light blue and red balls represent Al and O atoms, respectively.* [unpublished, Wei Zhan]

The TEM/STEM/EELS/EDX studies were carried out in a probe-corrected and monochromated FEI Titan G2 60−300, with a Fischione HAADF detector (3000), a Gatan GIF Quantum 965 EELS spectrometer, and four FEI Super-X EDX detectors. The chemical mapping and structural studies were performed at a 300 kV accelerating voltage, with achievable spatial resolutions of approximately 0.8 Å and 2 Å for probe-corrected STEM and TEM imaging, respectively. For simultaneous HAADF and ABF observations, the probe convergence angle (α) was all approximately 22 mrad, while the STEM collection angles were 98.7−200 mrad and 10.6−21.5 mrad, respectively. The core-loss edges were analyzed utilizing normal EELS, whose spectral resolution is about 0.8 eV.

The monochromated EELS experiments were employed to measure optical band gaps. They were performed at a low accelerating voltage of 60 kV for the purpose of reducing the effect of the Cherenkov radiation. At this high tension, a spatial resolution better than 1.4 Å can be

achieved for probe-corrected STEM imaging. The energy resolution of monochromatic electrons was approximately 0.15 eV, as determined by the FWHM of the ZLP. The probe convergence angle (α) was all approximately 23 mrad. For band gap mapping, spectrometer dispersion was set up at 0.01 eV/channel, and the EELS spectrometer collection angle was 16.8, 21.1 and 26.6 mrad. While for mapping of both band gap and plasmon energy, spectrometer dispersion of 0.025 eV/channel was chosen, so that EELS spectrum range would cover both band gap and plasmon energy. The EELS spectrometer collection angle was all about 26.6 mrad so as to ensure sufficient EELS signals that enter into the GIF spectrometer. The EELS signals were collected in the form of spectrum images. In this way the band gap and plasmon energy can be mapped two-dimensionally. The procedure of extracting band gap is the same as the previously published work [29, 63, 85]. It must be stressed that both high spatial and spectral resolution in EELS characterization does not necessarily ensure a good quality band gap mapping, as a result of significant drop in beam intensity caused by the monochromator. To deal with this kind of issue, in addition to appropriate exposure time close to the CCD limitation, the acquisition time of each monochromatic EELS mapping was around 90 min. We obtained the values of plasmon energies in EELS spectrum using a Gaussian function as fitted in DigitalMicrograph. For both band gap and plasmon energy mapping, pixels were binned in order to handle the problem associated with noise and improve the mapping quality. To compare the band gaps and plasmon energies from pixel to pixel conveniently, the binning of the two were kept the same.

For STEM imaging or spectrum mapping, the probe was aberration corrected ahead of time, where a convergence angle (α) about 22 mrad and a camera length of 77 mm were chosen. The images or maps were taken until the requirements were met, with sufficient details described in Chapter 2.1.3. This guarantees the high spatial resolving ability, and representative atom-resolution STEM images can be found in Figure 2.5 and 2.6. To achieve a good energy resolution for (monochromated) EELS measurements, GIF spectrometer was tuned in TEM mode, before which TEM alignment was performed to ensure a parallel uniform beam with minimum astigmatism. This also benefits the following STEM-EELS spectrum mapping. A typical HRTEM image after fine alignment is displayed in Figure 2.21. To improve EELS spectral resolution, before acquiring a spectrum or filtered image, the spectrometer was focused and aligned until a minimum width and maximum height of ZLP was achieved. During the EELS or EDX mapping, the spatial drift was corrected.

Chapter 3

Overview of publications

3.1 Paper I

Nanoscale mapping of optical band gaps using monochromated electron energy loss spectroscopy

W. Zhan, C. S. Granerød, V. Venkatachalapathy, K. M. H. Johansen, I. J. T. Jensen, A. Y. Kuznetsov and Ø. Prytz

As nanoscale semiconductor engineering makes advances, measurement of band structure at the corresponding dimension becomes an issue of critical importance. Monochromated EELS and probe-corrected STEM can be applied to this field with both high spatial and energy resolution, in contrast to conventional techniques that suffer from an acute lack of spatial resolving power. Lin Gu and co-authors [57] developed a particular instrumental design of energy-filtered STEM to make band gap mapping possible, and predicted an spatial resolution around 12 nm, which is considerably above theoretical estimation. This paper made use of probe-corrected and monochromated STEM-EELS to measure the band gap energies of $Zn_{1-x}Cd_xO/ZnO$ with a high level of precision, and discussed the achievable spatial resolving power with the support of elemental EDX analysis which enabled accurate quantification. Even with this conventional setup of the microscope, two-dimensional mapping of optical band gaps reached spatial resolution well below 10 nm, which is very close to the theoretical limit. In addition, the correlations between composition and band gap properties were clarified.

W. Zhan prepared the TEM samples, carried out TEM/probe-corrected STEM/(monochromated) EELS/EDX experiments, performed the band gap mapping, and did the data analysis. C. S. Granerød developed the computing method for extracting band gap maps and did the fit to the simulated profile. V. Venkatachalapathy synthesized the thin films. K. M. H. Johansen and I. J. T. Jensen conducted CL measurements and analysis.

3.2 Paper II

Band gap maps beyond the delocalization limit: correlation between optical band gaps and plasmon energies at the nanoscale

W. Zhan, V. Venkatachalapathy, T. Aarholt, A. Y. Kuznetsov and Ø. Prytz

Two-dimensional STEM-EELS observation of band gaps can be achieved on the nanometer scale. However, there are very few examples in the literature due to the associated experimental and analytical complexities. In this work, we used monochromated EELS combined with probe-corrected STEM to simultaneously map the band gaps and plasmon energies in $Zn_{1-x}Cd_xO/ZnO$. These properties are both associated with the unit cell parameter, and are therefore correlated with each other. We established a quantitative correlation between the band gap and plasmon energy, and applied this newly-proposed approach to the directly measured plasmon energy map, thereby retrieving a reconstructed band gap map with better spatial resolution. Thus these findings provide an easy and straightforward approach to perform band gap mapping via measurements of the plamon energy, while side-stepping the inelastic delocalization limitation and thus improving the spatial resolution. Other alloyed semiconductor systems with band gap modulation, such as $Zn_{1-y}Mg_yO$, would benefit from this study immediately.

W. Zhan prepared the TEM samples, carried out TEM/probe-corrected STEM/(monochromated) EELS/EDX experiments, performed the band gap and plasmon energy mapping, and did the data analysis. V. Venkatachalapathy synthesized the thin films. T. Aarholt wrote the code.

3.3 Paper III

Nano $ZnCr_2O_4$ inclusions in ZnO matrix investigated by probe-corrected STEM-EELS

W. Zhan, A. Y. Kosinskiy, L. Vines, K. M. H. Johansen, P. A. Carvalho and Ø. Prytz

The defect structure and its associated strain at interfaces are of critical importance for the material or device functionality. With the availability of probe forming correctors, an electron beam with sub-ångström size can be realized, which enables us to carry out atom-resolved imaging as well as fast spectroscopic mapping of high quality. We applied GPA to high-

resolution images of $ZnO/ZnCr_2O_4$ interfaces, and obvious strain fields at the defective structures were found and analyzed. Furthermore, two-dimensional band gap measurements of $ZnCr_2O_4$ nanoparticles were achieved by making use of monochromatic electrons in conjunction with probe-corrected STEM. The defect structures and strains at interfaces reported here would probably lead to a better understanding of thin film growth.

W. Zhan synthesized the specimen, prepared the TEM samples, carried out TEM/probe-corrected STEM/(monochromated) EELS/EDX experiments, performed band gap mapping and STEM image simulation, and did GPA and other data analysis. A. Y. Kosinskiy conducted XRD measurements. L. Vines and K. M. H. Johansen contributed to the improvement of the manuscript. P. A. Carvalho helped GPA analysis.

3.4 Paper IV

Automated approaches for band gap mapping in STEM-EELS

C. S. Granerød, W. Zhan, Ø. Prytz

Although point- and line measurements of band gaps using EELS have been the subject of many publications in the past, very few studies have been focused on two-dimensional mapping of band structure. The main reason for this is the level of experimental and data analysis complexities, as well as the lack of efficient ways for computing band gap mapping (semi-) automatically. In this work we explored an efficient method to extract band gaps (semi-) automatically from high resolution spectrum images of $Zn_{1-x}Cd_xO/ZnO$ hetero structures. The various experimental and data processing challenges were discussed, and the proposed method is demonstrated with great accuracy and precision on large data sets.

C. S. Granerød developed the computing method for mapping band gap, and carried out the data analysis. W. Zhan prepared the TEM sample, and performed probe-corrected STEM/(monochromated) EELS experiments.

3.5 Paper V

Bandgap and band edge positions in compositionally graded ZnCdO

I. J. T. Jensen, K. M. H. Johansen, W. Zhan, V. Venkatachalapathy, L. Brillson, A. Y. Kuznetsov and Ø. Prytz

ZnO can be alloyed with Cd, allowing the band gap to be tuned in the visible range. For a long time, however, there has been an unresolved debate on whether this band gap change is caused by the valence band, conduction band, or both. In this paper, the band structures of four ZnCdO films were investigated by XPS and CL, and it was found that a shift of CBM is the main cause of the band gap reduction upon alloying with Cd, while there is no significant change in VBM. These findings provide new insight on the band gap tunability in ZnCdO alloys, and would lead to a better understanding of band structure engineering mechanism.

I. J. T. Jensen conducted the XPS measurements and did the data analysis. K. M. H. Johansen carried out CL investigations. W. Zhan prepared the four TEM samples, performed probe-corrected STEM/EDX experiments, and did the EDX quantification analysis. V. Venkatachalapathy synthesized the thin films.

Chapter 4

Summary and suggestions for future work

In the current project, a series of ZnO thin film samples alloyed with a varying amount of Cd and nano $ZnCr_2O_4$ inclusions embedded in ZnO matrix were studied by taking advantages of state-of-the-art probe-corrected and monochromated STEM-EELS. We conducted detailed two-dimensional band structural and compositional measurements of $Zn_{1-x}Cd_xO$/ZnO down to the nanometer scale and with excellent precision. Our results demonstrate that with today's instrumentation a spatial resolution close to theoretical limit can be achieved by utilizing monochromatic electrons, making it a promising method for band gap analysis at the nanoscale. This together with the high spatial-resolution analysis of structure and strain of the Cr_2O_3-alloyed ZnO sample should see a wide-spread application for investigating band gap and structure of nanoscale semiconductors in the future.

For example, graded $Ga_{1-z}Al_zN$ *p–n* junctions can be realized through polarization-induced doping, resulting in graded band gaps and high electrical conductivity [35]. Such gradient alloyed semiconductors are of great benefit for energy savings in optoelectronic devices. The combination of probe-corrected STEM, monochromated EELS and EDX gives two-dimensional structure, composition and electronic property (e.g. band gap) information with high spatial and spectral resolving ability. Thus, two-dimensional mapping and accurate observation of the band gap and compositional variations, as achieved in the present work, could assist in the further development of new types of graded semiconductor *p–n* junctions.

By means of high spatial and spectral resolution monochromated EELS in combination with probe-corrected STEM, research similar to those mentioned above can be accomplished in quantum wells with thickness on the nanometer scale. This would help fabricate more efficient LEDs.

Besides, in existing publications, two dimensional electron gas was found to exist within a narrow width of approximately 10 nm at interfaces such as $SrTiO_3/LaAlO_3$, resulting in superconductivity [110, 111]. The STEM-EELS approach can be applied here, and direct mapping of band gap at this kind of interface can be performed. Compared to the recent report [112] that used depth-resolved CL to investigate the $SrTiO_3/LaAlO_3/SrTiO_3$

heterostructure layer by layer, the STEM-EELS method provides profile imaging, where the structure and band gap of interfacial layer and layers nearby can be observed simultaneously. Indeed, the monochromatic electrons can not detect excitations in the range close to zero because a tail exists in the ZLP. However, a drop of band gap at such interfaces should be expected.

Furthermore, nowadays one-dimensional EELS band gap investigation is undergoing a large number of investigations. However, there are very few reports about two-dimensional band gap mapping because of the experimental and data processing complexity in EELS band gap analysis. Using the STEM-EELS technique, the present study proposed a robust quantitative E_p-E_g correlation in $Zn_{1-x}Cd_xO$/ZnO hetero structure through the simultaneous collection of band gap and plasmon energy signals, offering a convenient and straightforward approach to create band gap maps with better spatial resolution than achievable in conventional EELS measurements. This method most likely provides a novel and realizable solution for band gap determination of other alloyed semiconductors, such as $Zn_{1-y}Mg_yO$, $Ga_{1-y}Al_yN$, and $Ga_{1-y}In_yN$.

In addition, low-loss and core-loss EELS signals can be collected simultaneously using the dual-EELS setup in the FEI Titan 60-300 microscope. This leads us to think about further research that correlates band gap, plasmon energy and O-*K* edge in the $Zn_{1-x}Cd_xO$/ZnO sample. It is known that the EELS O-*K* edge probes the unoccupied O 2*p* states, thus the shift of O-*K* edge can be used to determine the change of CBM. In combination with band gap variations, the VBM position can be obtained.

Last but not the least, atom-resolved STEM can be employed to observe crystal structure and measure unit cell parameter [109], which is the determining factor for both band gap and plasmon energy in $Zn_{1-x}Cd_xO$/ZnO. This measured unit cell parameter can be verified by XRD [113], and would help deepen our understanding of the correlation between unit cell parameter and band gap or plasmon energy. Note that in this work, $Zn_{1-x}Cd_xO$ is inhomogeneous with large variations of Cd content, and there are many grains with different orientations. Therefore we found it very difficult to perform high-resolution STEM imaging of this film due to large variations in zone axis. To obtain a homogeneous film with a specific orientation and thus enable atomic-resolution STEM imaging, it is advised that $Zn_{1-x}Cd_xO$ is directly grown on ZnO substrate (instead of using α-Al_2O_3 substrate with a ZnO buffer layer in between), before which the surface of ZnO substrate is finely polished.

References

[1] D.C. Look, Recent advances in ZnO materials and devices, Materials Science and Engineering: B, 80 (2001) 383-387.
[2] Ü. Özgür, Y.I. Alivov, C. Liu, A. Teke, M.A. Reshchikov, S. Doğan, V. Avrutin, S.-J. Cho, H. Morkoç, A comprehensive review of ZnO materials and devices, Journal of Applied Physics, 98 (2005) -.
[3] D.C. Reynolds, D.C. Look, B. Jogai, Optically pumped ultraviolet lasing from ZnO, Solid State Communications, 99 (1996) 873-875.
[4] D.M. Bagnall, Y.F. Chen, Z. Zhu, T. Yao, S. Koyama, M.Y. Shen, T. Goto, Optically pumped lasing of ZnO at room temperature, Applied Physics Letters, 70 (1997) 2230-2232.
[5] Z.L. Wang, Splendid One-Dimensional Nanostructures of Zinc Oxide: A New Nanomaterial Family for Nanotechnology, ACS Nano, 2 (2008) 1987-1992.
[6] M. Chaari, A. Matoussi, Electrical conduction and dielectric studies of ZnO pellets, Physica B: Condensed Matter, 407 (2012) 3441-3447.
[7] M.S. Arnold, P. Avouris, Z.W. Pan, Z.L. Wang, Field-Effect Transistors Based on Single Semiconducting Oxide Nanobelts, The Journal of Physical Chemistry B, 107 (2003) 659-663.
[8] W. Water, S.-E. Chen, T.-H. Meen, L.-W. Ji, ZnO thin film with nanorod arrays applied to fluid sensor, Ultrasonics, 52 (2012) 747-752.
[9] A.C. Chaves, S.J.G. Lima, R.C.M.U. Araújo, M.A.M.A. Maurera, E. Longo, P.S. Pizani, L.G.P. Simões, L.E.B. Soledade, A.G. Souza, I.M.G.d. Santos, Photoluminescence in disordered Zn_2TiO_4, Journal of Solid State Chemistry, 179 (2006) 985-992.
[10] U. Chellam, Z.P. Xu, H.C. Zeng, Low-Temperature Synthesis of $Mg_xCo_{1-x}Co_2O_4$ Spinel Catalysts for N_2O Decomposition, Chemistry of Materials, 12 (2000) 650-658.
[11] D.-C. Kim, S.-K. Ihm, Application of Spinel-Type Cobalt Chromite as a Novel Catalyst for Combustion of Chlorinated Organic Pollutants, Environmental Science & Technology, 35 (2001) 222-226.
[12] X. Lou, S. Liu, D. Shi, W. Chu, Ethanol-sensing characteristics of $CdFe_2O_4$ sensor prepared by sol–gel method, Materials Chemistry and Physics, 105 (2007) 67-70.
[13] K. Ahn, B.W. Wessels, S. Sampath, Spinel humidity sensors prepared by thermal spray direct writing, Sensors and Actuators B: Chemical, 107 (2005) 342-346.
[14] S. Bid, S.K. Pradhan, Preparation of zinc ferrite by high-energy ball-milling and microstructure characterization by Rietveld's analysis, Materials Chemistry and Physics, 82 (2003) 27-37.
[15] P. Lavela, J.L. Tirado, C. Vidal-Abarca, Sol–gel preparation of cobalt manganese mixed oxides for their use as electrode materials in lithium cells, Electrochimica Acta, 52 (2007) 7986-7995.
[16] R.M. Gabr, M.M. Girgis, A.M. El-Awad, Formation, conductivity and activity of zinc chromite catalyst, Materials Chemistry and Physics, 30 (1992) 169-177.
[17] M. Bayhan, T. Hashemi, A.W. Brinkman, Sintering and humidity-sensitive behaviour of the $ZnCr_2O_4$–$K_{22}CrO_4$ ceramic system, Journal of Materials Science, 32 (1997) 6619-6623.
[18] P. Parhi, V. Manivannan, Microwave metathetic approach for the synthesis and characterization of $ZnCr_2O_4$, Journal of the European Ceramic Society, 28 (2008) 1665-1670.
[19] L. Schmidt-Mende, J.L. MacManus-Driscoll, ZnO – nanostructures, defects, and devices, Materials Today, 10 (2007) 40-48.
[20] A. Ohtomo, M. Kawasaki, T. Koida, K. Masubuchi, H. Koinuma, Y. Sakurai, Y. Yoshida, T. Yasuda, Y. Segawa, $Mg_xZn_{1-x}O$ as a II–VI widegap semiconductor alloy, Applied Physics Letters, 72 (1998) 2466-2468.
[21] A. Ohtomo, K. Tamura, M. Kawasaki, T. Makino, Y. Segawa, Z.K. Tang, G.K.L. Wong, Y. Matsumoto, H. Koinuma, Room-temperature stimulated emission of excitons in ZnO/(Mg,Zn)O superlattices, Applied Physics Letters, 77 (2000) 2204-2206.

[22] T. Makino, Y. Segawa, M. Kawasaki, A. Ohtomo, R. Shiroki, K. Tamura, T. Yasuda, H. Koinuma, Band gap engineering based on $Mg_xZn_{1-x}O$ and $Cd_yZn_{1-y}O$ ternary alloy films, Applied Physics Letters, 78 (2001) 1237-1239.
[23] T. Gruber, C. Kirchner, R. Kling, F. Reuss, A. Waag, ZnMgO epilayers and ZnO–ZnMgO quantum wells for optoelectronic applications in the blue and UV spectral region, Applied Physics Letters, 84 (2004) 5359-5361.
[24] T. Gruber, C. Kirchner, R. Kling, F. Reuss, A. Waag, F. Bertram, D. Forster, J. Christen, M. Schreck, Optical and structural analysis of ZnCdO layers grown by metalorganic vapor-phase epitaxy, Applied Physics Letters, 83 (2003) 3290-3292.
[25] D.M. Detert, S.H.M. Lim, K. Tom, A.V. Luce, A. Anders, O.D. Dubon, K.M. Yu, W. Walukiewicz, Crystal structure and properties of $Cd_xZn_{1-x}O$ alloys across the full composition range, Applied Physics Letters, 102 (2013) -.
[26] X.J. Wang, I.A. Buyanova, W.M. Chen, M. Izadifard, S. Rawal, D.P. Norton, S.J. Pearton, A. Osinsky, J.W. Dong, A. Dabiran, Band gap properties of $Zn_{1-x}Cd_xO$ alloys grown by molecular-beam epitaxy, Applied Physics Letters, 89 (2006) 151909-151909-151903.
[27] V. Venkatachalapathy, A. Galeckas, M. Trunk, T. Zhang, A. Azarov, A.Y. Kuznetsov, Understanding phase separation in ZnCdO by a combination of structural and optical analysis, Physical Review B, 83 (2011) 125315.
[28] G. Manoranjan, A.K. Raychaudhuri, Structure and optical properties of Cd-substituted ZnO ($Zn_{1-x}Cd_xO$) nanostructures synthesized by the high-pressure solution route, Nanotechnology, 18 (2007) 115618.
[29] W. Zhan, C.S. Granerød, V. Venkatachalapathy, K.M.H. Johansen, I.J.T. Jensen, A.Y. Kuznetsov, P. Ø, Nanoscale mapping of optical band gaps using monochromated electron energy loss spectroscopy, Nanotechnology, 28 (2017) 105703.
[30] M. Bosman, L.J. Tang, J.D. Ye, S.T. Tan, Y. Zhang, V.J. Keast, Nanoscale band gap spectroscopy on ZnO and GaN-based compounds with a monochromated electron microscope, Applied Physics Letters, 95 (2009) 101110-101110-101113.
[31] H. Hung-Chun Lai, V.L. Kuznetsov, R.G. Egdell, P.P. Edwards, Electronic structure of ternary $Cd_xZn_{1-x}O$ ($0 \le x \le 0.075$) alloys, Applied Physics Letters, 100 (2012) 072106.
[32] A. Tsukazaki, A. Ohtomo, T. Kita, Y. Ohno, H. Ohno, M. Kawasaki, Quantum Hall Effect in Polar Oxide Heterostructures, Science, 315 (2007) 1388.
[33] H. Tampo, H. Shibata, K. Maejima, A. Yamada, K. Matsubara, P. Fons, S. Kashiwaya, S. Niki, Y. Chiba, T. Wakamatsu, H. Kanie, Polarization-induced two-dimensional electron gases in ZnMgO/ZnO heterostructures, Applied Physics Letters, 93 (2008) 202104.
[34] P. Chen, X. Ma, D. Yang, Fairly pure ultraviolet electroluminescence from ZnO-based light-emitting devices, Applied Physics Letters, 89 (2006) 111112.
[35] J. Simon, V. Protasenko, C. Lian, H. Xing, D. Jena, Polarization-Induced Hole Doping in Wide–Band-Gap Uniaxial Semiconductor Heterostructures, Science, 327 (2010) 60-64.
[36] Efficient blue light-emitting diodes leading to bright and energy-saving white light sources, Scientific Backgrond on the Nobel Prize in Physics 2014, the Class for Physics of the Royal Swedish Academy of Sciences, 2014.
[37] J. Singleton, Band theory and electronic properties of solids, Oxford University2001.
[38] S. Nakamura, T. Mukai, M. Senoh, Candela-class high-brightness InGaN/AlGaN double-heterostructure blue-light-emitting diodes, Applied Physics Letters, 64 (1994) 1687-1689.
[39] J. Anderson, G.V.d.W. Chris, Fundamentals of zinc oxide as a semiconductor, Reports on Progress in Physics, 72 (2009) 126501.
[40] D.C. Look, R.L. Jones, J.R. Sizelove, N.Y. Garces, N.C. Giles, L.E. Halliburton, The path to ZnO devices: donor and acceptor dynamics, physica status solidi (a), 195 (2003) 171-177.

[41] H. Ohta, K.-i. Kawamura, M. Orita, M. Hirano, N. Sarukura, H. Hosono, Current injection emission from a transparent p–n junction composed of p-$SrCu_2O_2$/n-ZnO, Applied Physics Letters, 77 (2000) 475-477.
[42] Y.I. Alivov, J.E.V. Nostrand, D.C. Look, M.V. Chukichev, B.M. Ataev, Observation of 430 nm electroluminescence from ZnO/GaN heterojunction light-emitting diodes, Applied Physics Letters, 83 (2003) 2943-2945.
[43] Q.-X. Yu, B. Xu, Q.-H. Wu, Y. Liao, G.-Z. Wang, R.-C. Fang, H.-Y. Lee, C.-T. Lee, Optical properties of ZnO/GaN heterostructure and its near-ultraviolet light-emitting diode, Applied Physics Letters, 83 (2003) 4713-4715.
[44] Y.I. Alivov, E.V. Kalinina, A.E. Cherenkov, D.C. Look, B.M. Ataev, A.K. Omaev, M.V. Chukichev, D.M. Bagnall, Fabrication and characterization of n-ZnO/p-AlGaN heterojunction light-emitting diodes on 6H-SiC substrates, Applied Physics Letters, 83 (2003) 4719-4721.
[45] M.D. Regulacio, M.-Y. Han, Composition-Tunable Alloyed Semiconductor Nanocrystals, Accounts of Chemical Research, 43 (2010) 621-630.
[46] R.E. Bailey, S. Nie, Alloyed Semiconductor Quantum Dots: Tuning the Optical Properties without Changing the Particle Size, Journal of the American Chemical Society, 125 (2003) 7100-7106.
[47] T. Trindade, P. O'Brien, N.L. Pickett, Nanocrystalline Semiconductors: Synthesis, Properties, and Perspectives, Chemistry of Materials, 13 (2001) 3843-3858.
[48] Y. Dong, F. Tuomisto, B.G. Svensson, A.Y. Kuznetsov, L.J. Brillson, Vacancy defect and defect cluster energetics in ion-implanted ZnO, Physical Review B, 81 (2010) 081201.
[49] A. Gorzkowska-Sobas, A. Galeckas, M.F. Sunding, S. Diplas, A.Y. Kuznetsov, An investigation of Fe-doped ZnO thin films grown by magnetron sputtering, Physica Scripta, 2010 (2010) 014004.
[50] M. Haider, S. Uhlemann, E. Schwan, H. Rose, B. Kabius, K. Urban, Electron microscopy image enhanced, Nature, 392 (1998) 768-769.
[51] P.E. Batson, N. Dellby, O.L. Krivanek, Sub-angstrom resolution using aberration corrected electron optics, Nature, 418 (2002) 617-620.
[52] O.L. Krivanek, G.J. Corbin, N. Dellby, B.F. Elston, R.J. Keyse, M.F. Murfitt, C.S. Own, Z.S. Szilagyi, J.W. Woodruff, An electron microscope for the aberration-corrected era, Ultramicroscopy, 108 (2008) 179-195.
[53] D.A. Muller, L.F. Kourkoutis, M. Murfitt, J.H. Song, H.Y. Hwang, J. Silcox, N. Dellby, O.L. Krivanek, Atomic-Scale Chemical Imaging of Composition and Bonding by Aberration-Corrected Microscopy, Science, 319 (2008) 1073-1076.
[54] G.A. Botton, S. Lazar, C. Dwyer, Elemental mapping at the atomic scale using low accelerating voltages, Ultramicroscopy, 110 (2010) 926-934.
[55] L. Gu, V. Srot, W. Sigle, C. Koch, P. van Aken, F. Scholz, S.B. Thapa, C. Kirchner, M. Jetter, M. Rühle, Band-gap measurements of direct and indirect semiconductors using monochromated electrons, Physical Review B, 75 (2007) 195214.
[56] R. Erni, N.D. Browning, The impact of surface and retardation losses on valence electron energy-loss spectroscopy, Ultramicroscopy, 108 (2008) 84-99.
[57] L. Gu, W. Sigle, C.T. Koch, J. Nelayah, V. Srot, P.A. van Aken, Mapping of valence energy losses via energy-filtered annular dark-field scanning transmission electron microscopy, Ultramicroscopy, 109 (2009) 1164-1170.
[58] M. Stöger-Pollach, Optical properties and bandgaps from low loss EELS: Pitfalls and solutions, Micron, 39 (2008) 1092-1110.
[59] D. Keller, S. Buecheler, P. Reinhard, F. Pianezzi, D. Pohl, A. Surrey, B. Rellinghaus, R. Erni, A.N. Tiwari, Local Band Gap Measurements by VEELS of Thin Film Solar Cells, Microscopy and Microanalysis, 20 (2014) 1246-1253.

[60] R.F. Egerton, Limits to the spatial, energy and momentum resolution of electron energy-loss spectroscopy, Ultramicroscopy, 107 (2007) 575-586.
[61] R.F. Egerton, Electron Energy-loss Spectroscopy in the Electron Microscope, Plenum, New York, 2011.
[62] P. Schattschneider, C. Hébert, H. Franco, B. Jouffrey, Anisotropic relativistic cross sections for inelastic electron scattering, and the magic angle, Physical Review B, 72 (2005) 045142.
[63] W. Zhan, V. Venkatachalapathy, T. Aarholt, A.Y. Kuznetsov, Ø. Prytz, Band gap maps beyond the delocalization limit: correlation between optical band gaps and plasmon energies at the nanoscale, Scientific Reports, 8 (2018) 848.
[64] R.-w. Shao, K. Zheng, B. Wei, Y.-f. Zhang, Y.-j. Li, X.-d. Han, Z. Zhang, J. Zou, Bandgap engineering and manipulating electronic and optical properties of ZnO nanowires by uniaxial strain, Nanoscale, 6 (2014) 4936-4941.
[65] E. Okunishi, I. Ishikawa, H. Sawada, F. Hosokawa, M. Hori, Y. Kondo, Visualization of Light Elements at Ultrahigh Resolution by STEM Annular Bright Field Microscopy, Microscopy and microanalysis, 15 (2009) 164-165.
[66] M. Couillard, G. Radtke, G.A. Botton, Strain fields around dislocation arrays in a Σ9 silicon bicrystal measured by scanning transmission electron microscopy, Philosophical Magazine, 93 (2013) 1250-1267.
[67] Y. Zhu, C. Ophus, J. Ciston, H. Wang, Interface lattice displacement measurement to 1pm by geometric phase analysis on aberration-corrected HAADF STEM images, Acta Materialia, 61 (2013) 5646-5663.
[68] P.E. Batson, Simultaneous STEM imaging and electron energy-loss spectroscopy with atomic-column sensitivity, Nature, 366 (1993) 727-728.
[69] S. Francis, R. Saravanan, L.J. Berchmans, Phase analysis in $Zn_{1-x}Cr_xO$ through charge density, Phase Transitions, 86 (2013) 620-632.
[70] C.K. Moureen, T.B. Phillip, L.M. Stephanie, W.G. Michael, A.K. Joshua, S. Ram, R.S. Matthew, K. Young-Il, Crystal structures of spin-Jahn–Teller-ordered $MgCr_2O_4$ and $ZnCr_2O_4$, Journal of Physics: Condensed Matter, 25 (2013) 326001.
[71] C.L. Jia, M. Lentzen, K. Urban, Atomic-Resolution Imaging of Oxygen in Perovskite Ceramics, Science, 299 (2003) 870-873.
[72] R. Schweinfest, A.T. Paxton, M.W. Finnis, Bismuth embrittlement of copper is an atomic size effect, Nature, 432 (2004) 1008-1011.
[73] D.A. Muller, Structure and bonding at the atomic scale by scanning transmission electron microscopy, Nat Mater, 8 (2009) 263-270.
[74] C.B.C. David B. Williams, Transmission Electron Microscopy, A Textbook for Materials Science, Springer2009.
[75] Z. Qing-Hua, X. Dong-Dong, G. Lin, Aberration-corrected scanning transmission electron microscopy for complex transition metal oxides, Chinese Physics B, 25 (2016) 066803.
[76] K. Kimoto, T. Asaka, T. Nagai, M. Saito, Y. Matsui, K. Ishizuka, Element-selective imaging of atomic columns in a crystal using STEM and EELS, Nature, 450 (2007) 702-704.
[77] Z. Wang, M. Saito, K.P. McKenna, L. Gu, S. Tsukimoto, A.L. Shluger, Y. Ikuhara, Atom-resolved imaging of ordered defect superstructures at individual grain boundaries, Nature, 479 (2011) 380-383.
[78] O.L. Krivanek, M.F. Chisholm, V. Nicolosi, T.J. Pennycook, G.J. Corbin, N. Dellby, M.F. Murfitt, C.S. Own, Z.S. Szilagyi, M.P. Oxley, S.T. Pantelides, S.J. Pennycook, Atom-by-atom structural and chemical analysis by annular dark-field electron microscopy, Nature, 464 (2010) 571-574.
[79] S.J. Pennycook, L.A. Boatner, Chemically sensitive structure-imaging with a scanning transmission electron microscope, Nature, 336 (1988) 565-567.

[80] S.D. Findlay, N. Shibata, H. Sawada, E. Okunishi, Y. Kondo, T. Yamamoto, Y. Ikuhara, Robust atomic resolution imaging of light elements using scanning transmission electron microscopy, Applied Physics Letters, 95 (2009) 191913-191913-191913.
[81] http://qstem.org/.
[82] B. Rafferty, L.M. Brown, Direct and indirect transitions in the region of the band gap using electron-energy-loss spectroscopy, Physical Review B, 58 (1998) 10326-10337.
[83] F.J. García de Abajo, Optical excitations in electron microscopy, Reviews of Modern Physics, 82 (2010) 209-275.
[84] S. Lazar, G.A. Botton, M.Y. Wu, F.D. Tichelaar, H.W. Zandbergen, Materials science applications of HREELS in near edge structure analysis and low-energy loss spectroscopy, Ultramicroscopy, 96 (2003) 535-546.
[85] C.S. Granerød, W. Zhan, Ø. Prytz, Automated approaches for band gap mapping in STEM-EELS, Ultramicroscopy, 184 (2018) 39-45.
[86] A. Gutiérrez-Sosa, U. Bangert, A.J. Harvey, C. Fall, R. Jones, Energy loss spectroscopy of dislocations in GaN and diamond: a comparison of experiment and calculations, Diamond and Related Materials, 12 (2003) 1108-1112.
[87] F.K. Shan, Y.S. Yu, Optical properties of pure and Al doped ZnO thin films fabricated with plasma produced by excimer laser, Thin Solid Films, 435 (2003) 174-178.
[88] T. Minemoto, T. Negami, S. Nishiwaki, H. Takakura, Y. Hamakawa, Preparation of $Zn_{1-x}Mg_xO$ films by radio frequency magnetron sputtering, Thin Solid Films, 372 (2000) 173-176.
[89] J.-L. Zhao, X.-M. Li, J.-M. Bian, W.-D. Yu, X.-D. Gao, Structural, optical and electrical properties of ZnO films grown by pulsed laser deposition (PLD), Journal of Crystal Growth, 276 (2005) 507-512.
[90] S.A. Studenikin, N. Golego, M. Cocivera, Optical and electrical properties of undoped ZnO films grown by spray pyrolysis of zinc nitrate solution, Journal of Applied Physics, 83 (1998) 2104-2111.
[91] V. Srikant, D.R. Clarke, Optical absorption edge of ZnO thin films: The effect of substrate, Journal of Applied Physics, 81 (1997) 6357-6364.
[92] R.S.-G. C. Bundesmann , M. Schubert, Transparent Conductive Zinc Oxide, Springer, Materials Science, Berlin, Heidelberg, 2008, pp. 79-124.
[93] X. Kong, S. Albert, A. Bengoechea-Encabo, M.A. Sanchez-Garcia, E. Calleja, A. Trampert, Plasmon excitation in electron energy-loss spectroscopy for determination of indium concentration in (In,Ga)N/GaN nanowires, Nanotechnology, 23 (2012) 485701.
[94] J. Palisaitis, C.L. Hsiao, M. Junaid, J. Birch, L. Hultman, P.O.Å. Persson, Effect of strain on low-loss electron energy loss spectra of group-III nitrides, Physical Review B, 84 (2011) 245301.
[95] G. Qin, Q.-B. Yan, Z. Qin, S.-Y. Yue, H.-J. Cui, Q.-R. Zheng, G. Su, Hinge-like structure induced unusual properties of black phosphorus and new strategies to improve the thermoelectric performance, Scientific Reports, 4 (2014) 6946.
[96] J. Palisaitis, C.L. Hsiao, L. Hultman, J. Birch, P.O.Å. Persson, Direct observation of spinodal decomposition phenomena in InAlN alloys during in-situ STEM heating, Scientific Reports, 7 (2017) 44390.
[97] A. Hörling, L. Hultman, M. Odén, J. Sjölén, L. Karlsson, Thermal stability of arc evaporated high aluminum-content $Ti_{1-x}Al_xN$ thin films, Journal of Vacuum Science & Technology A, 20 (2002) 1815-1823.
[98] L. Yedra, E. Xuriguera, M. Estrader, A. López-Ortega, M.D. Baró, J. Nogués, M. Roldan, M. Varela, S. Estradé, F. Peiró, Oxide Wizard: An EELS Application to Characterize the White Lines of Transition Metal Edges, Microscopy and Microanalysis, 20 (2014) 698-705.

[99] T. Riedl, T. Gemming, K. Wetzig, Extraction of EELS white-line intensities of manganese compounds: Methods, accuracy, and valence sensitivity, Ultramicroscopy, 106 (2006) 284-291.
[100] D. Doutt, H.L. Mosbacker, G. Cantwell, J. Zhang, J.J. Song, L.J. Brillson, Impact of near-surface defects and morphology on ZnO luminescence, Applied Physics Letters, 94 (2009) 042111.
[101] L.J. Brillson, Y. Dong, F. Tuomisto, B.G. Svensson, A.Y. Kuznetsov, D. Doutt, H.L. Mosbacker, G. Cantwell, J. Zhang, J.J. Song, Z.-Q. Fang, D.C. Look, Interplay of native point defects with ZnO Schottky barriers and doping, Journal of Vacuum Science & Technology B, 30 (2012) 050801.
[102] M.J. Hytch, J.-L. Putaux, J.-M. Penisson, Measurement of the displacement field of dislocations to 0.03 Å by electron microscopy, Nature, 423 (2003) 270-273.
[103] M.J. Hÿtch, J.L. Putaux, J. Thibault, Stress and strain around grain-boundary dislocations measured by high-resolution electron microscopy, Philosophical Magazine, 86 (2006) 4641-4656.
[104] C.L. Johnson, E. Snoeck, M. Ezcurdia, B. Rodriguez-Gonzalez, I. Pastoriza-Santos, L.M. Liz-Marzan, M.J. Hytch, Effects of elastic anisotropy on strain distributions in decahedral gold nanoparticles, Nat Mater, 7 (2008) 120-124.
[105] Y.L. Tang, Y.L. Zhu, X.L. Ma, On the benefit of aberration-corrected HAADF-STEM for strain determination and its application to tailoring ferroelectric domain patterns, Ultramicroscopy, 160 (2016) 57-63.
[106] D.O. Klenov, S. Stemmer, Contributions to the contrast in experimental high-angle annular dark-field images, Ultramicroscopy, 106 (2006) 889-901.
[107] P.D.N. S. J. Pennycook, Scanning Transmission Electron Microscopy Imaging and Analysis, Springer, NewYork, 2011.
[108] J.M. LeBeau, S.D. Findlay, L.J. Allen, S. Stemmer, Quantitative Atomic Resolution Scanning Transmission Electron Microscopy, Physical Review Letters, 100 (2008) 206101.
[109] Y. Liu, Y.-L. Zhu, Y.-L. Tang, Y.-J. Wang, Y.-X. Jiang, Y.-B. Xu, B. Zhang, X.-L. Ma, Local Enhancement of Polarization at $PbTiO_3$/$BiFeO_3$ Interfaces Mediated by Charge Transfer, Nano Letters, 17 (2017) 3619-3628.
[110] A. Ohtomo, H.Y. Hwang, A high-mobility electron gas at the $LaAlO_3$/$SrTiO_3$ heterointerface, Nature, 427 (2004) 423.
[111] N. Reyren, S. Thiel, A.D. Caviglia, L.F. Kourkoutis, G. Hammerl, C. Richter, C.W. Schneider, T. Kopp, A.S. Rüetschi, D. Jaccard, M. Gabay, D.A. Muller, J.M. Triscone, J. Mannhart, Superconducting Interfaces Between Insulating Oxides, Science, 317 (2007) 1196.
[112] H. Lee, N. Campbell, J. Lee, T.J. Asel, T.R. Paudel, H. Zhou, J.W. Lee, B. Noesges, J. Seo, B. Park, L.J. Brillson, S.H. Oh, E.Y. Tsymbal, M.S. Rzchowski, C.B. Eom, Direct observation of a two-dimensional hole gas at oxide interfaces, Nature Materials, 17 (2018) 231-236.
[113] J. Palisaitis, C.L. Hsiao, M. Junaid, M. Xie, V. Darakchieva, J.F. Carlin, N. Grandjean, J. Birch, L. Hultman, O.Å. Persson Per, Standard-free composition measurements of $Al_xIn_{1-x}N$ by low-loss electron energy loss spectroscopy, physica status solidi (RRL) – Rapid Research Letters, 5 (2010) 50-52.

Paper I

W. Zhan, C. S. Granerød, V. Venkatachalapathy, K. M. H. Johansen, I. J. T. Jensen, A. Y. Kuznetsov and Ø. Prytz

Nanoscale mapping of optical band gaps using monochromated electron energy loss spectroscopy

Nanotechnology 28, 105703 (2017)

I

Paper II

W. Zhan, V. Venkatachalapathy, T. Aarholt, A. Y. Kuznetsov and Ø. Prytz

Band gap maps beyond the delocalization limit: correlation between optical band gaps and plasmon energies at the nanoscale

Scientific Reports 8, 848 (2018)

II

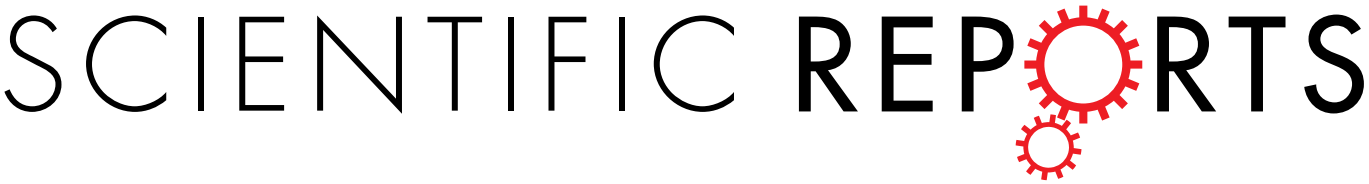

OPEN

Band gap maps beyond the delocalization limit: correlation between optical band gaps and plasmon energies at the nanoscale

Received: 23 August 2017
Accepted: 20 December 2017
Published online: 16 January 2018

Wei Zhan, Vishnukanthan Venkatachalapathy, Thomas Aarholt, Andrej Yu. Kuznetsov & Øystein Prytz

Recent progresses in nanoscale semiconductor technology have heightened the need for measurements of band gaps with high spatial resolution. Band gap mapping can be performed through a combination of probe-corrected scanning transmission electron microscopy (STEM) and monochromated electron energy-loss spectroscopy (EELS), but are rare owing to the complexity of the experiments and the data analysis. Furthermore, although this method is far superior in terms of spatial resolution to any other techniques, it is still fundamentally resolution-limited due to inelastic delocalization of the EELS signal. In this work we have established a quantitative correlation between optical band gaps and plasmon energies using the $Zn_{1-x}Cd_xO$/ZnO system as an example, thereby side-stepping the fundamental resolution limits of band gap measurements, and providing a simple and convenient approach to achieve band gap maps with unprecedented spatial resolution.

Wurtzite ZnO, with a wide direct band gap (E_g) of ~3.3 eV, can be alloyed with rock salt CdO (direct band gap of ~2.3 eV). Incorporation of Cd into ZnO matrix reduces the band gap, resulting in band gap tunability from UV to the visible spectral range[1], while maintaining superior properties of the direct band gap[2,3], thereby benefitting device performance[1]. As previous research illustrates, conventional tools such as photoluminescence (PL)[1], cathodoluminescence (CL)[4], optical absorption[5] and X-ray photoelectron spectroscopy (XPS)[6] are very useful for band gap structure measurement of doped ZnO with high energy resolution. However, they suffered from limited spatial resolution (several microns) and can only reveal one-dimensional band gap structure, thus calling for the application of high resolution techniques.

Monochromated electron energy-loss spectroscopy (EELS)[7,8] in a scanning transmission electron microscope (STEM)[9] is highly suited for this purpose. Moreover, aberration correctors in STEM[10], allowing more electrons to be brought to a focused spot, greatly enhance the signal-to-noise ratio[11–13]. Specifically, over the past decade, these developments have contributed to detailed studies of semiconductor band gaps[14–18]. Most recently, band gap mapping with spatial resolution well below 10 nm has been proved using monochromated EELS in probe-corrected STEM without special setup of the microscope[19], differing remarkably from the research carried out by Lin Gu *et al.*[16], who developed energy-filtered STEM to enable the band gap mapping. Experimentally obtained EEL spectra give access to detailed information about the dielectric response, and can be directly compared to theoretical simulations[20,21].

Despite these advancements, experimental and data processing challenges in EELS band gap analysis[19,22] hinder wide-spread application of band gap mapping, so that nanoscale band gap measurements are still very rare. Furthermore, the identification of the band gap signal can be complicated by the presence of additional loss mechanisms such as the excitation of surface plasmons, guided light modes, and Cherenkov radiation. Finally, although the spatial resolution realized in the direct mapping of band gap transitions in EELS is far superior to that of other techniques, it is still unfortunately limited by the fundamentals of the scattering process[23]. This means that resolution below the theoretically predicted inelastic delocalization length (L_{50}) of 5–7 nm is probably not feasible regardless of future technical advances in instrumentation.

Department of Physics, Centre for Materials Science and Nanotechnology, University of Oslo, P.O. Box 1048 Blindern, N-0316, Oslo, Norway. Correspondence and requests for materials should be addressed to Ø.P. (email: oystein.prytz@fys.uio.no)

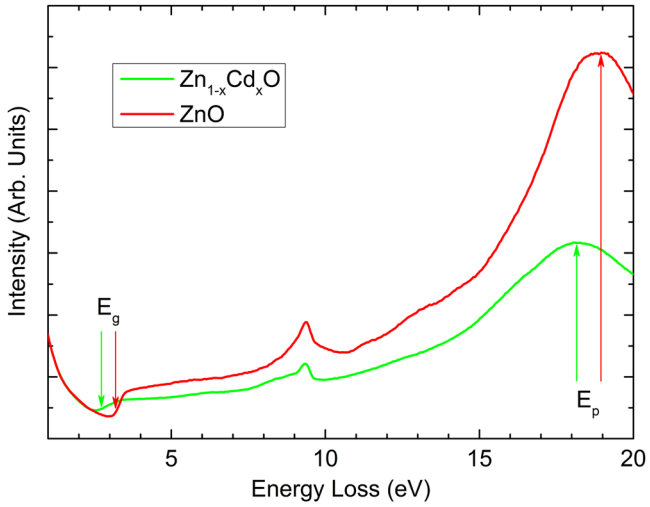

Figure 1. Two single EELS spectra taken from the pure ZnO and Cd-containing layers. Shifts of the plasmon and band gap energies are clearly observed as indicated by arrows.

In this work, using monochromated EELS in probe-corrected STEM, we investigate the relationship between band gaps and plasmon energies, and establish a robust quantitative correlation using in the ZnO-CdO alloys as an example. This provides a fast and effortless pathway to carry out band gap mapping that can be performed without the need of special hardware such as monochromators or probe Cs correctors, and with much less complexity in the experimental acquisition and data analysis. We furthermore show that using this approach we achieve a higher spatial resolution than the conventional method, without compromising the accuracy.

Background

In the periodic table, Cd is located directly below Zn and can therefore be considered iso-electronic. However, Cd has a significantly larger ionic radius than Zn, and when Cd^{2+} ions (radius 0.097 nm) replace Zn^{2+} (radius 0.074 nm) in the wurtzite ZnO matrix, the unit cell volume is increased while the band gap is reduced[1,4,24,25].

Meanwhile, higher Cd content is also associated with a drop in plasmon energy, since the valence electron density decreases as the unit cell volume expands. The plasmons are collective excitations of valence electrons triggered by their collective response to the repulsive field carried by the incident electron. In a free electron model, the plasmon energy is given by[25]:

$$E_{p,F} = \hbar\omega_p = \hbar\sqrt{\frac{Ne^2}{V(x)m_0\varepsilon_0}} \tag{1}$$

where $E_{p,F}$ is the free electron plasmon energy in EELS spectrum, ω_p is the plasmon frequency, $\hbar$ is the reduced Planck constant, N is the number of valence electrons per unit cell, e is the elementary charge, $V(x)$ is the Cd-concentration dependent volume of unit cell, m_0 is the electron mass, and ε_0 is the permittivity of free space. This free electron model assumes that the valence electrons behave as simple harmonic oscillators, which is an obvious simplification when considering real materials. Nevertheless, many simple metals (e.g. Be, B, Na, Al) and semiconductors (e.g. Si, Ge, GaAs) have sharp plasmon peaks near the value predicted by this model[26], and it has also been shown that Equation (1) is quite successful in estimating the plasmon energy of more complex materials[21].

For wide band gap semiconductors, the free electron model can be modified by introducing a bound oscillation with frequency $\omega_b = E_g/\hbar$, so that a semi-free electron plasmon energy can be obtained[25]:

$$E_{p,sF} = \sqrt{E_{p,F}^2 + E_g^2} \tag{2}$$

thereby improving the correspondence with the experimental values somewhat.

As both the band gap and plasmon energy depend on the Cd concentration (x), these models predict a relationship between the band gap and the plasmon energy: via the volume alone in the case of the free electron model, while in the semi-free model the band gap energy also appears directly. This indicates that a quantitative connection between the plasmon and band gap energies may be formulated. This theory is elaborated further in the Supplementary Information section 5, and forms the basic justification for the approach taken in the present work.

Results

Shifts of E_g and E_p of ZnO after incorporation of Cd. Figure 1 illustrates experimental spectra obtained from the pure ZnO buffer layer and the alloyed layer with a large amount of Cd. Both the plasmon peaks and the band gap energy loss onsets are easily identified. To extract the band gap value, a power-law model was used to reliably subtract the background signal at energies $E < E_g$, and a parabola was fitted to the remaining spectrum,

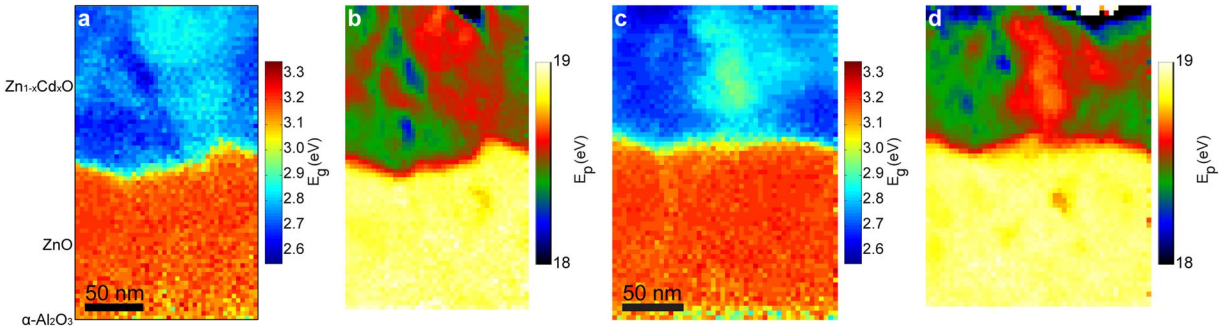

Figure 2. Directly measured (**a**) band gap and (**b**) plasmon energy maps of $Zn_{1-x}Cd_xO/ZnO/\alpha\text{-}Al_2O_3$. Directly measured (**c**) band gap and (**d**) plasmon energy maps from a different region. $Zn_{1-x}Cd_xO$ was grown on the $\alpha\text{-}Al_2O_3$ substrate with a ZnO buffer layer in between.

further details about this procedure can be found elsewhere[18,19]. In pure ZnO, the average band gap is found to be 3.22 ± 0.02 eV using the fitting range 2.4–2.9 eV for background subtraction (Supplementary Fig. S8a), in agreement with previous investigations[19]. In order to measure the plasmon energy, we first employed the Fourier-log method, as implemented in DigitalMicrograph, to remove plural scattering. Thereafter the EELS spectra within a selected narrow energy range were fitted with a Gaussian function to determine the plasmon peak positions. The average plasmon energy of ZnO is 18.88 ± 0.02 eV (Supplementary Fig. S1), consistent with previous reports[27,28]. In comparison, the free electron model (Equation (1)) predicts a theoretical value of 18.64 eV, while the semi-free model (Equation (2)) using the observed band gap as an input leads to a higher value of 18.92 eV. Thus, the two models, and the semi-free model in particular, are in good agreement with the experimental observation. For the Cd-containing layer, Fig. 1 shows that both E_g and E_p are shifted to lower energies, as expected from the unit cell volume expansion caused by the incorporation of Cd atoms into the structure.

Simultaneous E_g and E_p maps. Figure 2 shows band gap and plasmon energy maps of $Zn_{1-x}Cd_xO/ZnO$ taken from two different areas. Red and yellow colors indicate a high band gap or plasmon energy, while blue and green imply a lower value. As demonstrated by energy-dispersive X-ray spectroscopy (EDX) maps obtained for Cd and Zn (see Supplementary Figs S2 and S3), the film exhibits the expected two-layer structure, with an inner buffer layer consisting of pure ZnO, and an outer layer of Cd-containing ZnO[19]. The $\alpha\text{-}Al_2O_3$ substrate is situated at the bottom. The thickness of each layer is about 120 nm. The transition from ZnO to the $Zn_{1-x}Cd_xO$ layer is clearly visible as a rather abrupt drop in E_g or E_p values. However, the interface between ZnO and $Zn_{1-x}Cd_xO$ is rough. Furthermore, we observed that there are significant spatial variations of band gaps and plasmon energies internally in the Cd-containing layers. Intriguingly, their variations match very well, and are supported by the elemental EDX maps in Supplementary Information. These EDX measurements confirm that the higher Cd content is correlated with decreasing band gap and plasmon energy, and that the maximum Cd content (x) in our specimens is ≈0.51. Previous work[2] shows that $Zn_{1-x}Cd_xO$ stabilizes single-phase wurtzite with Cd content x up to 0.67, this is also confirmed by our X-ray diffraction investigations.

In comparison, the variations observed in Fig. 2 within the pure ZnO layer are much smaller, suggesting a high spectral precision. Note that the optical band gaps and plasmon energies were simultaneously acquired pixel by pixel. Therefore these maps with point-to-point correspondence are well suited to investigate their relationship and establish a quantitative correlation. Importantly, the plasmon energy map displays a significantly better spatial resolution than the band gap map, and there are some small energy variations that are undetectable in the band gap map. This is expected from the difference in EELS spatial resolving ability, which depends on the energy loss as well as high tension of the microscope. As an example, in the current experimental setup with 60 keV incident electrons, the EELS spatial resolution as expressed by the inelastic delocalization length (L_{50}) is estimated to be approximately 5.41 nm for the band gap transitions in ZnO, and 1.46 nm in the case of its plasmon excitations[23,25,29]. See the Supplementary Information for further details.

Quantitative correlation between E_g and E_p. To establish a quantitative relationship between the plasmon energy and band gap, several experiments such as those in Fig. 2 were performed on different regions of the sample. In Fig. 3 we have plotted the observed band gap and plasmon energy in 13876 pixels (spectra) originating from eleven different spectrum images, sufficient for establishing the quantitative correlation. Owing to the poorer spatial resolution of the band gap map, several different plasmon energies may be observed for each particular value of the band gap. This is indicated by the error bars which show the spread (one standard deviation) of plasmon energies around the average value.

As shown in the Supplementary Information a relationship between the plasmon energy and band gap can be derived. In the free electron model this relationship is as follows:

$$E_{p,F} = a_* \sqrt{\frac{2bg - cf + \sqrt{4E_g c^2 g - 4c^2 eg + c^2 f^2}}{2(b^2 g + c^2 e - bcf - E_g c^2)}} \tag{3}$$

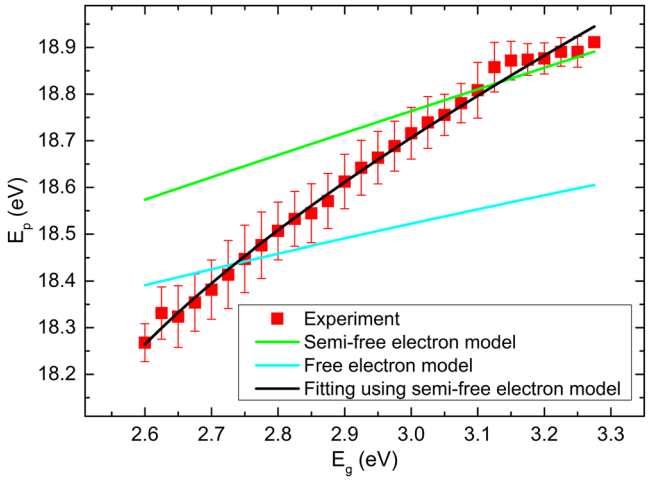

Figure 3. The observed $E_p - E_g$ correlation plotted together with the values predicted from the free and semi-free electron models based on literature inputs. The fitting of the semi-free electron model to the experimental data is plotted in black.

Parameter	Literature value	Fitted value (semi-free model)	Comment/Reference
a	128.566	128.4767	From free electron plasmon model, see Equation (S3)
b	47.6093	47.6093	ZnO unit cell volume. Reference[24]
c	4.14502	4.139997	Reference[24]
d	0	—	Reference[24]
e	3.37	3.215	Band gap of pure ZnO. Reference[3]
f	−2.82	−1.194	Band bowing parameter. Reference[3]
g	0.95	0.45	Band bowing parameter. Reference[3]
N	12	11.98	Valence electron numbers in ZnO unit cell are used to calculate literature value of a. The fitted value 11.98 is calculated from the fitted value of a.

Table 1. Fitting parameters for experimental data and Eq. 4.

while for semiconductor or insulator the semi-free model should be used, resulting in the following equation:

$$E_{p,sF} = \sqrt{E_g^{\,2} + a^2 \frac{2bg - cf + \sqrt{4E_g c^2 g - 4c^2 eg + c^2 f^2}}{2(b^2 g + c^2 e - bcf - E_g c^2)}} \tag{4}$$

Here, a, b, c, d, e, f, g and N are all constants that can be found in literature, see Table 1 for an overview.

The relationship predicted between E_g and E_p predicted by the free and semi-free electron models using the literature inputs from Table 1 are plotted in Fig. 3. It can be seen that the two models are somewhat successful in estimating the plasmon energy in the low gap and high gap range respectively, but neither of the models offer satisfactory results over the entire range.

We now follow two different routes to establish the quantitative relationship between the band gap and plasmon energy. First a polynomial function relating E_g and E_p is fitted on the basis of the experimental data, as shown in Supplementary Fig. S5. Although this results in a rather exact fit, it does not directly relate to any of the physical parameters that serve as determining factors in the variation of band gap and plasmon energy. Instead, we take Equation (4) above as a starting point, and use the constants as fitting parameters, arriving at a correlation described by the black line in Fig. 3 and the parameters in Table 1. An excellent match with the observed correlation can be achieved, while at the same time retaining physically realistic and meaningful fitting parameters. It is particularly encouraging that reasonable values of the unit cell volume and the band gap are kept. It needs to be pointed out that the Cd compositional range in our work differs significantly from the literature[3], resulting in a significant discrepancy between the fitted and the literature values of f and g.

Reconstructed E_g map with improved spatial resolution. The proposed relationship between the plasmon energy and band gap can now be employed to reconstruct band gap maps from plasmon energy maps. It was not possible to acquire an analytical solution of Equation (4) for E_g in terms of E_p. Instead, the equation was solved numerically by slowly increasing E_g until a value equal or larger than E_p was found, for each pixel of a plasmon energy map. See the Supplementary Information for attached python code. This was applied to the two data sets shown in Fig. 2. The resulting reconstructed band gap maps are shown in Figs 4a and 5a. For convenience, the

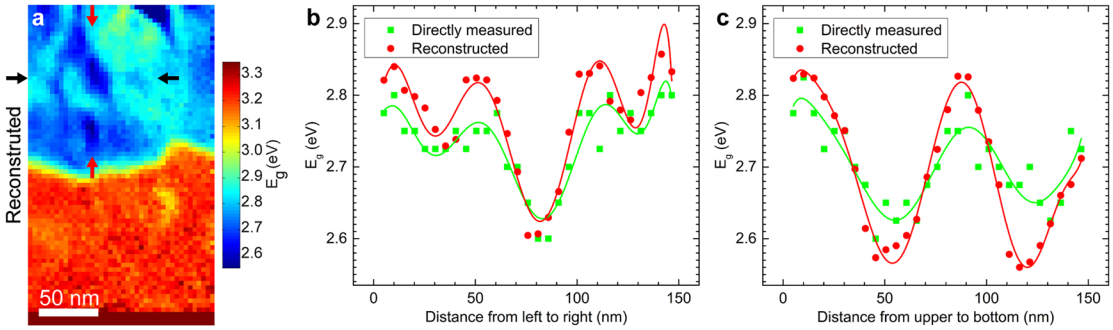

Figure 4. (**a**) Band gap map reconstructed from the plasmon energy map (Fig. 2b) using the semi-free electron fitting. The arrows display the start and end points of the two lines chosen for analysis in (**b**), (**c**). Directly measured (Fig. 2a) and reconstructed E_g along the horizontal (**b**) and vertical (**c**) line profiles. Polynomial curves are superimposed to guide the eyes.

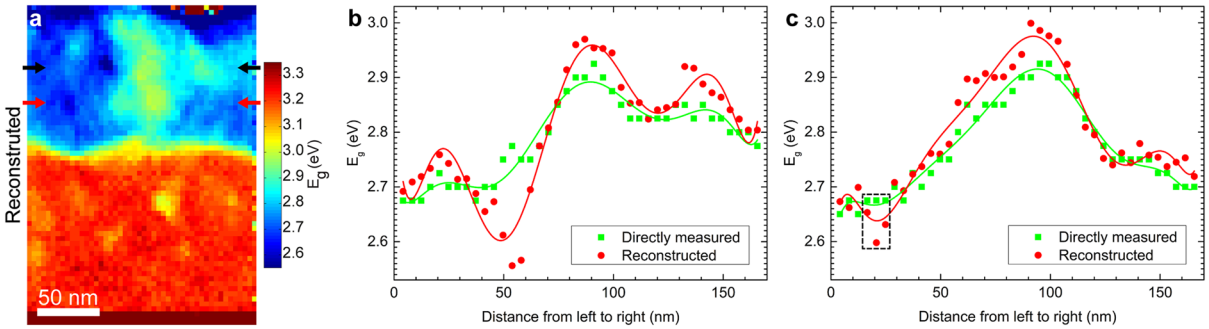

Figure 5. (**a**) Band gap map reconstructed from the plasmon energy map (Fig. 2d) using the semi-free electron fitting. The arrows display the start and end points of the two lines chosen for analysis in (**b**), (**c**). Directly measured (Fig. 2c) and reconstructed E_g along the top (**b**) and bottom (**c**) horizontal line profiles. Polynomial curves are superimposed to guide the eyes.

color scale here remains the same as the directly measured E_g map in Fig. 2a,c. As expected, the directly measured and reconstructed maps show a strong similarity, but the reconstructed map clearly resolves several additional variations not observable in the directly measured E_g maps. Line profiles from the reconstructed maps are shown in Figs 4b,c and 5b,c together with the corresponding line profiles from the directly measured maps as indicated by red and black arrows. These line profiles confirm that a greater resolution is achieved in the reconstructed maps.

Furthermore, as shown in Supplementary Fig. S8a,b, the reconstructed band gaps in the chemically homogeneous ZnO layer are very close to the directly measured values. By averaging over 260 pixels an average value of the reconstructed band gap of 3.24 ± 0.02 eV is obtained compared to the directly measured value of 3.22 ± 0.02 eV, thereby showing that a good accuracy is retained. Note that, in Figs 4b,c and 5b,c, the band gap values are revealed by the data points, and the polynomial curves are just added as a guide to the eye. Both the directly measured and reconstructed maps exhibit some standard deviations, which causes the shifts of the maximum (or minimum) position of the polynomial curves.

Discussion

Compared to the directly measured band gap maps, the reconstructed maps have significantly higher spatial resolution. As shown in Figs 4 and 5, the two methods capture the same general features, but the reconstructed map reveal both higher and lower absolute values. There are two effects contributing to this difference. First, in the case of the directly measured band gap maps, the incident electron not only experience energy transfer to excitations "locally", but also to transitions taking place some distance away from the position where it penetrates the specimen. This inelastic delocalization of the signal causes a spectrum from one position on the sample to have contributions from a larger volume, quantified as an inelastic delocalization length (L_{50}, contributing 50% of the signal) of approximately 6 nm (see Supplementary Information for more details). Second, to create the band gap map, the experimental spectra need to be analyzed in order to identify the onset of energy loss corresponding to the band gap. In this process, even small or moderate contributions from adjacent areas can weigh heavily and thereby causing a broadening of the features[19,22]. For a feature to be resolved using this direct mapping method, it must therefore be quite large both spatially and spectrally.

These problems are greatly reduced when using the E_p-to-E_g reconstruction approach. First, the inelastic delocalization is much smaller in the case of plasmon losses, and second, the data processing now only requires determination of the plasmon peak position, a procedure that is much less influenced by contributions from adjacent areas than attempting to find an energy loss onset. The improvements in resolution are clearly evident in the finer details of Fig. 5. Here several features that were not resolved in the directly measured maps now become apparent. For example, in Fig. 5c (dashed box) we see a sharp drop in the band gap between adjacent points in the reconstructed data. The distance between these points is only 4.14 nm, while the E_g reduction is well above the statistical error. In comparison, this feature is completely missing in the directly measured data.

As mentioned in Supplementary Information section 3, the spatial resolution of the directly measured band gaps could in theory be improved by using a different experimental setup. If a specific spatial resolution is required for a given excitation energy, the resolution could in principle be improved by lowering the accelerating voltage of the microscope. However, as shown in Supplementary Fig. S4, a dramatic reduction in accelerating voltage is needed to reduce the inelastic delocalization to comparable levels as that predicted for plasmon losses at 19 eV: an L_{50} of 1.46 nm is achieved for 3 eV band gaps only by reducing the accelerating voltage below 0.18 kV. While monochromatic electron beams with such low energy can indeed be generated, the increase in beam size (and resulting reduction in resolution) far outweighs the improvement in inelastic delocalization. In comparison, the E_p-to-E_g reconstruction approach can be used on regular samples at standard accelerating voltages, while still achieving excellent spatial resolution, accuracy and precision.

Conclusions

In summary, taking advantage of state-of-the-art monochromated EELS in conjunction with probe-corrected STEM, the local optical band gaps and plasmon energies of $Zn_{1-x}Cd_xO$/ZnO were simultaneously mapped on the nanometer scale with a high level of spectral precision, and their quantitative correlation was successfully established. This provides a practical method to acquire semiconductor band gap values via plasmon energies, with drastically improved spatial resolution as compared to the direct measurement of the band gap. These findings pave the way for studies of band gap engineered semiconductor nanostructures with spatial resolution beyond the traditional delocalization limits, with the added benefit of greatly relaxed requirements on hardware and data processing.

Methods

Thin-film specimen of $Zn_{1-x}Cd_xO$ with variable Cd concentrations was synthesized by metal organic vapour phase epitaxy (MOVPE) on α-Al_2O_3 substrate along the [0001] axis buffered with a pure ZnO layer. The sample for STEM investigations was prepared by cutting the slices along the [0001] direction of α-Al_2O_3. These slices were then mechanically ground to 150 μm, after which the slices were made into wedges with a tilt angle of 2.5°, using the MultiPrep System (Allied High Tech Products, USA). One side of the slices was further ground down to 20 μm. Thereafter the ground side was thinned by the low-angle ion milling & polishing system (Fischione 1010) with gun voltages of 5 kV/4 kV/3 kV, gun currents of 5 mA/4 mA/3 mA, and an incident beam angle of 8°. The total milling time was about 3 h.

Immediately before the STEM experiments were performed, the sample was plasma cleaned in a Fischione Model 1020 plasma cleaner. The STEM investigations were undertaken in a probe-corrected and monochromated FEI Titan G2 60–300, equipped with a Fischione HAADF detector (3000), a Gatan GIF Quantum 965 EELS spectrometer, and four FEI Super-X EDX detectors. The actual content of Cd in $Zn_{1-x}Cd_xO$ was studied by EDX maps at a 300 kV accelerating voltage. Zn Kα and Cd Lα characteristic X-ray peaks were used for EDX quantification of content, and Cd content was determined to be $0.01 < x < 0.51$. To prevent the Cherenkov radiation from overlapping with the band gap, monochromated EELS spectrum imaging were operated at a high tension of 60 kV, close to Cherenkov limit of ZnO. The specimens were finally thinned to be approximately 20~30 nm, further efficiently eliminating the unwanted retardation losses. The dispersion of the 2048-channel EELS spectrometer was set at 0.025 eV/channel in order to simultaneously collect the signals of band gap and plasmon energy pixel by pixel. To guarantee sufficient signals for EELS spectrum image, the time for exposure at each pixel was very close to the limiting exposure for the CCD. Before carrying out the structural and spectral mapping, the α-Al_2O_3 substrate was tilted to the $[2\bar{1}\bar{1}\ 0]$ orientation to make the electron beam perpendicular to the film growth direction. During the EELS or EDX spectrum imaging, software correction of the spatial drift was employed.

The energy resolution in the monochromated EELS measurements was approximately 0.175 eV, as determined by the full width at half maximum (FWHM) of the zero-loss peak (ZLP). The band gap is identified as the onset of energy loss (similar to the onset of absorption in optical absorption experiments) followed by fitting a parabolic model to the spectrum after background subtraction. An EELS spectroscopic image is composed of many pixels (spectra). The parabolic fitting performed at each spectrum would eventually lead to a two-dimensional band gap image. A detailed explanation of the steps taken for band gap fitting has been published previously[19,22]. The plasmon energy values in EELS spectrum were obtained by fitting a Gaussian function in DigitalMicrograph, before which plural scattering was removed using the Fourier-log method.The datasets generated during and/or analyzed during the current study are available from the corresponding author upon a reasonable request.

References

1. Du, X. L. *et al*. Controlled Growth of High-Quality ZnO-Based Films and Fabrication of Visible-Blind and Solar-Blind Ultra-Violet Detectors. *Adv. Mater.* **21**, 4625 (2009).
2. Detert, D. M. *et al*. Crystal structure and properties of CdxZn1−xO alloys across the full composition range. *Applied Physics Letters* **102**, (2013).
3. Wang, X. J. *et al*. Band gap properties of Zn1−xCdxO alloys grown by molecular-beam epitaxy. *Applied Physics Letters* **89**, 151909 (2006).
4. Dong, Y., Tuomisto, F., Svensson, B. G., Kuznetsov, A. Y. & Brillson, L. J. Vacancy defect and defect cluster energetics in ion-implanted ZnO. *Physical Review B* **81**, 081201 (2010).

5. Makino, T. *et al*. Band gap engineering based on MgxZn1−xO and CdyZn1−yO ternary alloy films. *Applied Physics Letters* **78**, 1237–1239 (2001).
6. Gorzkowska-Sobas, A., Galeckas, A., Sunding, M. F., Diplas, S. & Kuznetsov, A. Y. An investigation of Fe-doped ZnO thin films grown by magnetron sputtering. *Physica Scripta* **2010**, 014004 (2010).
7. Erni, R. & Browning, N. D. Valence electron energy-loss spectroscopy in monochromated scanning transmission electron microscopy. *Ultramicroscopy* **104**, 176–192 (2005).
8. Egerton, R. F. Electron energy-loss spectroscopy in the TEM. *Reports on Progress in Physics* **72**, 016502 (2009).
9. Batson, P. E., Dellby, N. & Krivanek, O. L. Sub-angstrom resolution using aberration corrected electron optics. *Nature* **418**, 617–620 (2002).
10. Muller, D. A. Structure and bonding at the atomic scale by scanning transmission electron microscopy. *Nat Mater* **8**, 263–270 (2009).
11. Krivanek, O. L. *et al*. An electron microscope for the aberration-corrected era. *Ultramicroscopy* **108**, 179–195 (2008).
12. Muller, D. A. *et al*. Atomic-Scale Chemical Imaging of Composition and Bonding by Aberration-Corrected Microscopy. *Science* **319**, 1073–1076 (2008).
13. Botton, G. A., Lazar, S. & Dwyer, C. Elemental mapping at the atomic scale using low accelerating voltages. *Ultramicroscopy* **110**, 926–934 (2010).
14. Gu, L. *et al*. Band-gap measurements of direct and indirect semiconductors using monochromated electrons. *Physical Review B* **75**, 195214 (2007).
15. Erni, R. & Browning, N. D. The impact of surface and retardation losses on valence electron energy-loss spectroscopy. *Ultramicroscopy* **108**, 84–99 (2008).
16. Gu, L. *et al*. Mapping of valence energy losses via energy-filtered annular dark-field scanning transmission electron microscopy. *Ultramicroscopy* **109**, 1164–1170 (2009).
17. Stöger-Pollach, M. Optical properties and bandgaps from low loss EELS: Pitfalls and solutions. *Micron* **39**, 1092–1110 (2008).
18. Keller, D. *et al*. Local Band Gap Measurements by VEELS of Thin Film Solar Cells. *Microscopy and Microanalysis* **20**, 1246–1253 (2014).
19. Zhan, W. *et al*. Nanoscale mapping of optical band gaps using monochromated electron energy loss spectroscopy. *Nanotechnology* **28**, 105703 (2017).
20. Hwanhui Yun, M. T. *et al*. Electronic structure of BaSnO3 investigated by high-energy-resolution electron energy-loss spectroscopy and ab initio calculations. *arXiv* **1611**, 09284 (2016).
21. Prytz, Ø., Løvvik, O. M. & Taftø, J. Comparison of theoretical and experimental dielectric functions: Electron energy-loss spectroscopy and density-functional calculations on skutterudites. *Physical Review B* **74**, 245109 (2006).
22. Granerød, C. S., Zhan, W. & Prytz, Ø. Automated approaches for band gap mapping in STEM-EELS. *Ultramicroscopy* **184**, 39–45 (2018).
23. Egerton, R. F. Limits to the spatial, energy and momentum resolution of electron energy-loss spectroscopy. *Ultramicroscopy* **107**, 575–586 (2007).
24. Manoranjan, G. & Raychaudhuri, A. K. Structure and optical properties of Cd-substituted ZnO (Zn 1−x Cd x O) nanostructures synthesized by the high-pressure solution route. *Nanotechnology* **18**, 115618 (2007).
25. Egerton, R. F. *Electron Energy-Loss Spectroscopy in the Electron Microscope*. (Springer, New York, 2011).
26. Raether, H. *Excitation of Plasmons and Interband Transitions by Electrons*. (Springer-Verlag Berlin Heidelberg, Berlin, 1980).
27. Ong, H. C., Dai, J. Y. & Du, G. T. Studies of electronic structure of ZnO grain boundary and its proximity by using spatially resolved electron energy loss spectroscopy. *Applied Physics Letters* **81**, 277–279 (2002).
28. Wu, L. L. & Zhang, X. T. Facile fabrication of ZnO:S/ZnO hetero-nanostructures and their electronic structure investigation by electron energy loss spectroscopy. *Cryst Eng Comm* **17**, 2250–2254 (2015).
29. Schattschneider, P., Hébert, C., Franco, H. & Jouffrey, B. Anisotropic relativistic cross sections for inelastic electron scattering, and the magic angle. *Physical Review B* **72**, 045142 (2005).

Acknowledgements

The authors would like to acknowledge support from the Research council of Norway through the Norwegian Center for Transmission Electron Microscopy, NORTEM (197405/F50), the Norwegian Micro- and Nano-Fabrication Facility, NorFab (197411/V30), as well as the FriPRO Toppforsk project FUNDAMeNT (no. 251131) and the MIDAS project (no. 228578).

Author Contributions

Wei Zhan prepared the TEM samples, performed the TEM/STEM/EELS/EDX experiments, carried out data analysis, and wrote the manuscript under the supervision of Øystein Prytz and Andrej Yu. Kuznetsov. Vishnukanthan Venkatachalapathy synthesized the thin films, while Thomas Aarholt wrote the code for numerical conversion of plasmon energies to band gaps. All authors contributed to discussions and writing of the manuscript.

Additional Information

Supplementary information accompanies this paper at https://doi.org/10.1038/s41598-017-18949-9.

Competing Interests: The authors declare that they have no competing interests.

Publisher's note: Springer Nature remains neutral with regard to jurisdictional claims in published maps and institutional affiliations.

Supplementary Information

Band gap maps beyond the delocalization limit: correlation between optical band gaps and plasmon energies at the nanoscale

Wei Zhan, Vishnukanthan Venkatachalapathy, Thomas Aarholt, Andrej Yu. Kuznetsov, and Øystein Prytz*

Department of Physics, Centre for Materials Science and Nanotechnology, University of Oslo, P.O. Box 1048 Blindern, N-0316 Oslo, Norway

*E-mail: oystein.prytz@fys.uio.no

1. Determination of ZnO plasmon energy

As shown in Supplementary Fig. S1, employing monochromated EELS in combination with probe-corrected STEM, the average plasmon energy found for the pure ZnO layer is approximately 18.88 eV by extracting from 260 pixels, and their standard deviation (σ) is typically 0.02 eV. The plasmon energy is in good agreement with previous measurements [1, 2].

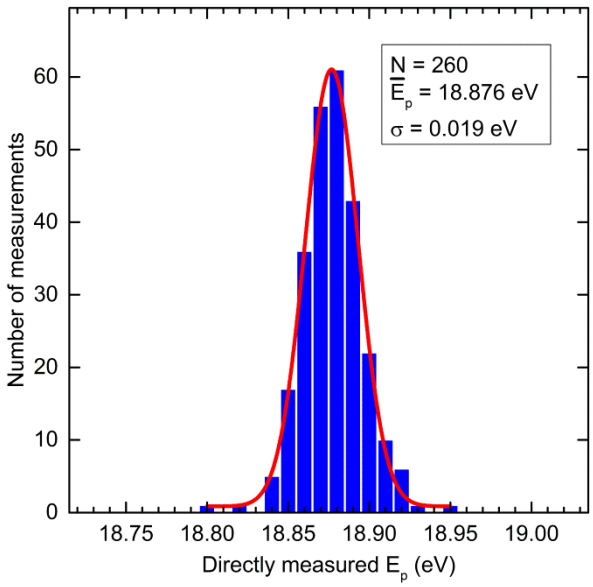

Supplementary Figure S1. Histogram of the plasmon energy values as extracted from the pure ZnO buffer layer, superimposed by a Gaussian fitting.

2. EDX maps of the E_g and E_p imaging areas

Supplementary Figure S2 illustrates annular dark-field (ADF) STEM image and EDX maps of $Zn_{1-x}Cd_xO$/ZnO observed from the same position as band gap and plasmon energy imaging in Fig. 2a,b (main text). By comparison, a conclusion can be drawn: the decrease (rise) of band gap or plasmon energy in the Cd-containing layer is correlated with the rise (drop) of Cd content x. The α-Al_2O_3 substrate is located at the bottom, and in the plasmon maps (Figs. 2b and 2d main text), the color is white (not visible) since its value (>19 eV) is out of the color range chosen for E_p in $Zn_{1-x}Cd_xO$/ZnO. Note that the band gap and plasmon energy variations in the α-Al_2O_3 substrate are outside the scope of this study.

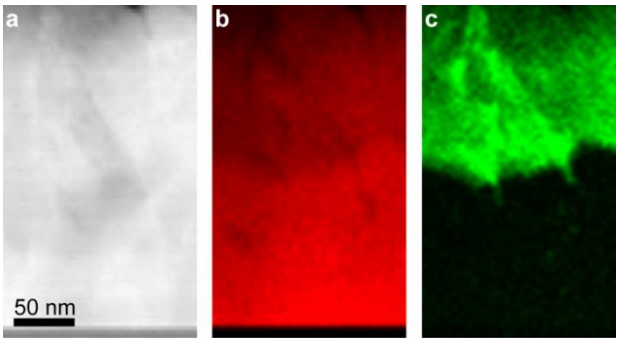

Supplementary Figure S2. (a) ADF image of $Zn_{1-x}Cd_xO/ZnO/\alpha\text{-}Al_2O_3$. EDX maps of (b) Zn and (c) Cd from the same area of Fig. 2a,b (main text).

Supplementary Figure S3 displays ADF image and EDX maps of $Zn_{1-x}Cd_xO/ZnO$ taken from the same position as Fig. 2c,d (main text). Cd content changes here are consistent with the variations in band gap and plasmon energy.

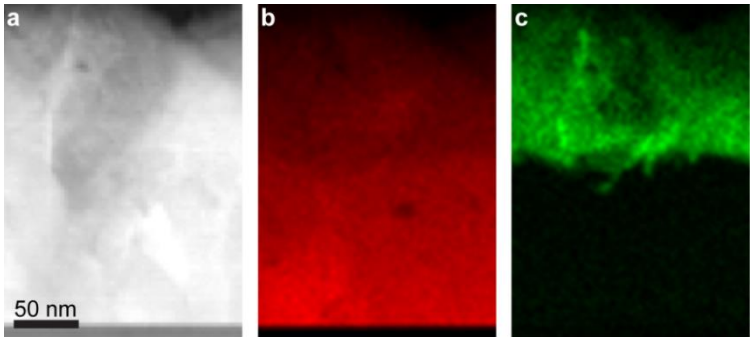

Supplementary Figure S3. (a) ADF image of $Zn_{1-x}Cd_xO/ZnO/\alpha\text{-}Al_2O_3$. EDX maps of (b) Zn and (c) Cd from the same region of Fig. 2c,d (main text).

3. EELS spatial resolution

It has been mentioned in main text that experimental and analytical difficulties remain a barrier to the wide-spread adoption of STEM-EELS band gap mapping [3, 4]. The setup of hardware required, especially monochromator, is accounted for the complexity in performing experiment. It is known that monochromators can greatly improve energy resolution by energy-filtering the incident beam. However, it also significantly reduces the beam current and thereby the observable signal. Lin Gu and co-authors [5] proposed energy-filtered STEM to improve the signal collection and thus make band gap mapping possible. In comparison, there is no special instrumental design required in this work (nor in our previous research [3, 4]). In fact, we set the exposure time of each pixel close to the limiting exposure for the CCD. In addition, the thin sample, long-time acquisition and good adjacent environment also helped the measurements.

The factors that affect EELS spatial resolution are described below. In previous work [6-8] it has been reported that the spatial resolution is determined by the inelastic delocalization length

$$L_{50} = \frac{0.44hc_0[eU(eU + 2m_0{c_0}^2)]^{\frac{1}{4}}}{[E(eU + m_0{c_0}^2)]^{\frac{3}{4}}} \quad \text{(S1)}$$

where L_{50} is the diameter containing 50% of the inelastic scattering events, h is the Planck constant, c_0 is light speed, e is elementary charge, U is accelerating voltage, m_0 is electron

mass, E is energy loss.

As can be seen from Equation (S1), the spatial resolution (L_{50}) depends on energy loss (E) and accelerating voltage (U). The spatial resolution could therefore in theory be improved by reducing the accelerating voltage of the microscope. However, for a particular energy loss, even quite dramatic reductions in accelerating voltage have only a modest effect on the spatial resolution, which limits the usefulness of this approach. To exemplify this we have plotted L_{50} for two relevant energy losses (19 eV and 3 eV) as a function of microscope accelerating voltage. As shown in Supplementary Fig. S4, for a direct measurement of a band gap edge at 3 eV to reach the same level of inelastic delocalization as a plasmon loss of 19 eV, the accelerating voltage would have to be reduced e.g. from 60 kV to 0.18 kV.

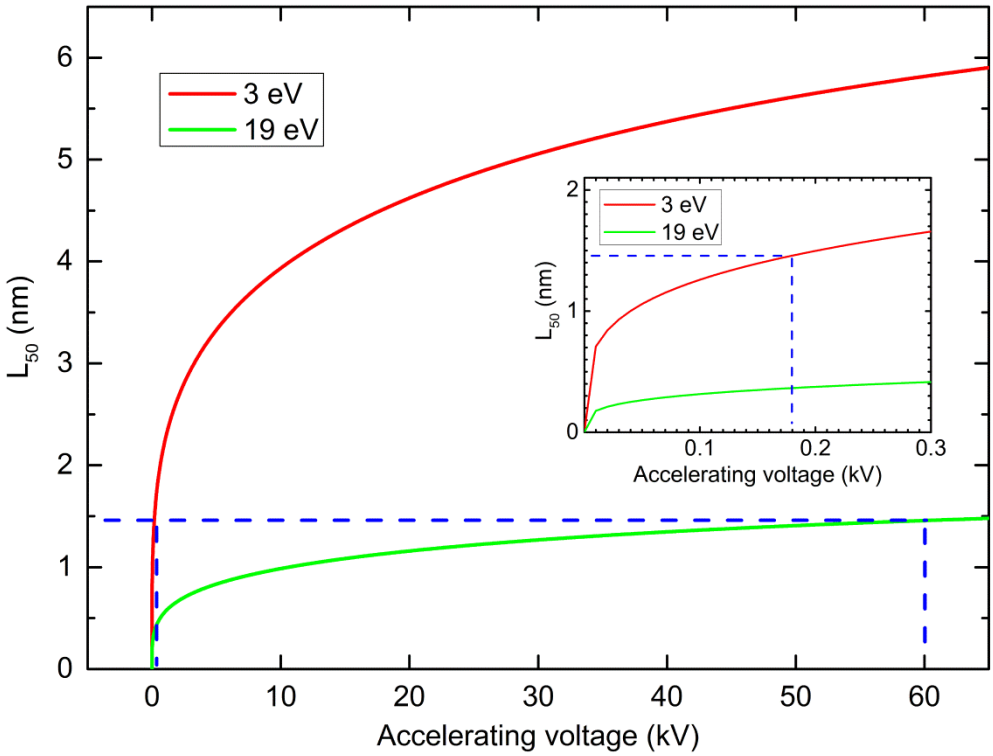

Supplementary Figure S4. The inelastic delocalization length L_{50} plotted as a function of microscope accelerating voltage for two relevant energy losses. The inset shows a closeup of the bottom left part of the plot. In order to achieve similar delocalization for a directly measured band gap at 3 eV, the accelerating voltage would have to be reduced to 0.18 kV.

4. Quantifying the correlation between E_p and E_g using polynomial function

There is a clear correlation between the observed plasmon energies and band gaps, see Supplementary Fig. S5. To quantitatively relate the two, a simple polynomial function can be fitted to the experimental data as follows.

$$E_p = A + B * E_g + C * {E_g}^D \quad \text{(S2)}$$

where A, B, C and D are fitting parameters, with the resulting values listed in Supplementary Table S1. The fitting of the experimental data adopting Eq. (S2) is displayed in Supplementary Fig. S5. We find that the polynomial gives a good fit to the experimental data. However, when using such a polynomial function, we cannot expect the fitting parameters to correspond to any physical properties of the material. In the main text we have therefore chosen a physical model for the correlation, which is derived in the next section.

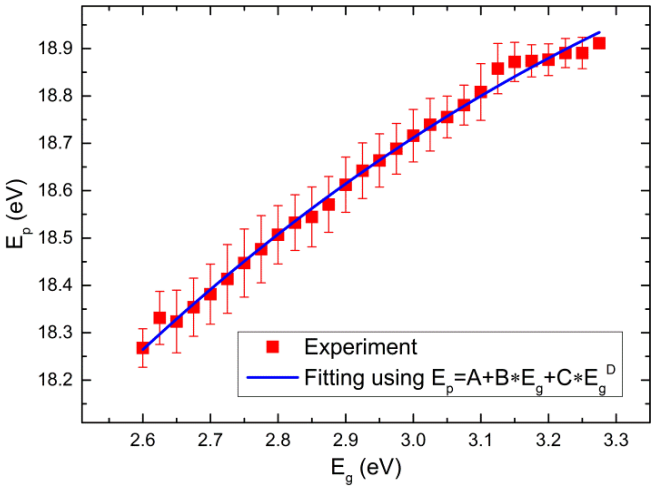

Supplementary Figure S5. Fitting the experimental data using Equation (S2).

Constant	Fitting values
A	-0.859843
B	-4.23272
C	19.0521
D	0.479655

Supplementary Table S1. Parameters in the polynomial fitting equation of the experimental data.

5. Free and semi-free electron models for plasmon oscillations

Instead of a polynomial fitting as used in the previous section, we can adopt the two well-known models to provide a fitting function. In the free electron model, for solids with loosely bound outer-shell electrons, the frequency of resonant oscillation is ω_p, giving the free electron plasmon energy [7]

$$E_{p,F} = \hbar\omega_p = \hbar\sqrt{\frac{Ne^2}{V(x)m_0\varepsilon_0}} = \frac{a}{\sqrt{V(x)}} \tag{S3}$$

with $a = \hbar\sqrt{\frac{Ne^2}{m_0\varepsilon_0}}$. For ZnO $(x = 0)$ with a unit cell volume $V = 47.6093$ Å^3 and $N = 12$ valence electrons per unit cell (2 Zn atoms with 8 electrons and 2 O atoms with 4 electrons), a free electron plasmon energy $E_{p,F} = 18.64\ eV$ is obtained.

If ZnO is alloyed with Cd, forming $Zn_{1-x}Cd_xO$, the volume of the unit cell can be described as a polynomial

$$V(x) = b + cx + dx^2 \tag{S4}$$

We will now assume $d = 0$ in accordance with Vegard's law, and fit b and c to the linear relationship found by Ghosh, et al [9]. The combination of Equations (S3) and (S4) gives the free electron plasmon energy as a function of composition x:

$$E_{p,F} = \frac{a}{\sqrt{b + cx}} \tag{S5}$$

The main emphasis of this research lies in the correlation between band gap and plasmon energy, and Wang's band bowing formula as follows can be used [10].

$$E_g(x) = e + fx + gx^2 \tag{S6}$$

Combining Equations (S5) and (S6) we arrive at the set of four equations:

$$E_{p,F} = -a * \sqrt{\frac{2bg - cf - \sqrt{4E_g c^2 g - 4c^2 eg + c^2 f^2}}{2(b^2 g + c^2 e - bcf - E_g c^2)}} \tag{S7a}$$

$$E_{p,F} = a * \sqrt{\frac{2bg - cf - \sqrt{4E_g c^2 g - 4c^2 eg + c^2 f^2}}{2(b^2 g + c^2 e - bcf - E_g c^2)}} \tag{S7b}$$

$$E_{p,F} = -a * \sqrt{\frac{2bg - cf + \sqrt{4E_g c^2 g - 4c^2 eg + c^2 f^2}}{2(b^2 g + c^2 e - bcf - E_g c^2)}} \tag{S7c}$$

$$E_{p,F} = a * \sqrt{\frac{2bg - cf + \sqrt{4E_g c^2 g - 4c^2 eg + c^2 f^2}}{2(b^2 g + c^2 e - bcf - E_g c^2)}} \tag{S7d}$$

These four branches are plotted in Supplementary Fig. S6. Only the fourth branch, corresponding to Equation (S7d), provides physical results with $0 \leq x \leq 1$. Solving instead for E_g the expression below is obtained:

$$E_g = g\left(\frac{a^2}{{E_p}^2 c} - \frac{b}{c}\right)^2 + f\left(\frac{a^2}{{E_p}^2 c} - \frac{b}{c}\right) + e \tag{S8}$$

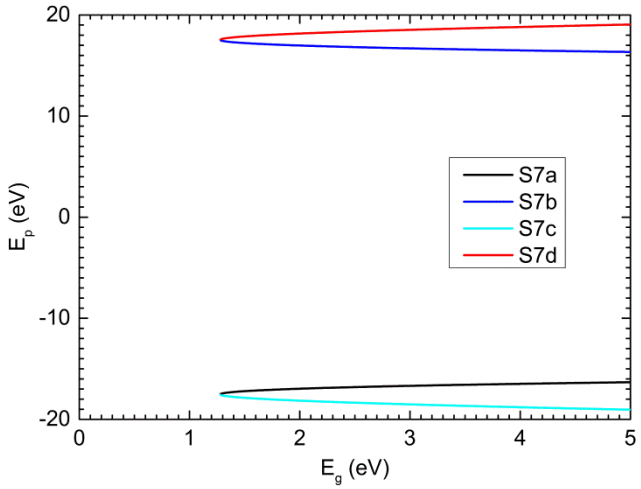

Supplementary Figure S6. The four branches (S7a, S7b, S7c, S7d) plotted together.

The free electron model assumed in Equation (S3) will underestimate the observed plasmon energy in semiconductors with a wide band gap. For semiconductor or insulator, a modified version of the plasmon energy takes into account bound electrons with a resonance frequency

ω_b. Setting $\hbar\omega_b = E_g$ brings about the semi-free plasmon energy [7]:

$$E_{p,sF} = \sqrt{E_{p,F}^2 + E_g^2} = \sqrt{\left(\hbar\sqrt{\frac{Ne^2}{V(x)m_0\varepsilon_0}}\right)^2 + E_g^2} = \sqrt{\frac{a^2}{V(x)} + E_g^2} \tag{S9}$$

Using a band gap energy $E_g = 3.22\,eV$, this model leads to a plasmon energy $E_{p,sF} = 18.92\,eV$, which is closer to the experimentally observed value of $E_{p,exp} = 18.88 \pm 0.02\,eV$ than the free electron model.

Further, to obtain plasmon energy as a function of band gap, we proceed in the same manner as before. There are four solutions, only one of which gives physically meaningful results:

$$E_{p,sF} = \sqrt{{E_g}^2 + a^2\frac{2bg - cf + \sqrt{4E_g c^2 g - 4c^2 eg + c^2 f^2}}{2(b^2 g + c^2 e - bcf - E_g c^2)}} \tag{S10}$$

where a, b, c, d, e, f, g, N are all constants, as summarized in Table 1 (main text).

In Supplementary Fig. S7, the two models are plotted together.

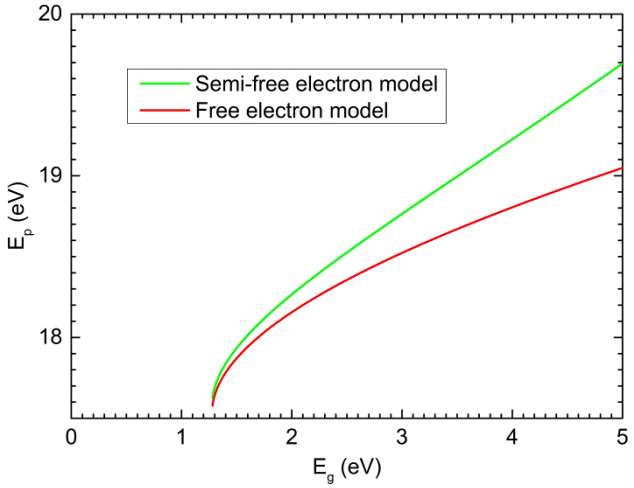

Supplementary Figure S7. Free electron model and semi-free electron model plotted together.

6. Numerical conversion of E_p to reconstructed E_g

The fitted E_p-E_g equation adopting semi-free electron model is a monotonically increasing function within the range of E_g (from minimum to maximum), as can also be seen from the fitting curve in Fig. 3 (main text). This implies that there is only one band gap value for a particular plasmon energy, based on which the reconstructed band gap can be extracted. The code that is employed to process E_p-to-E_g conversion maps is given below.

```
import hyperspy.api as hs
import numpy as np
import matplotlib.pyplot as plt
import os

path = r"M:\pc\Dokumenter\Notebooks\EpEg"
path = os.path.join(path, "")
name = "Plasmon Map.dm3"
```

```
s = hs.load(path + name)
### Settings constants for the relation Eg -> Ep
a = 128.476702120452
b = 47.6093
c = 4.13999650371382
e = 3.21530501740307
f = -1.19423330394094
g = 0.450088043947096

constants = a,b,c,e,f,g

def Eg_to_Ep(Eg, constants):
    import math
    a,b,c,e,f,g = constants
    return math.sqrt(
        Eg**2 + a**2*(2*b*g-c*f+math.sqrt(4*Eg*c**2*g-4*c**2*e*g+c**2*f**2))
        /(2*(b**2*g+c**2*e-b*c*f-Eg*c**2)))

Ep_signal = s
Eg_signal = s.deepcopy()

Ep = Eg_signal.data

Egvalues = np.arange(2.5,76,0.001)
EgtoEpConversionArray = np.array([Eg_to_Ep(i, constants) for i in Egvalues])

ourEgvalues = Egvalues[EgtoEpConversionArray < 19.5]
ourEpvalues = EgtoEpConversionArray[EgtoEpConversionArray < 19.5]

def func(Epvalue, Epvalues, EpEgConversionArray):
    import numpy as np
    Egvalue = Egvalues[np.where(EgtoEpConversionArray >= Epvalue)[0][0]]
    return Egvalue

for x in np.nditer(Ep, op_flags=['readwrite']):
    x[...] = func(x, Egvalues, EgtoEpConversionArray)

# Save as tif
Eg_signal.save(path + "Eg_values.tif")
# Save for Matlab
import scipy.io
scipy.io.savemat(path+"Eg.mat", mdict={'arr': Eg_signal.data})
# Plot
Eg_signal.plot(cmap="viridis", vmin = 2.6, vmax=3.8)
```

7. Accuracy and precision of the reconstructed band gaps

As illustrated in Supplementary Fig. S8b, the average reconstructed E_g of the pure ZnO layer is approximately 3.24 eV by extracting from 260 pixels, and the standard deviation (σ) is found to be typically 0.02 eV. Compared with the directly measured map (Supplementary Fig. S8a), the reconstructed E_g map retains high precision, while the average value of the band gap is somewhat higher than when measured directly. However, the increase is marginal, and we consider the reconstruction to have good accuracy in determining absolute values of the band gap. Note that for the directly measured band gap the bin-size of the histogram is related to the spectrometer dispersion, while for the reconstructed band gap a smaller bin-size is achieved due to the higher numerical precision of the Gaussian fitting to the plasmon peak.

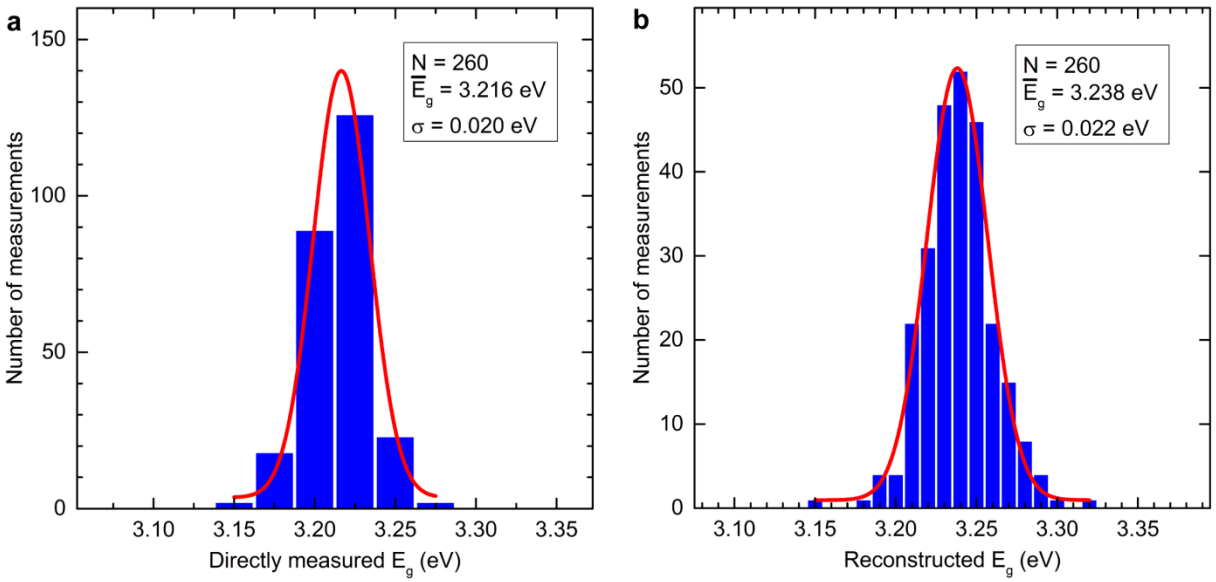

Supplementary Figure S8. Histogram of the (a) directly measured and (b) reconstructed band gaps of pure ZnO from the same region as Supplementary Fig. S1. A Gaussian fitting is superimposed, showing that the reconstructed band gap maps retain excellent precision, while the accuracy is slightly reduced.

References

1. Ong, H.C., Dai, J.Y. & Du, G.T. Studies of electronic structure of ZnO grain boundary and its proximity by using spatially resolved electron energy loss spectroscopy. *Applied Physics Letters* **81**, 277-279 (2002).
2. Wu, L.L. & Zhang, X.T. Facile fabrication of ZnO:S/ZnO hetero-nanostructures and their electronic structure investigation by electron energy loss spectroscopy. *CrystEngComm* **17**, 2250-2254 (2015).
3. Zhan, W. et al. Nanoscale mapping of optical band gaps using monochromated electron energy loss spectroscopy. *Nanotechnology* **28**, 105703 (2017).
4. Granerød, C.S., Zhan, W. & Prytz, Ø. Automated approaches for band gap mapping in STEM-EELS. *Ultramicroscopy* **184**, 39-45 (2018).
5. Gu, L. et al. Mapping of valence energy losses via energy-filtered annular dark-field scanning transmission electron microscopy. *Ultramicroscopy* **109**, 1164-1170 (2009).
6. Egerton, R.F. Limits to the spatial, energy and momentum resolution of electron energy-loss spectroscopy. *Ultramicroscopy* **107**, 575-586 (2007).
7. Egerton, R.F. Electron Energy-Loss Spectroscopy in the Electron Microscope, Edn. third. (Springer, New York; 2011).
8. Schattschneider, P., Hébert, C., Franco, H. & Jouffrey, B. Anisotropic relativistic cross sections for inelastic electron scattering, and the magic angle. *Physical Review B* **72**, 045142 (2005).
9. Manoranjan, G. & Raychaudhuri, A.K. Structure and optical properties of Cd-substituted ZnO (Zn 1− x Cd x O) nanostructures synthesized by the high-pressure solution route. *Nanotechnology* **18**, 115618 (2007).
10. Wang, X.J. et al. Band gap properties of Zn1-xCdxO alloys grown by molecular-beam epitaxy. *Applied Physics Letters* **89**, 151909-151909-151903 (2006).

Paper III

W. Zhan, A. Y. Kosinskiy, L. Vines, K. M. H. Johansen, P. A. Carvalho and Ø. Prytz

Nano $ZnCr_2O_4$ inclusions in ZnO matrix investigated by probe-corrected STEM-EELS

Submitted to Crystal Growth & Design (May 2018)

III

Paper IV

C. S. Granerød, W. Zhan, Ø. Prytz

Automated approaches for band gap mapping in STEM-EELS

Ultramicroscopy, 184, 39 (2018)

IV

Paper V

I. J. T. Jensen, K. M. H. Johansen, W. Zhan, V. Venkatachalapathy, L. Brillson, A. Y. Kuznetsov and Ø. Prytz

Bandgap and band edge positions in compositionally graded ZnCdO

Submitted to Journal of Applied Physics (April 2018)

Bandgap and band edge positions in compositionally graded ZnCdO

I.J.T. Jensen,[1,*] K.M. Johansen,[2] W. Zhan,[2] V. Venkatachalapathy,[2] L. Brillson,[3] A.Yu. Kuznetsov,[2] and Ø. Prytz[2]

[1] *SINTEF Materials and Chemistry, P/O box 124 Blindern, 0314 Oslo, Norway*
[2] *Department of Physics, University of Oslo, P/O box 1048 Blindern, 0316 Oslo, Norway*
[3] *Departments of Electrical and Computer Engineering, Department of Physics, and Center for Materials Research, Ohio State University, Columbus, Ohio 43210, USA*

(Dated: April 19, 2018)

Introducing Cd into ZnO allows for bandgap engineering, potentially with particularly interesting properties to observe in compositionally graded samples. In this work compositionally graded $Zn_{1-x}Cd_xO$ samples with $0 \leq x < 0.16$ were made using metal organic vapour phase epitaxy. The chemical composition was studied using scanning transmission electron microscopy, while the band structure of the samples was investigated using a combination of cathodoluminescence spectroscopy and X-ray photoelectron spectroscopy. It is found that the reduction of the bandgap in our samples is caused by changes in the conduction band. The position of the Fermi level relative to the vacuum level, i.e., the workfunction, was also found to change upon addition of Cd, giving an *apparent* shift in the valence band when evaluated from the XPS valence spectra.

I. INTRODUCTION

Group-II oxides represent direct wide-bandgap semiconductors that share many attractive features with group-III nitrides, making them promising for electronic applications. The unique combination of high exciton binding energy and broad bandgap tuneability range from 4.8 eV to 1.8 eV in wurtzite MgO-ZnO-CdO compounds can benefit a number of modern device applications, including recently demonstrated solar-blind photodetectors, thin-film transistors (TFT) for smart displays, tandem solar cells, as well as in yet to be established approaches in realizing light emitting diodes (LEDs), resistive switching (RS) devices, etc.[1–7] These developments, however, are hampered by several unresolved issues, notably by unreliable p-type doping, phase separation in ternary alloys, etc. Indeed, ZnO exhibits native n-type conductivity and numerous attempts to convert it to p-type by controlling acceptor-type intrinsic defects (zinc vacancy V_{Zn} and oxygen interstitials O_i) and by doping with relevant acceptor impurities (N, Na, P, Ag, etc.) have had very limited success so far.[8]

A fundamentally new way to create conductivity in non-centrosymmetric crystal structures, called polarization-induced doping (PID), was proposed by D. Jena *et al.*[9] and later demonstrated in III-nitrides by grading the composition of AlGaN along its c-axis, the direction along which the polarization dipoles lie in wurtzite.[10] In uni-axial crystals, spontaneous polarization arises due to the ionic character of the bonds between atoms and their asymmetric positions within the structure. For noncentro-symmetric crystals with a composition varying along the direction of the dipoles, a fixed (bound) polarization charge builds up because the neighbouring dipoles in the graded alloy are not of the same magnitude anymore, and thus no longer cancel each other. To maintain the overall charge neutrality, the bound polarization charge accumulated in the crystal must be compensated by mobile (free) charge carriers, which can be provided from elswhere, e.g., the surface states.[11] The outcome of such charge rearrangements is n-type (or p-type) conductivity with bound polarization charge acting as local donor (or acceptor) with zero activation energy, as well as higher carrier mobilities due to removal of ionized impurity scattering. Compositionally graded ZnCdO and ZnMgO have raised interest as possible candidates for PID. By taking advantage of the large polarization charges typical for group II oxides and controlling the composition gradient during synthesis, the resultant electric fields can be arranged in a way to create spatially separated electrons or holes without introducing dopants, potetially resolving the doping asymmetry inherent to this family of wide-bandgap semiconductors. Moreover, compositionally graded films are used as buffer layers to synthesize, e.g., ZnMgO, exhibiting ultimately high Mg content.[3] Altogether, this makes investigations of such compositionally graded samples of high interest.

Introducing Cd into ZnO reduces the bandgap (E_g), but no general framework exists for predicting the position of the band edges of $Zn_{1-x}Cd_xO$ relative to the Fermi level (E_F). The E_g reduction can be accommodated by changes either in the valence band, the conduction band, or both. Furthermore, the influence of intrinsic defects on the band structure may change as the bandgap changes, affecting the position of the Fermi level relative to the band edges, e.g., making the semiconducting material more or less p- or n-type. When materials are combined to form heterojunctions, which is central to advances in device development, the Fermi levels of the different materials will line up. The core, valence, and conduction bands may thus have to bend to make up for band structure mismatches between the two materials. It is largely the shape of the band bending across the interface, e.g., formation of barriers, that controls the device functions. This shape relies on the difference in workfunctions and the alignment of the band edges. To some extent models for predicting the shape of band bending across interfaces exist for certain materials

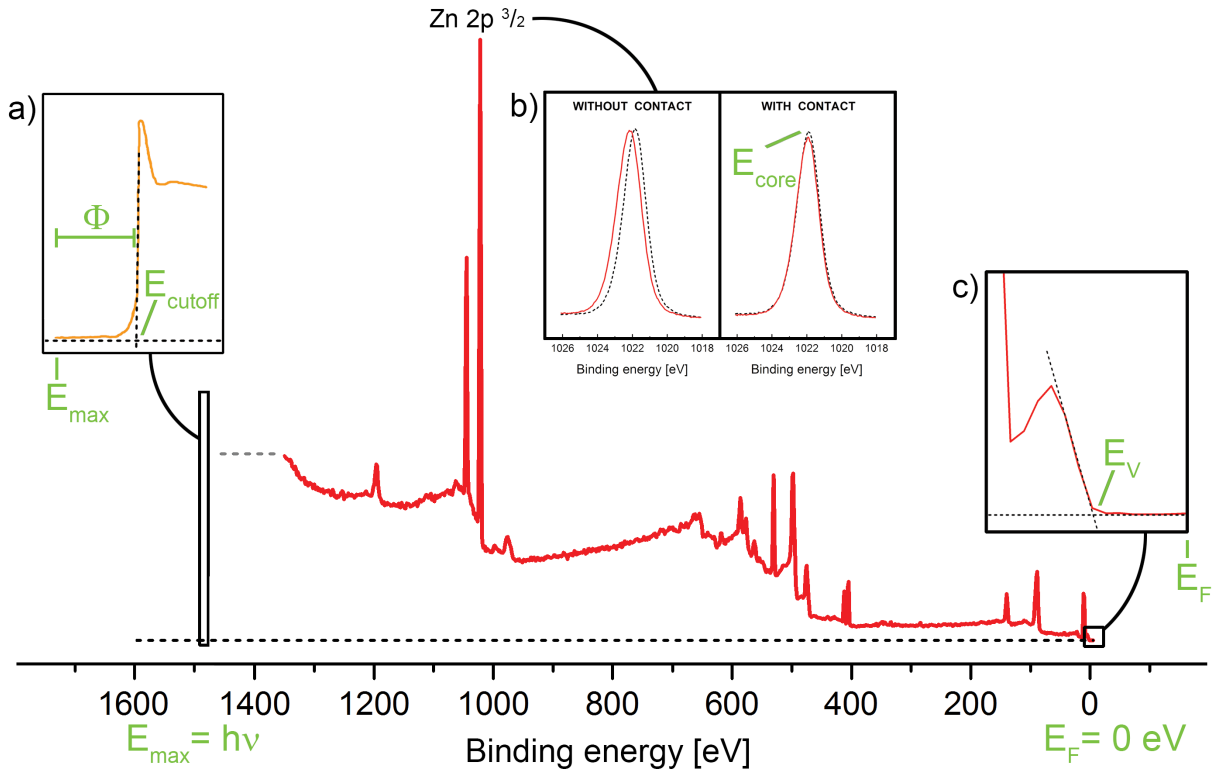

FIG. 1: (Color online) XPS survey spectrum from the Cd_{16} sample, with schematic illustrations of relevant parameters. a) Hypothetical spectrum from the high binding energy (low kinetic energy) region, which is usually not within the detectable range during normal XPS operation. E_{max} is the energy of the incoming X-rays; in the present case from an Al Kα source ($h\nu$ = 1486.6 eV). The workfunction (Φ) is the difference between E_{max} and the spectrum cutoff energy (E_{cutoff}). b) High resolution spectra from the Zn 2p 3/2 region: Test of XPS sample charging for Cd_{16} comparing mounting of clip directly onto sample (left) and mounting of clip onto Al contact (right); with and without charge compensation (dashed black and solid red line, respectively.) With contact the peak position (E_{core}) does not change significantly upon charge compensation. c) Enhanced view of the valence region, showing the valence band maximum (E_V). When the sample is in electrical contact with the instrument the Fermi level lines up with the binding energy scale ($E_F = 0$ eV).

classes, but a general understanding is still lacking.[12–14] Particularly for new alloyed materials like $Zn_{1-x}Cd_xO$, characterization of the band structure is important for potential applications.

In a density functional theory (DFT) study of the electrical and optical properties of $Zn_{1-x}Cd_xO$ with $x \leq 0.25$ Zhang *et al.*[15] found the bandgap decrease to be caused by changes in the conduction band. An increase of s states was observed upon introduction of Cd, shifting the Zn 4s states in the lowest conduction band closer to the O 2p states in the highest valence band. To date, only a few X-ray photoelectron spectroscopy (XPS) based studies of band edge positions in ZnCdO have been reported, with diverging conclusions. According to Chen *et al.*,[16] who studied molecular beam epitaxy grown samples with composition $Zn_{0.95}Cd_{0.05}O$, both the valence band maximum (E_V) and the conduction band minimum (E_C) moves relative to the Fermi level, by +0.17 eV and -0.30 eV, respectively. In a study of calcinated $Zn_{1-x}Cd_xO$ samples with $x = 0$, 0.039, 0.075 and 1, Lai *et al.* also found that both band edges shift, but with the same magnitude.[17] In the work of Detert *et al.*, however, it was concluded that the decrease in the bandgap was due to shifts in E_V only; for pulsed filtered cathodic arc deposited samples with $x = 0$, 0.11, 0.29, 0.56, 0.74 and 1.[18]

In the present work we study the composition and bandgap energy (E_g) of four compositionally graded $Zn_{1-x}Cd_xO$ samples with $0 \leq x < 0.16$ using scanning transmission electron microscopy (STEM) and cathodoluminescence spectroscopy (CL), respectively. XPS is used to find the position of the E_V relative to the Fermi level, which is combined with E_g from CL to determine the position of the E_C.

II. METHODS

Thin film samples of $Zn_{1-x}Cd_xO$ with varying Cd concentrations were prepared by metal organic vapour phase epitaxy (MOVPE) along the c axis of α-Al_2O_3 substrates buffered with a ZnO film. The substrates were

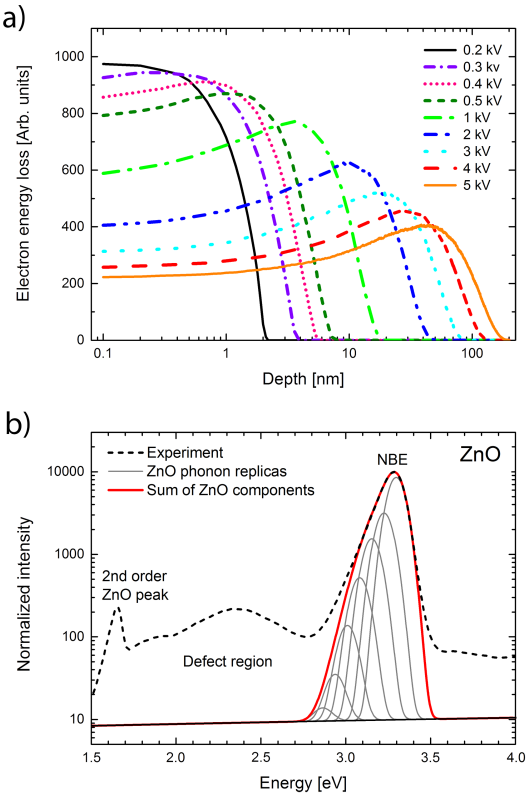

FIG. 2: (Color online) a) Calculated electron energy loss in pure ZnO as function of sample depth for different electron beam energies. b) CL spectrum from pure ZnO, illustrating fitting of the NBE peak with phonon replicas.

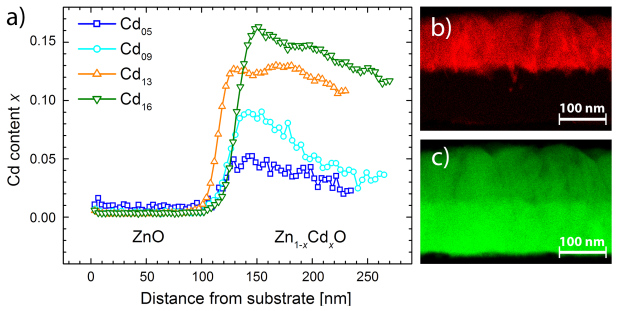

FIG. 3: (Color online) STEM-EDS investigation of sample composition: a) Cd content (x) as a function of distance from the substrate/film interface. b) Cd EDS map and c) Zn EDS map from the Cd_{13} sample.

cleaned in several solutions, rinsed by deionized water, and then dried with N_2 gas before loading into the chamber. Diethyl zinc (DEZn), dimethyl cadmium (DMCd), and tertiary butanol (t-BuOH) were used as zinc source, cadmium source, and oxidizing agent, respectively. For DEZn and t-BuOH, the flows were set at 100 and 150 sccm, respectively. The temperatures of both DEZn and DMCd bubblers were maintained at 10 °C, while that of t-BuOH was kept at 30 °C. The Cd content in the films was varied by changing the DMCd flow rate while maintaining the growth temperature at 370 °C, which means increasingly metal-rich (oxygen-poor) conditions for increasing Cd supply. The samples were labelled according to their maximum Cd content as measured by energy-dispersive X-ray spectroscopy (EDS), see details below.

XPS was performed using a Thermo Theta Probe instrument with monochromatic Al Kα radiation ($h\nu = 1486.6$ eV) operated at 15 kV and 15 mA. High resolution spectra were collected at pass energy 20 eV and step size 0.1 eV for core/Auger peaks and 0.05 eV for the VBM region. See figure 1 for a typical XPS survey spectrum and definition of relevant parameters. An area of about 2 x 2 mm^2 was gently cleaned with an Ar^+ ion beam of 0.5 kV delivering 100 μA of current for 5 minutes. In order to ensure good electrical contact between the sample and the XPS instrument, Al contacts with a thickness of $\sim$ 100 nm were applied at one corner of each sample. This was done using a Telemark e-beam source in an Angstrom Engineering EvoVac system. The samples were then mounted to the XPS stage by pressing copper clips onto the Al contact area. Figure 1 b) shows an example of charge compensation test using a low energy electron flood gun. When the sample is mounted with the copper clip onto the Al contact, no peak shift is observed when the flood gun is used, implying good electrical contact. When the sample is mounted with the copper clip directly onto the sample, however, a clear shift to lower binding energy (E_B) is observed. Thus the Al contacts were concluded to improve the electrical contact between the sample and the XPS instrument and the measurements could be performed without the use of low energy electron charge compensation. XPS spectra were fitted after Shirley[19] background substraction, using the CasaXPS software.[20]

Depth resolved CL spectra were obtained in ultra-high vacuum using an electron beam with an angle $\sim$30° off the normal incidence, with electron beam energies in the range of 0.2 to 5 keV. The spectra were analyzed by an Oriel monochromator with a slit size of 0.1 mm, and a CCD strip detector. The measurements were performed at room temperature. Each spectrum has been normalized using the near band emission (NBE) peak maximum. Figure 2 a) shows the electron energy loss as a function of the sample depth calculated for pure ZnO using the CASINO 3.2.0.4 software.[21] As can be seen, for electron beam energies up to 0.5 kV, the penetration depth is in the range of 1-10 nm, which matches the sampling depth of the XPS technique. The CL spectra were fitted using the CasaXPS software.[20] The bandgap information was extracted from the NBE peaks, which were fitted with a series of phonon replicas with 72 meV spacing.[22] The CL spectrum from the pure ZnO sample was used as a starting point for determining the shape of the NBE peaks in the $Zn_{1-x}Cd_xO$ samples. Figure 2 b) shows an example of a CL spectrum with fitted NBE peak.

For STEM studies, samples were prepared by me-

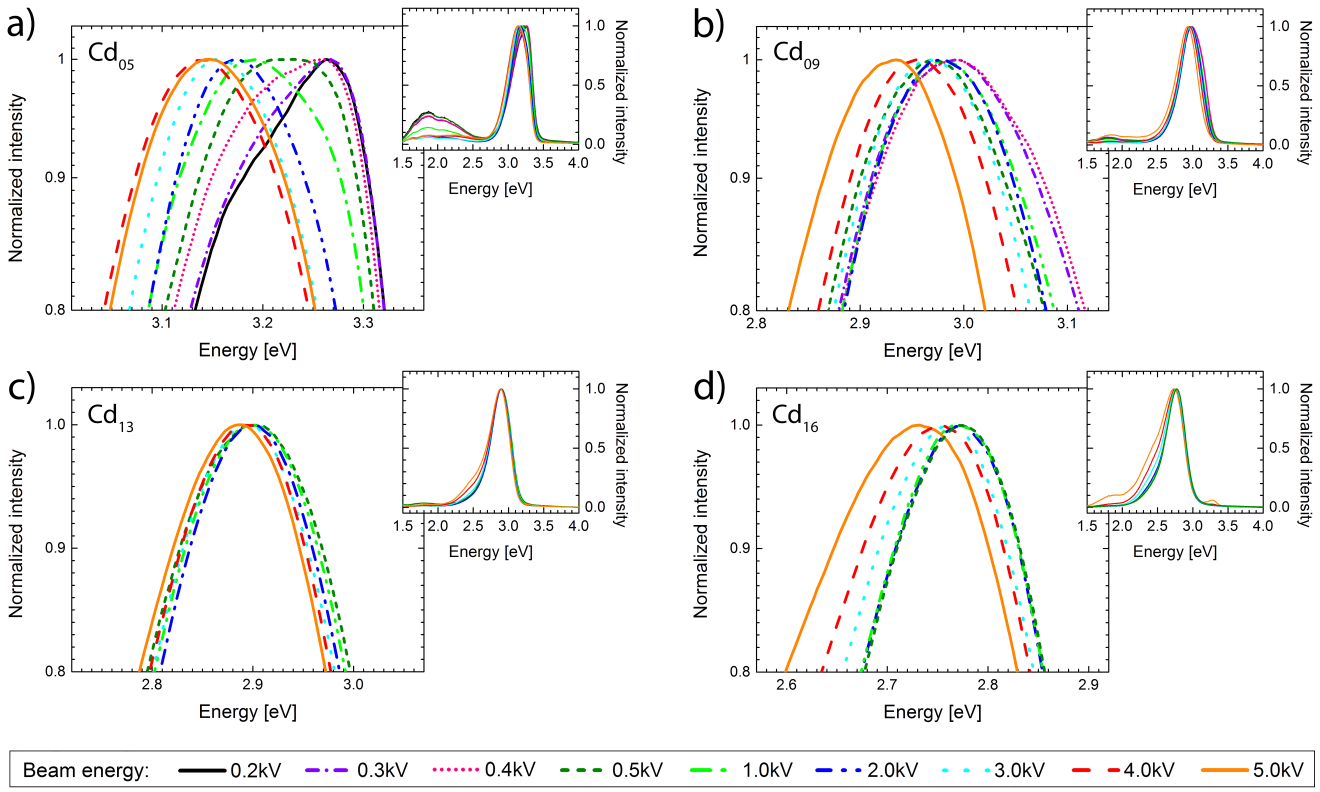

FIG. 4: (Color online) CL spectra from sample Cd_{05} (a), Cd_{09} (b), Cd_{13} (c) and Cd_{16} (d). The region around the NBE peak maximum is enhanced, while the full spectra are included as insets. In general a decrease of the bandgap is observed with increasing electron beam energy, i.e., increasing sample depth, in agreement with the gradient in Cd content.

chanical cutting, grinding/polishing, and ion beam thinning. The compositions were studied by EDS in a probe-corrected FEI Titan 60-300 instrument, which was operated in STEM mode at 300 kV. In this mode, a spatial resolution of 0.8 Å can be achieved for probe-corrected STEM imaging. The EDS maps and spectra were collected using the FEI Super-X EDS setup with four EDS detectors, thereby increasing the collection efficiency. Before STEM-EDS mapping, the sapphire substrate was tilted in the $[2\,\bar{1}\,\bar{1}0]$ zone axis, so as to make the electron beam parallel to substrate/film interface and perpendicular to the film growth direction, the c axis of the sapphire substrate. The maps and spectra were analyzed using the Bruker Esprit 1.9 software. The absolute error in the quantification was determined to be below 4.70 at%. For an in-depth STEM study of the samples, see the recent publication by Zhan *et al.*[23]

Resistivity and charge carrier density were measured at room temperature with a LakeShore 7704A Hall Measurement System using a Van der Pauw configuration. Sample thicknesses were estimated from STEM images.

III. RESULTS AND DISCUSSION

Figure 3 shows results from the STEM-EDS investigation of the samples. In order to accurately quantify the vertical grading, the compositions were averaged over areas of 109 nm x 3 nm (Cd_{05}), 53 nm x 4 nm (Cd_{09}), 408 nm x 3 nm (Cd_{13}), and 440 nm x 3 nm (Cd_{16}) to produce the line profiles in figure 3 (a). As an illustration, figure 3(b) and (c) show EDS mapping of Cd and Zn, respectively, from sample Cd_{13}. The Cd containing film is clearly distinguishable from the ZnO buffer layer. Both layers are typically about 100-120 nm thick. All samples reveal statistically significant variations in Cd content. For the samples Cd_{05}, Cd_{09} and Cd_{16} the Cd content is highest closest to the pure ZnO interface and decreases in a nearly linear manner towards the sample surface. For sample Cd_{13} the Cd content is highest in the middle of the $Zn_{1-x}Cd_xO$ film, after which it drops off again towards the sample surface. The data are listed in table I. Quantitative XPS analysis was used to determine the surface composition of the samples after gentle Ar^+ sputter removal of the carbon contamination layer. At the surface Cd_{05}, Cd_{09}, Cd_{13} and Cd_{16} were found to have $x = 0.01$, 0.03, 0.05 and 0.08, respectively. This is generally somewhat lower than the compositions measured by STEM-EDS in figure 3. This can be due to the

TABLE I: Sample details for $Zn_{1-x}Cd_xO$.

Sample name	Maximum Cd content[a)] x	Surface composition[b)] x	E_V position relative to E_F [eV]	Auger parameter Zn 2p-LMM [eV]	Surface bandgap[c)] E_g [eV]
ZnO	0.00	0.00	3.24(5)	2010.08(14)	3.31
Cd_{05}	0.05	0.01	3.24(5)	2010.16(14)	3.30
Cd_{09}	0.09	0.03	3.14(5)	2010.12(14)	3.03
Cd_{13}	0.13	0.05	3.05(5)	2010.15(14)	2.94
Cd_{16}	0.16	0.08	2.88(5)	2010.13(14)	2.80

a) Measured by STEM-EDS. b) Measured by XPS. c) Measured by CL.

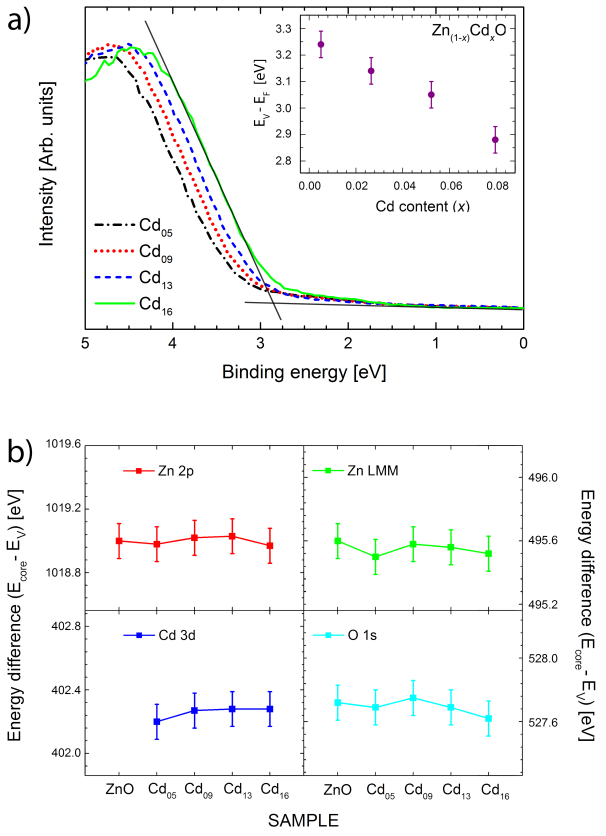

FIG. 5: (Color online) XPS results: a) Valence spectra from sample Cd_{05} (black dash-dot), Cd_{09} (red dot), Cd_{13} (blue dash) and Cd_{16} (green solid). The black intersecting lines are included to illustrate the method for E_V determination. The inset shows the distance between E_V and E_f with standard deviations, as measured from the XPS valence spectra. b) The energy difference between E_V and relevant core level peaks with standard deviations, as measured by XPS.

fact that the STEM-EDS investigation does not provide the true composition at the outermost surface, e.g., because of surface roughness. Some preferential sputtering may also occur, although the sputter yields of Zn and Cd are not severely different.[24]

Figure 4 shows CL spectra from the samples studied by STEM-EDS. A clear shift in NBE peak position is seen as a function of the electron beam energy. In general, the bandgap decreases with increasing electron beam energy, i.e., deeper penetration depth, consistent with the variation in Cd content found from STEM-EDS. For each sample the spectrum acquired at the lowest beam energy was peak fitted in order to extract bandgap values from the sample depth corresponding to the XPS measurement. The fitting strategy for such samples is not unambiguous: As shown in figure 2 b), the NBE peak contains several phonon replicas, resulting in an asymmetric overall peak shape with the true NBE position shifted to slightly higher energies than the apparent peak maximum. The width, separation, and relative intensity of the replicas depend on the material and are not known for the $Zn_{1-x}Cd_xO$ system. Furthermore, the compositional inhomogeneity of the samples means that the CL spectrum will consist of several overlapping NBE peaks from different sample regions exhibiting different bandgaps. For the present purpose we chose a simplified fitting procedure focusing on comparability between the different samples: The spectra were fitted with one main NBE peak, consisting of replica peaks with separation and relative intensity taken from pure ZnO. The full-width-at-half-maximum (FWHM), however, was allowed to increase compared to pure ZnO in order to represent the spread in bandgap values within the measurement volume. A limited number of generic defect peaks were added to the lower energy region (labelled "Defect region" in figure 2b), and for Cd_{05} and Cd_{09} the NBE peak of pure ZnO was added to the higher energy side. More elaborate peak fitting schemes were explored, but not found to offer increased accuracy due to the large number of unknown variables. The bandgap values extracted from the CL data are listed in table I.

Detailed XPS measurements of the valence region were conducted in order to find the position of the E_V as function of Cd content. A nearly linear shift in E_V as function of x is seen in figure 5 a). An important thing to remember at this point, however, is that XPS measures energies relative to E_F. Thus if the E_F position shifts within the bandgap, i.e., if the workfunction of the material changes, the entire XPS spectrum will shift accordingly. Changes

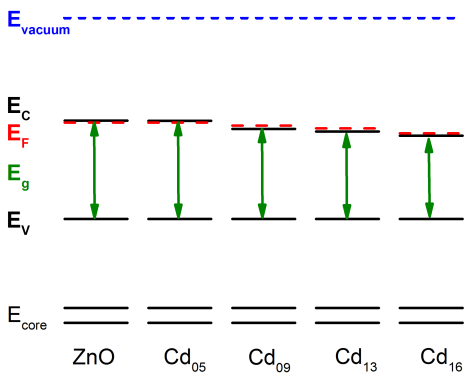

FIG. 6: (Color online) Schematic illustrations of band structure near the surface of the $Zn_{1-x}Cd_xO$ samples after alignment of the occupied levels. E_V and E_F position from XPS is combined with E_g from CL to determine E_C.

in E_F position are seen, e.g., as a result of doping. In the case of $Zn_{1-x}Cd_xO$ there is also a change in the magnitude of the bandgap, which may affect the position of the Fermi level in unknown ways. This complicates the comparison of absolute E_V positions between the samples. After analyzing the core spectra it was found that the distances between the E_V and the Zn 2p, Cd 3d and O 1s core level peaks were constant in all the samples, within the accuracy of the measurements, see figure 5 b). The Zn 2p-LMM Auger parameter[25] (AP) was also found to be constant, see Table I. It is highly unlikely that the introduction of Cd would cause both the valence levels and the core levels to shift by exactly the same amount. Sample charging, which is another possible source of uniform peak shifts, was already tested and ruled out. Thus, if we interpret the constant E_V-to-core level distances and APs as a sign that Cd does not cause changes in the valence and core levels, the relative bandstructure of the $Zn_{1-x}Cd_xO$ samples can be established using the core levels for the alignment. In figure 6 the E_V and core levels are aligned, while the distance between E_F and the vacuum level (E_{vacuum}) is seen to increase with increasing Cd content. The E_C position is found using the bandgap values as measured by low electron energy CL. Two things are worth noting from Figure 6: *i*) For the present samples the change in E_g due to Cd appears to be accommodated primarily by changes in the conduction band. *ii*) For all samples except Cd_{05}, E_F appears to lie above the E_C. Additional work is needed to clarify whether the latter is a bulk material property, or just a surface bandbending effect observed by XPS.

In Figure 7 the results of Hall measurements show an increased carrier concentration as a function of increasing Cd content. For pure ZnO, the growth conditions are slightly oxygen-rich, but with an increased DMCd-flow the growth conditions shift towards oxygen-poor/metal rich since the flow rate of t-BuOH is kept constant for all samples, explaining this general trend of increasing carrier concentration. However, for the highest Cd content (Cd_{16} sample) the carrier concentration is again reduced as compared to the Cd_{13} sample. Interestingly, the mobility is at the same time increased (not shown), which is consistent with a higher incorporation of Cd on the Zn-site combined with a lower Cd-interstitial donor concentration in the film.[26] At low DMCd flow rates, the incorporation efficiency of Cd into ZnO is low and Zn/Cd-rich conditions introduces Zn_i (or Cd_i), which acts as a donor. However, at high DMCd flow rate, the Cd incorporation efficiency increases, in turn influencing the formation of interstitial defects. Similar trend was observed by Kumar *et al.* in samples synthesized by reactive dc magnetron sputtering.[27] For pure ZnO calculations show that at 300 K $E_F \geq E_C$ for carrier concentrations exceeding 10^{19}-10^{20} cm^{-3}.[28] This suggests that the carrier concentrations measured for the present $Zn_{1-x}Cd_xO$ samples are in the right order of magnitude to exhibit degenerate behaviour. However, the values for carrier concentration extracted from Hall measurements do not take into account the compositional grading. Furthermore, a strong downward surface bandbending effect has previously been reported for pure ZnO[29] and a similar effect for $Zn_{1-x}Cd_xO$ can not be ruled out.

The bandstructure data discussed so far were extracted from the near-surface area of different samples. In the following paragraph we combine the surface data from these samples to predict the band structure evolution along the growth direction of a compositionally graded $Zn_{1-x}Cd_xO$ film. The position of E_V relative to E_F was obtained from the XPS data, while E_V could be combined with E_g found by CL, to determine the position of E_C. The obtained E_V and E_C values were plotted as function of Cd content and fitted with linear functions. These graphs were in turn incorporated into a schematic illustration of the graded ZnCdO (n-type) side of a possible PID-junction, as presented in Figure 8. It is important to note that the change in position of E_V relative to E_F in this representation of the data is not an indication of changes in the valence band. In figure 8 the Fermi levels are aligned, which is what happens upon electrical contact. This gives the impression that the valence band is changing, but is in reality an effect of bandbending; where the compositionally graded film behaves similarly to a heterostructure made of very thin layers.

IV. CONCLUSIONS

The bandgap and band edge positions of compositionally graded $Zn_{1-x}Cd_xO$ samples made by MOVPE were investigated using a combination of XPS and CL. Common pitfalls related to XPS energy referencing were resolved. Firstly it was shown how sample charging during XPS measurements can be minimized by depositing proper metal contacts onto the $Zn_{1-x}Cd_xO$ samples. Secondly it was emphasized how changes in the Fermi level position relative to vacuum, i.e., the workfunction,

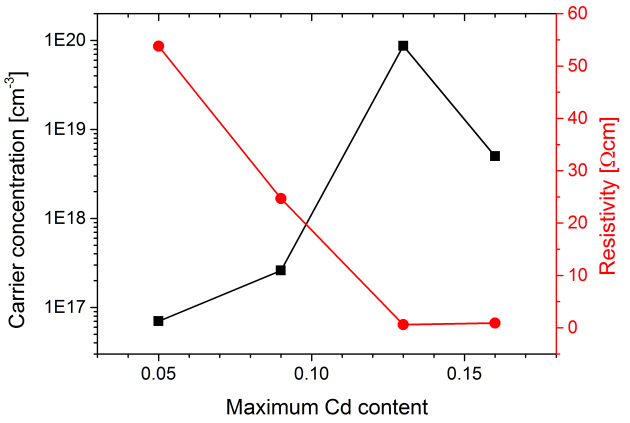

FIG. 7: (Color online) Carrier concentration (squares) and resistivity (circles) as function of maximum Cd content, obtained from Hall measurements.

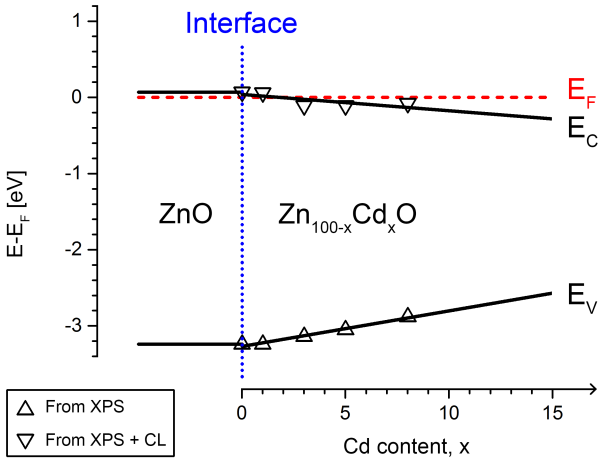

FIG. 8: (Color online) Schematic illustrations of possible band structure for compositionally graded $Zn_{1-x}Cd_xO$ on pure ZnO substrate, extrapolated from XPS and CL measurements.

complicate the comparison of XPS data from different samples. Taking the latter into account, it was found that introducing Cd into ZnO does not significantly alter the band structure below the Fermi level. Hence the reduction of the bandgap upon alloying with Cd must be accommodated primarily by changes in the conduction band. Bandgap values were obtained from low energy CL and combined with the XPS data to sketch the band structure of graded $Zn_{1-x}Cd_xO$ heterostructures.

Acknowledgement

LJB acknowledges support from National Science Foundation grant DMR-1305193. KMJ would like to thank the Norwegian Research Council for the support to the DYNAZOx project (no. 221992). AYuK and VV would like to thank the Norwegian Research Council for the support to the MIDAS project (no. 228578).

* Electronic address: IngvildThue.Jensen@sintef.no

[1] P. F. Garcia, R. S. McLean, and G. Nunes Jr., Appl. Phys. Lett. **82**, 1117 (2003).
[2] E. M. C. Fortunato, P. M. C. Barquinha, A. C. M. B. G. Pimentel, A. M. F. Goncalves, A. J. S. Marques, L. M. N. Pereira, and R. F. P. Martins, Adv. Mater. **17**, 590 (2005).
[3] X. Du, Z. Mei, Z. Liu, Y. Guo, T. Zhang, Y. Hou, Z. Zhang, Q. Xue, and A. Y. Kuznetsov, Adv. Mater. **21**, 1 (2009).
[4] M. Trunk, A. Gorzkowska-Sobas, V. Venkatachalapathy, T. Zhang, A. Galeckas, and A. Y. Kuznetsov, Energy Proc. **22**, 101 (2012).
[5] D. Ielmini, Semicond. Sci. Technol. **31**, 063002 (2016).
[6] W. Walukiewicz, D. Detert, K. M. Yu, and M. Ristova, *CdZnO/Si Tandem Cell for Photoelectrochemical Water Dissociation*, http://www.freepatentsonline.com/y2017/0076875.html (2017), patent no. 20170076875.
[7] A. A. Metri, T. S. Rani, and P. Sharan, in *Silicon Photonics and High Performance Computing. Advances in Intelligent Systems and Computing*, edited by A. Mishra, A. Basu, and V. Tyagi (Springer, Singapore, 2018), vol. 718.
[8] L. Vines and A. Y. Kuznetsov, in *Oxide Semiconductors*, edited by B. G. Svensson, S. J. Pearton, and C. Jagadish (Academic Press, 2013), vol. 88, pp. 67–104.
[9] D. Jena, S. Heikman, D. Green, D. Buttari, R. Coffie, H. L. Xing, S. Keller, S. Denbaars, J. S. Speck, U. K. Mishra, et al., Appl. Phys. Letl. **81**, 4395 (2002).
[10] J. Simon, V. Protasenko, C. Lian, H. Xing, and D. Jena, Science **327**, 60 (2010).
[11] J. J. Ibbetson, P. Fini, K. Ness, S. DenBaars, J. Speck, and U. Mishra, Appl. Phys. Lett. **77**, 250 (2000).
[12] A. Franciosi and C. G. Van de Walle, Surf. Sci. Rep. **25**, 1

(1996).
[13] A. Klein, Thin Solid Films **520**, 3721 (2012).
[14] R. T. Tung, Appl. Phys. Rev. **1**, 011304 (2014).
[15] X. D. Zhang, M. L. Guo, W. X. Li, and C. L. Liu, J. Appl. Phys. **103**, 063721 (2008).
[16] J. J. Chen, F. Ren, Y. Li, D. P. Norton, S. J. Pearton, A. Osinsky, J. W. Dong, P. P. Chow, and J. F. Weaver, Appl. Phys. Lett. **87**, 192106 (2005).
[17] H. H.-C. Lai, V. L. Kuznetsov, R. G. Egdell, and P. P. Edwards, Appl. Phys. Lett. **100**, 072106 (2012).
[18] D. M. Detert, K. B. Tom, C. Battaglia, J. D. Denlinger, S. H. N. Lim, A. Javey, A. Anders, O. D. Dubon, K. M. Yu, and W. Walukiewicz, J. Appl. Phys. **115**, 233708 (2014).
[19] D. A. Shirley, Phys. Rev. b **5**, 4709 (1972).
[20] *http://www.casaxps.com.* (2012).
[21] D. Drouin, Microsc. Microanal. **12** (2006).
[22] W. Shan, W. Walukiewicz, J. W. Ager, K. M. Yu, H. B. Yuan, H. P. Xin, G. Cantwell, and J. J. Song, Appl. Phys. Lett. **86**, 191911 (2005).
[23] W. Zhan, C. Granerød, V. Venkatachalapathy, K. M. Johansen, I. J. T. Jensen, A. Y. Kuznetsov, and . Prytz, Nanotechnology (2017), accepted manuscript.
[24] National Physical Laboratory, http://www.npl.co.uk/science-technology/surface-and-nanoanalysis/services/sputter-yield-values (2016).
[25] G. Moretti, J. Electron Spectrosc. Relat. Phenom. **95**, 95 (1998).
[26] V. Venkachalapathy, A. Galeckas, M. Trunk, T. Zhang, A. Azarov, and A. Y. Kuznetsov, Phys. Rev. B **83**, 125315 (2011).
[27] A. G. S. Kumar, L. Obulapathi, T. S. Sarmash, D. J. Rani, M. Maddaia, T. S. Rao, and K. Asokan, JOM **64**, 834 (2015).
[28] T. Makino and Y. Segawa, Appl. Phys. Lett. **85**, 759 (2004).
[29] M. W. Allen, C. H. Swartz, T. H. Myers, T. D. Veal, C. F. McConville, and M. Durbin, Phys. Rev. B **81**, 075211 (2010).